DESIGN AND ANALYSIS OF SUBSTRATE INTEGRATED WAVEGUIDE BASED FILTERING ANTENNAS

CHU HUI

(B.Eng., Nanjing University of Science and Technology, P.R.C)

A THESIS SUBMITTED FOR THE DEGREE OF
PHILOSOPHY DEPARTMENT OF CIVIL
ENGINEERING
NATIONAL UNIVERSITY OF SINGAPORE

2017

Supervisor:
Associate Professor Guo Yongxin

Examiners:
Professor Yeo Tat Soon
Associate Professor Chen Xudong
Assistant Professor Qiu Cheng Wei

DECLARATION

I hereby declare that the thesis is my original work and it has been written by me in its entirety.

I have duly acknowledged all the sources of information which have been used in the thesis.

This thesis has also not been submitted for any degree in any university previously.

Chu Hui

05 Jan 2017

Acknowledgements

First and foremost, I want thank my supervisor Prof. Yongxin Guo, for supporting me during the past 3 years. I appreciate all his contributions of time, ideas, and funding to make my Ph.D. experience productive and stimulating. The joy and enthusiasm he has for the research have been contagious and motivational for me. I am also thankful for the excellent example he has set.

I would like to thank my friends in Microwave Research Laboratory and MMIC Laboratory, who have been very kind and supportive in my research life, especially Miss. Lei Wen, Mr. Liu Zhongtao, Mr. Zhang Hao, Mr. Huang Andong, Mr. Zhu Xiaoqi, Miss. Wang Mengshuang, Miss Wang Cong, Miss Yin Tiantian, Dr. Liu Changrong, Dr. Zhong Zheng, Dr. Tian Buning.

Many thanks go to all the staff in Microwave Research Laboratory and ECE Department, especially Mdm. Guo Lin, Mdm. Lee Siew Choo, and Mr. Sing Cheng Hiong for their kind assistances in all the technical and administrative support.

I also thank staffs in Nantong University, Prof. Chen Jianxin, Prof. Shi Jin, Mr. Lu Qingyuan, Mr. Zhou Liheng and Ms. Tang Hui, for always being so helpful to deal with some chores for me.

Lastly, I would like to thank my parents, for raising me with a love of science and supporting me in all my pursuits. And most of all, I would like to thank my loving, supportive, encouraging, and patient wife Mrs. Wang Peijuan, for her faithful support during the whole period of this Ph.D.. My wife has been a true and great supporter and has unconditionally loved me during my good and bad times. She has been faith in me and my intellect even when I didn't have faith in myself. These past several years have not been an easy ride, both academically and personally. I truly thank my wife for sticking by my side, even when I was irritable and depressed. I feel that what

we both learned a lot about life and strengthened our commitment and determination to each other and to live life to the fullest.

Table of Contents

Acknowledgements i

Table of Contents iii

Summary v

List of Tables vii

List of Figures ix

List of Acronyms xv

Chapter 1 Introduction 1

1.1 Background and Motivation 1

1.2 Design of Filtering Antennas 5

1.2.1 Design Approaches of Filtering Antennas 5
1.2.2 Filter-Antenna Synthesis Methods Using Reference Filters 9

1.3 Development and Application of Substrate Integrated Waveguide Cavity Resonators 10

1.4 Thesis Outline 14

1.5 Original Contributions 14

1.6 Publication List 15

Chapter 2 Design and Analysis of SIW Cavity Filtering Antennas with High Out-of-Band Attenuation 17

2.1 Introduction 17

2.2 Generation of Radiation Nulls for Cavity-Based Filtering Antennas ... 18

2.2.1 Analysis and Selection of TZ Realization Methods in Reference Filters . 19
2.2.2 Reference Filter Synthesis Using Gradient-Based Optimization Method 21

2.3 A 3-D Millimeter-Wave Filtering Antenna with High Selectivity and Low Cross-Polarization 26

2.3.1 Design of A Single Cavity to Realize a Coupling Scheme with Two Out-of-Band TZs 27
2.3.2 A Low Cross-Polarization Antenna Realized using the Dual-Slot Structure and Backed by a Cavity 30
2.3.3 Design of Reference Filter and Its Corresponding Filter-Antenna Synthesis 32
2.3.4 Measurement Results and Discussions 43

2.4 An SIW Filtering Antenna Array with Quasi-Elliptic Gain Response . 45

2.4.1 A Two-Output Reference Filter with Quasi-Elliptic Response 46
2.4.2 Filtering Antenna Array Synthesis..56
2.4.3 Measurement Results and Discussions 58

2.5 Summary 60

Chapter 3 Array Designs of SIW Cavity Filtering Antennas for Specific Applications..61

3.1 Introduction 61

3.2 A Millimeter-wave Filtering Monopulse Antenna Array Based on Substrate Integrated Waveguide Technology 62

3.2.1 A Four-Output Filter Composed of One Monopulse Comparator...........63
3.2.2 Filtering Monopulse Antenna Array Synthesis.......................................71
3.2.3 Measurement Results and Discussions 75

3.3 A Filtering Dual-Polarized Antenna Subarray Targeting for Base Stations in Millimeter-Wave 5G Wireless Communications.......................77

3.3.1 Design of A Dual-Path Filter 79
3.3.2 Design of Dual-Polarized Filtering Antenna Subarray 93
3.3.3 Measurement and Discussions 99

3.4 Summary 101

Chapter 4 Implementation of Synthetic Material in Dielectric Resonator Based Filtering Antennas for Broadband Applications 103

4.1 Introduction 103

4.2 Q_{EXT} Extraction of a DRA Operating at Its TE^{y}_{111} Mode. 105

4.3 Continuous adjustment of Q_{EXT} of a rectangular dielectric resonator using synthetic dielectric 110

4.4 Prototype Demonstration...111

4.4.1 Reference Filter Synthesis 112
4.4.2 Realization of A Filtering Antenna Using Ideal Dielectric.....................113
4.4.3 Realization of A Filtering Antenna Using Synthetic Dielectric.............114

4.5 Measurement Results and Discussions 118

4.6 Conclusion..119

Chapter 5 Conclusion and Proposal for Future Research 121

5.1 Contributions..121

5.2 Future Research..123

Bibliography 125

Summary

In this thesis, antennas with filtering responses for both input return loss and radiation gain, are analyzed by filter synthesis method and designed with substrate integrated waveguide resonators, to obtain better suppressions against out-of-band signals and functional array designs for practical applications.

Firstly, filtering antennas with high out-of-band attenuation are proposed. This kind of high attenuation is realized by creating radiation nulls at either side of the passband of an antenna. In order to achieve this aim, reference filters with transmission zeros, whose design specifications are synthesized by using the gradient-based optimization method, are analyzed and designed. The inter-cavity cross coupling is selected and implemented to physically realize required coupling topologies and also enable an easy replacement of resonators in the filter/antenna synthesis. In this thesis, a filtering antenna element is developed using the multi-layer printed circuit board technology to achieve both high selectivity and low cross-polarization level. Furthermore, a two-element antenna array with quasi-elliptic gain responses is designed, fabricated and measured for a demonstration.

Secondly, the filtering antenna concept is expanded from a simple element/array to complicated array designs for specific applications. Four-element filtering antenna arrays, with monopulse and dual-polarization characteristics, have been developed for applications of radar tracking systems and 5G base stations, respectively. Reference filters with multiple inputs/outputs are proposed to fulfill magnitude/phase requirements. Both designs are constructed in vertical stacked 3-D structures, to achieve compact size as well as good performance for different systems.

Lastly, a filtering antenna whose radiator is a dielectric resonator is proposed for the first time. Air-filled holes are periodically introduced into the dielectric resonator, to meet the external coupling quality factor required in its reference filter. A good correspondence is observed between frequency responses of the filtering antenna and its corresponding reference filter.

List of Tables

Table 1.1 Overview of Filtering Antennas in the Prior Literature..........................6

Table 2.1 Four Cases of the TZ Realization Method Using Cross-Couplings between Different Inter-Cavity Modes..20

Table 2.2 Comparison between Different Methods for the Realization of Two TZs using the Cross-Coupling..21

Table 2.3 Frequency Distance between Adjacent Transmission Zeros......................49

Table 3.1 Amplitude of S_{mn}..71

Table 3.2 Phase of S_{mn}..71

Table 4.1 Performance Comparison between Filtering Antennas with Different Radiators...109

List of Figures

Figure 1.1 The multi-functional antenna under different categories 2

Figure 1.2 Number of published articles related to filtering antennas with bandpass responses..3

Figure 1.3 Design approaches for filtering antennas...5

Figure 1.4 Filtering antenna subarrays for dual-band base station applications.... 8

Figure 1.5 Synthesis procedures for filtering antennas...9

Figure 1.6 The geometry of an SIW cavity resonator...11

Figure 2.1 Filter coupling scheme with a pair of transmission zeros by introducing the cross-coupling between (a) different resonators, (b) source & load and (c) different modes in a single resonator..19

Figure 2.2 Flow of the gradient-based optimization algorithm.................................25

Figure 2.3 (a) Proposed coupling scheme exhibiting two transmission zeros. (b) Electric field distributions of the spurious TE_{101}-mode and resonant TE_{102}- & TE_{201}-modes in a nearly square SIW cavity..27

Figure 2.4 (a) 3-D view and (b) side-view of the proposed single-cavity with two transmission zeros fed by microstrip lines...28

Figure 2.5 Simulated $|S_{21}|$ results of the proposed single-cavity with two TZs..........29

Figure 2.6 (a) 3-D view and (b) side view of the proposed dual-slot antenna backed by a cavity..30

Figure 2.7 Radiation patterns of the proposed dual-slot antenna operating at 31.5 GHz..31

Figure 2.8 Proposed third-order coupling scheme for a reference BPF with two TZs..33

Figure 2.9 (a) Cross-section view, (b) side view and (c) top view of a three-pole cavity BPF..33

Figure 2.10 Calculated frequency responses using optimized parameters.................37

Figure 2.11 Geometry of the proposed filtering antenna. (a) 3-D view, (b) side view and (c) top view..39

Figure 2.12 EM field distributions in resonant cavities at (a) 31.25 GHz and (b) 31.75 GHz..39

Figure 2.13 Reflection coefficients of the waveguide port 1 for the end resonator of either a single-mode cavity in the filter or dual-slot antenna backed by a cavity in the filtering antenna..40

Figure 2.14 Simulated $|S_{11}|$ results of the filter and filtering antenna..........................41

Figure 2.15 Simulated $|S_{21}|$ results of the filter and gain of the filtering antenna........41

Figure 2.16 (a) Top and bottom views of the fabricated prototype. (b) Fabricated antenna enclosed by a metallic cavity.........43

Figure 2.17 Simulated and measured $|S_{11}|$ results of the proposed filtering antenna..43

Figure 2.18 Simulated and measured broadside gain results of the proposed filtering antenna.........44

Figure 2.19 Simulated and measured results of the radiation pattern at 31.5 GHz for the proposed filtering antenna.........44

Figure 2.20 The geometric configuration of (a) a one-output filter and (b) the proposed two-output filter with quasi-elliptic response, *L1*=4.8mm, *L2*=5.34mm, *L3*=1.6mm, *L4*=1.4mm, *W1*=16.8mm, *W2*=5mm, *W3*=3.14mm, *W4*=1.68mm, *W5*=0.85mm, *W6*=0.45mm.........46

Figure 2.21 Geometry and feed arrangement of the TE_{103}-mode Cavity.........47

Figure 2.22 Electric field distributions of TE_{102}-, TE_{103}- and TE_{104}-modes in a single cavity.........48

Figure 2.23 Simulated S-parameter results of cavities with the feed arrangement shown in Figure 2.21, whose resonance at 28.1 GHz is of TE_{102} mode (dashed line) and TE_{103} mode (dot-dot-dashed line), separately.........49

Figure 2.24 Coupling schemes of (a) a 2nd-order bandpass filter and (b) a 2nd-order two-output filter extended from the previous filter.........50

Figure 2.25 Frequency responses of the two-output filter.........54

Figure 2.26 Schematics of simulation models used for evaluating the reflection coefficients of a waveguide port used to excite (a) cavity resonator with a filter port and (b) an SIW cavity-backed slot antenna.........55

Figure 2.27 (a) Cross-section view and (b) geometrical parameters of the proposed filtering antenna array, *Lc*=4.5mm, *Ls*=3.54mm, *Wc*=5mm, *Ws*=0.66mm.........55

Figure 2.28 Simulated $|S_{11}|$ results of the filter and filtering antenna array.........57

Figure 2.29 Simulated $|S_{21}|$ results of the filter and gain of the filtering antenna array.........57

Figure 2.30 Top and bottom views of the fabricated filtering antenna array.........57

Figure 2.31 Simulated and measured $|S_{11}|$ results of the filtering antenna array.........58

Figure 2.32 Simulated and measured gain of the filtering antenna array......... 59

Figure 2.33 Simulated and measured radiation patterns of the proposed filtering antenna array at 27.94 GHz (unit: dB).........59

Figure 3.1 Cross-section view of the proposed filtering monopulse antenna array...64

Figure 3.2 Electric field distributions of two degenerated modes (TE_{201} and TE_{102}) in the proposed monopulse comparator.........64

Figure 3.3 (a) Cross-section view, (b) top view and (c) side view of a four-output filter.........66

Figure 3.4 Coupling schemes of (a) a three-order bandpass filter and (b) three-order four-output filters (sum and difference channel) extended from the previous filter....67

Figure 3.5 Synthesized frequency responses of the four-output filter and its one-output counterpart....69

Figure 3.6 Simulated frequency responses of the four-output filter operating in the (a) difference channel and (b) sum channel....70

Figure 3.7 Schematics of simulation models used for evaluating the reflection coefficients of a waveguide port used to excite (a) a cavity resonator with a filter port and (b) an SIW cavity-backed slot antenna.... 72

Figure 3.8 Reflection coefficients of the waveguide port 1 for the end resonator of either a cavity resonator or a cavity-backed slot antenna....72

Figure 3.9 Geometrical parameters of the proposed filtering monopulse antenna array....73

Figure 3.10 Simulated and measured reflection coefficients of the filtering monopulse antenna array for the sum channel, as well as ideal frequency responses of the four-output filter....73

Figure 3.11 Simulated and measured reflection coefficients of the filtering monopulse antenna array for the difference channel, as well as ideal frequency responses of the four-output filter....74

Figure 3.12 Simulated radiation patterns of the filtering antenna at 29.25 GHz....74

Figure 3.13 Top and bottom views of the fabricated filtering monopulse antenna array....75

Figure 3.14 Measured radiation patterns of the filtering antenna at 29.25 GHz....76

Figure 3.15 A hybrid beamforming structure (digital beamforming and analog beamforming) for 5G mmWave base station applications....78

Figure 3.16 (a) The electric field and (b) magnetic field distributions of two degenerated modes (diagonal TE_{102} and TE_{201}) in a square SIW cavity....81

Figure 3.17 Stage-by-stage cavity arrangement in the dual-path filter....81

Figure 3.18 Field distributions of the 1st-stage cavity (a) before geometry modification and (b) after geometry modification....84

Figure 3.19 Simulated $|S_{12}|$ versus d' with different d'' as a parameter....84

Figure 3.20 Models for the coupling simulation between cavities of the 1st- and 2nd-stage. (a) Cavities resonating under the same mode (case 1). (b) Cavities resonating under orthogonal modes (case 2)....86

Figure 3.21 Couplings between adjacent cavities of the 1st- and 2nd-stage in different situations....86

Figure 3.22 Models for the coupling simulation between cavities of the 2nd- and 3rd-stage. (a) Cavities resonating under the same mode (case 1). (b) Cavities resonating under orthogonal modes (case 2).......87

Figure 3.23 Couplings between adjacent cavities of the 2nd- and 3rd-stage in different situations.......87

Figure 3.24 Models for the coupling simulation between cavities of the 3rd- and 4th-stage. (a) cavities resonating under the same mode (case 1). (b) Cavities resonating under orthogonal modes (case 2).......88

Figure 3.25 Couplings between adjacent cavities of the 3rd- and 4th-stage in different situations.......88

Figure 3.26 (a) Cross-section view of the proposed dual-path filter and (b) its layer definition.......90

Figure 3.27 Coupling schemes of a (a) 4th-order bandpass filter and (b) 4th-order dual-path filter (path 1 and path 2) extended from the previous filter.......91

Figure 3.28 Synthesized frequency responses of one path in the dual-path filter with four outputs and its one output counterpart. (dashed line: synthesized responses, solid line: full-wave simulation responses).......91

Figure 3.29 Dimensions of the proposed dual-path filter in different stages. (a) The 4th-stage. (b) The 3rd-stage. (c) The 2nd-stage. (d) The 1st-stage. (Unit:mm).......... 92

Figure 3.30 Geometries and electric field distributions for (a) radiator 1 [quad-slot operating in diagonal $TE_{201}\&TE_{102}$ modes], (b) radiator 2 [dual-slot operating in diagonal $TE_{201}\&TE_{102}$ modes], (c) radiator 3 [quad-slot operating in $TE_{201}\&TE_{102}$ modes] and (d) radiator 4 [dual-slot operating in $TE_{201}\&TE_{102}$ modes].......95

Figure 3.31. Schematics of simulation models used for evaluating the reflection coefficients of a waveguide port used to excite (a) cavity resonator with a filter port and (b) SIW cavity backed slot antenna.......96

Figure 3.32 Cross-section view of the proposed filtering dual-polarized antenna sub-array.......96

Figure 3.33 Geometrical parameters of the radiation part for the proposed filtering monopulse antenna array.......97

Figure 3.34 Simulated $|S_{11}|\&|S_{21}|$ results of the filter (proposed in Section 3.3.1) and filtering antenna (proposed in Section 3.3.2).......97

Figure 3.35 Simulated $|S_{21}|$ results of the filter and gain of the filtering antenna...... 97

Figure 3.36 (a) Top view and bottom view of the fabricated filtering antenna and (b) fabricated antenna with a metallic shield 98

Figure 3.37 Simulated and measured reflection coefficients and isolation of the proposed filtering antenna.......99

Figure 3.38 Simulated and measured gain of the proposed filtering antenna subarray.......100

Figure 3.39 Simulated and measured radiation patterns of the filtering antenna subarray at 37 GHz. (a) Excitation at P1 and (b) Excitation at P2...........................100

Figure 4.1 Simulation model used to extract the Q_{EXT} of a DRA operating at its TE^{y}_{111} mode...106

Figure 4.2 Reflection coefficients of the model used for permittivity extraction.....106

Figure 4.3 Extracted Q_{ext} of a DRA versus its width "H" with different height "W" as a parameter...107

Figure 4.4 Extracted Q_{ext} of a DRA versus its permittivity ε_r with different height "W" as a parameter...107

Figure 4.5 (a) Cross-section view and (b) top view of the reference 2nd-order SIW cavity BPF..111

Figure 4.6 Cross-section view of the filtering antenna using ideal dielectric...........111

Figure 4.7 Simulated frequency responses of the reference filter and the filtering DRA in Figure 4.6..112

Figure 4.8 HFSS simulation models for extracting the electromagnetic characteristics of (a) synthetic dielectric with the air-filled hole and (b) conventional dielectric....113

Figure 4.9 Extracted ε_{reff} along Z-axis [Case A] and X-&Y-axis [Case B] of the simulation model in Figure 4.8(a)..114

Figure 4.10 HFSS simulation models for the verification of permittivity extraction of (a) synthetic dielectric with air-filled holes and (b) conventional dielectric............114

Figure 4.11 The geometry of a 2nd-order filtering antenna using a synthetic dielectric resonator as the radiator...115

Figure 4.12 Cross-section view of the filtering antenna using synthetic dielectric...115

Figure 4.13 Simulated frequency responses of the reference filter and the filtering DRA in Figure 4.11..116

Figure 4.14 (a) Top view and bottom view and (b) cross-section view of the fabricated filtering antenna prototype..117

Figure 4.15 Simulated and measured $|S_{11}|$ and gain of the proposed filtering antenna...118

Figure 4.16 Simulated and measured radiation patterns at 11 GHz for the filtering antenna...119

List of Acronyms

AIA	Active-integrated antenna
NIC	Negative impedance converter
PIA	Passive-integrated antenna
SIW	Substrate integrated waveguide
PCB	Printed circuit board
LTCC	Low-temperature co-fired ceramic
FSS	Frequency selective surface
LTE	Long term evaluation
UWB	Ultra wideband
DRA	Dielectric resonator antenna
PEC	Perfect conductor
THz	Terahertz
CAA	Computer-aided analysis
TZ	Transmission zero
BPF	Bandpass filter
HFSS	High frequency structure simulator
GCPW	Grounded coplanar waveguide
mm-Wave	Millimeter-wave
NLoS	Non-line-of-sight
DBF	Digital beamforming

Chapter 1 Introduction

1.1 Background and Motivation

In the past several decades, multifunctional antennas have already been proposed and implemented extensively to miniaturize various active and passive devices, which operate in the radio-frequency range. Active-integrated antennas (AIA) [1] can be considered as one of the earliest multifunctional antennas that have received a high level of attention from both academia and industry. An active antenna is defined as an antenna integrated with active electronic components, which is quite different from typical passive antennas. Active antennas can behave different functions, such as amplifying the RF power received by the antenna and allowing much longer transmission cable, miniaturizing the antenna size and decreasing the mutual coupling between array elements [2]. Therefore, active antennas have received considerable interest and have been used for both receiving and transmitting applications. Based on the active component it includes, AIAs can be roughly categorized into five groups summarized in Figure 1.1.

Besides active-integrated antennas, passive-integrated antennas (PIAs) also attract significant attention in recent years. This is due to the fact that, PIAs such as circulator antennas and filtering antennas are able to integrate several functions into a single module to achieve high compactness, low loss and low cost, which are all

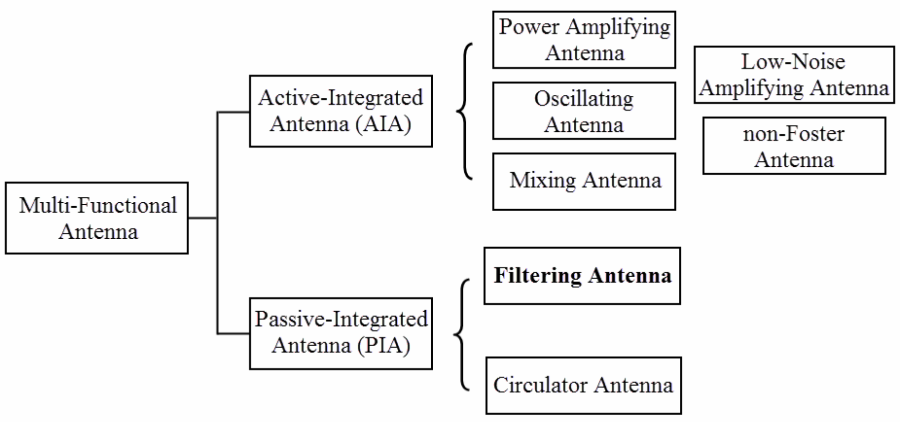

Figure 1.1 The multi-functional antenna in different categories.

highly desired in modern microwave systems. In a circulator antenna [3], the circulator can be designed without the need for impedance equalization with the antenna. In a filtering antenna [4], an antenna and a filter are co-designed without the use of connectors via standard 50-Ω ports for the connection between them.

The filtering antenna can provide a shaping of filter-like response for both the antenna gain and input return loss. Therefore, strong and growing interest [seen in Figure 1.2] in this research topic is being fueled by a recognition that this device allows high efficiency and compact size. Most published works related to filtering antennas focus on transmission line structures, both for the radiator and the resonator. It is a common knowledge that, transmission-line structures are not the optimal choice for applications operating at high frequency ranges, e.g. the millimeter-wave (mm-Wave) band, due to their high radiation loss. Therefore, few work has been done at an operation frequency higher than 10 GHz in published articles.

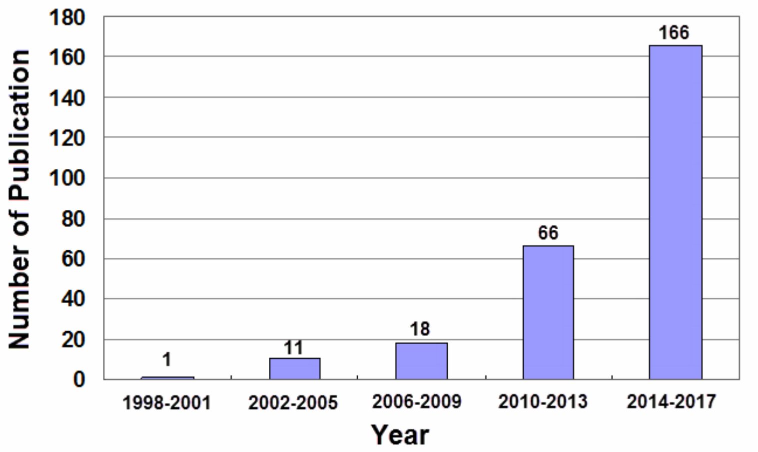

Figure 1.2 Number of published articles related to filtering antennas with bandpass responses. *Data source: Engineering Village

On the other hand, the mm-Wave technology is attracting more and more attention, because it can support high data-rate data transmission when the mm-Wave band is used as the carrier frequency in wireless systems. Transmission lines are no longer suitable for mm-Wave components due to their large radiation loss. Instead, the substrate integrated waveguide (SIW) technology [5] becomes a promising candidate. An SIW is fabricated in a dielectric substrate using two rows of grounded metallic vias, which are connected to two parallel metallic plates. An SIW transforms the non-planar rectangular waveguide into a planar form. The fabrication of an SIW is compatible with conventional planar fabrication process, e.g. printed circuit board (PCB) and low-temperature co-fired ceramic (LTCC) technology. SIW structures can exhibit high power-handling capability, easy integration with other circuits, low cost and low radiation loss extremely at high frequency ranges. To take full advantages of the SIW, the first aim of this research work intends to apply this technology to filtering antenna designs operating at the mm-Wave region.

Meanwhile, in a filter design, the sharp cutoff skirt for transmission responses is desired to better attenuate out-of-band signals. The situation is similar to a filtering antenna, whose radiation is preferred to be highly suppressed outside the passband. This requirement can be achieved by introducing radiation nulls in frequency responses of those filtering antennas, which is seldom done in published works. To meet this requirement, the second aim of this research work is to design novel SIW cavity-based filtering antennas and antenna arrays with high out-of-band attenuation.

Moreover, antenna arrays are essential in many applications, to achieve improved performance over that of a single antenna. Most of current research concentrates on filtering antenna element designs, which also limits the application area of this kind of PIAs. Since few research papers report array designs of filtering antennas, the third objective of this research work attempts to design filtering antenna arrays with specific functions for different systems.

The following section will review prior research on filtering antenna designs, their analysis/synthesis methods and applications of the SIW resonator, respectively.

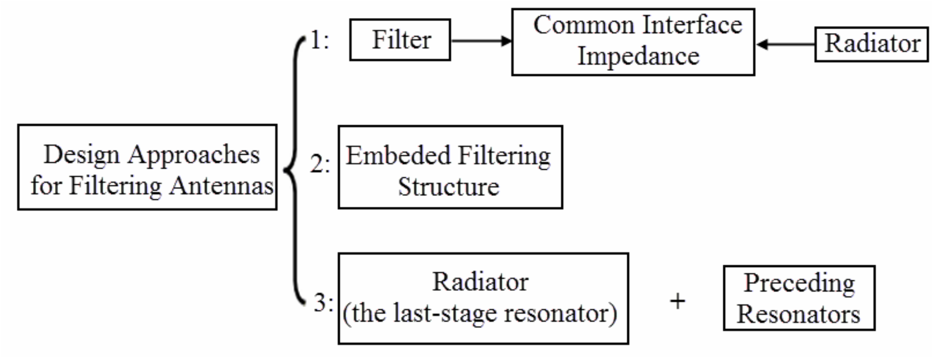

Figure 1.3 Design approaches for filtering antennas.

1.2 Design of Filtering Antennas

1.2.1 Design Approaches of Filtering Antennas

An antenna with filtering responses, which means it can provide not only a conversion between radio waves and electric power, but also a shaping of filter-like response for the input return loss and antenna gain, turns out to be an efficient approach in improving the efficiency and reducing the size of the functional block for a microwave system. For brevity, this kind of an antenna is also called as the filtering antenna or the filtenna. The filtering antenna can be used to reduce the loss introduced by the transmission between the RF filter and the radiator. Typically, three kinds of approaches [as illustrated in Figure 1.3] can be implemented to obtain a filtering antenna.

The first approach is to integrate a filter and an antenna with common impedance at the interface between them [6], [7]. The challenge of this approach lies in the selection of the optimized common impedance, since it has to be easily achieved by both components. In most cases, an impedance transformer is still required between the antenna and the filter for a good matching. A co-designed antenna-filter consisting of a microstrip patch antenna and a hairpin filter was presented in [6]. Another design example is an SIW filtenna for *Ku*-band applications [7]. However, there are not many filtering antennas designed by this approach. The main reason is

Table 1.1 Overview of Filtering Antennas in the Prior Literature

Reference	Freq (GHz)	Radiator Type	Resonator Type for the Filter	Approach No.
[6]	4	Patch	Hairpin resonator	1
[7]	14.5	Serially-fed patch array	SIW cavity	1
[8]	10	Horn	FSS	2
[9]	2.5	Patch	Shorting pin	2
[10]	5	Dielectric resonator antenna (DRA)	Open stub	2
[12]	3.1-10.9	Monopole	Shorting pin	2
[13]	3.1-10.9	Monopole	Shorting stub	2
[15]	5	Patch	T-shape microstrip	3
[16]	2.5	Patch	Circular open-loop	3
[25]	2.5	Monopole	Open-loop	3
[26]	2.5	Monopole	Coupled line	3
[27]	10	Slot	SIW cavity	3
[28]	10.25	Slot	SIW cavity	3
[30]	5	Patch	E-shape microstrip	3
[31]	10	Patch	SIW cavity	3

that the additional loss brought by the impedance transformer reduces the efficiency of this functional block.

In the second approach, some filtering structures are embedded into different parts of an antenna, to achieve bandstop responses either within or outside its operating bandwidth, without increasing the size of the whole functional block. The filtering structure can be an SIW cavity frequency selective surface (FSS) covered at the aperture of a horn antenna [8]. It can also be a group of shorting pins [9] or an open stub [10], to produce radiation nulls and enhance the out-of-band suppression level. It should be highlighted that, the structure proposed in [9] has already been successfully applied in dual-band base stations, for Digital Cellular System (DCS: 1710–1880 MHz) and Wideband Code Division Multiple Access (WCDMA: 1920–2170 MHz) systems [11]. As can be seen in the structure illustrated in Figure 1.4, two 1×6 filtering antenna subarrays operating at different frequency ranges are arranged side by side. No diplexer is required in this system so that the corresponding insertion loss can be eliminated. Besides the above designs, some filtering structures [12-14] were also proposed to generate bandstop notches within the passband of ultra wideband (UWB) antennas. The main advantage of this approach is that no additional insertion loss is introduced. However, the bandwidth of the passband/stopband in this kind of a filtering antenna is highly dependent on the filtering structure, and not that flexible

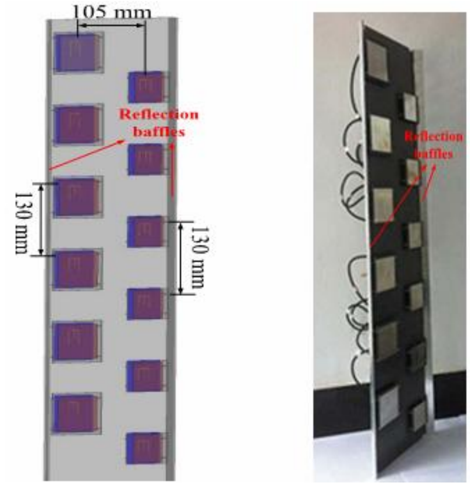

Figure 1.4 Filtering antenna subarrays for dual-band base station applications [11].

to be adjusted for various specifications.

In the third approach, the antenna works as a radiator and also a resonator of the last-stage in a bandpass filter. All filtering antenna designs proposed in this thesis are analyzed and synthesized using this approach. The specifications of this kind of a filtering antenna can almost be the same as its reference filter, which means its performance is easier to be adjusted and optimized for different systems. This approach was first proposed by Person *et al.* using slotline resonators and a slotline dipole antenna [4]. Rectangular and fan-shaped patch antennas were applied in [15] and [16], respectively. Patch antennas were also used to construct filtering antennas with duplex [17], [18], dual-band [19], [20], dual-polarization [21], [22] and even circular polarization [23], [24] properties. The use of monopole antenna was reported in [25] and [26]. Cavity-backed slot antennas was implemented in planar [27] or 3-D integrated [28] filtering antenna designs. A dielectric resonator antenna (DRA),

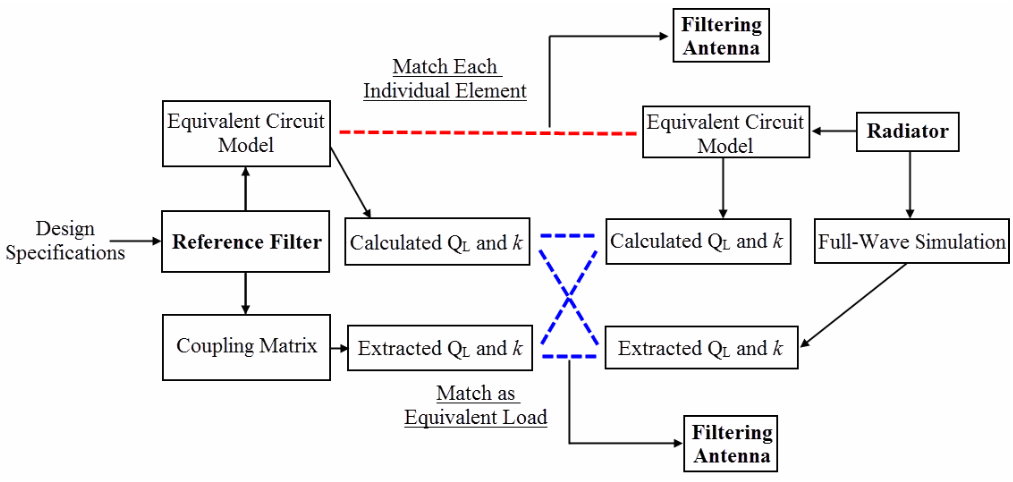

Figure 1.5 Synthesis procedures for filtering antennas.

which is simultaneously used as a filtering device, was proposed by Leung *et al* [29]. However, this structure is not a filtering antenna, but two devices share a common resonator. Meanwhile, among published works, only the one by Chung *et al.* can achieve a quasi-elliptic response for the antenna gain [15]. Moreover, few work has been done on the design of filtering antenna arrays [22], [30].

1.2.2 Filter-Antenna Synthesis Methods Using Reference Filters

All filtering antennas proposed in this thesis can be categorized into the third approach described in Section 1.2.1. In this approach, a reference filter is always required based on detailed design specifications. This filter will be converted to a filtering antenna by replacing the resonator of the last-stage in the filter using a radiator. The reference filter can be synthesized by either an equivalent circuit model or a coupling matrix. In order to successfully obtain a filtering antenna, whose in-band performance is exactly the same as its reference filter, two methods can be implemented. One can first extract the equivalent circuit model of a filtering antenna. Then, each individual element in the equivalent circuit model of the filtering antenna is optimized to be identical to that in the circuit model of its reference filter [26]. One can also enable Q_L of the radiator in the filtering antenna to be identical to Q_L of the end resonator in the reference filter, and the same internal coupling coefficients k between the last two resonators in the filtering antenna and its reference filter [28]. When using this approach, the radiator can work as an equivalent load as the end resonator in the reference filter to its preceding resonators.

For the reference filter, its Q_L and k values can be either calculated based on its equivalent circuit model [31] or directly extracted from the coupling matrix related to it [28]. For the radiator, there are also two ways to obtain the values of Q_L and k, which are calculated results from its circuit model [27] or extracted results from a full-wave simulation [28], respectively. All the above synthesis methods are summarized in Figure 1.5 for a better understanding.

1.3 Development and Application of Substrate Integrated Waveguide Cavity Resonators

In this thesis, most of proposed designs are based on cavity resonators realized by the substrate integrated waveguide technology (SIW) [32], [33]. The SIW cavity

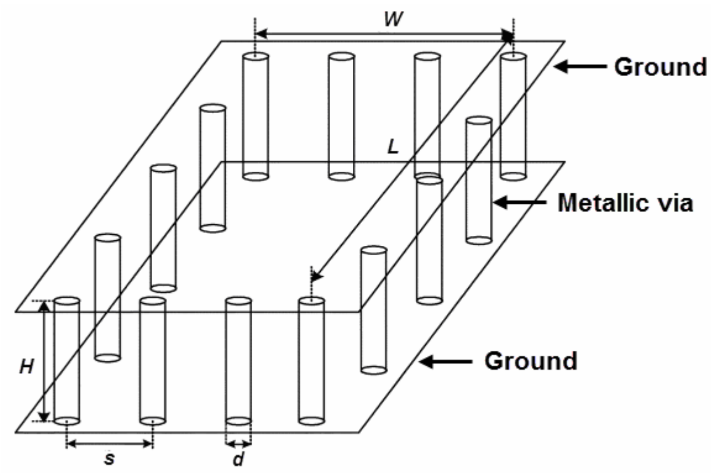

Figure 1.6 The geometry of an SIW cavity resonator.

resonator is achieved by a row of metallic vias connecting the upper and lower ground plane of a substrate. On one hand, when compared with the traditional waveguide cavity, the SIW cavity brings advantages of low profile, small fabrication tolerance and easier integration with microstrip circuit. On the other hand, when compared with microstrip resonators, it exhibits advantages such as self-packaging characteristic, easier integration with heat sink and small radiation loss especially at mm-Wave range. For those cavity-resonator based components operating at mm-Wave band, the tolerance in the fabrication process using mechanic methods is the key issue which limits the yield. Moreover, a transition is always required in the integration of waveguide components and other components based on the PCB technology. This kind of a transition not only brings additional loss, but also affects the performance of the overall module due to misalignments in the installation. As a contrast, the SIW resonator is fully compatible with the PCB or low temperature co-fired ceramic (LTCC) technology, which enables a much easier connection with other PCB/LTCC circuits. In high-power applications, the heat sink can directly touch either ground planes of the SIW resonator for an efficient cooling.

The geometry of a typical SIW cavity resonator is illustrated in Figure 1.6. Those vertical perfect conductor (PEC) walls are formed by metallic vias inside a dielectric substrate, while horizontal PEC walls are metallic layers of a substrate. The diameter of vias and spacing between adjacent vias are represented by *d* and *p*, respectively. The length, width and height of the cavity are *L*, *W* and *H*, respectively. As introduced in [34], the spacing *p* should be less than half guided wavelength of the highest operation frequency. Since the vertical walls are formed by vias, in which surface currents are not supported, only TE mode is considered inside the SIW cavity resonator. The resonance of a TE_{mnl}-mode resonator can be calculated as [35]:

$$f_{res} = \frac{c}{2\pi\sqrt{\mu_r \varepsilon_r}} \sqrt{\left(\frac{m\pi}{L}\right)^2 + \left(\frac{n\pi}{H}\right)^2 + \left(\frac{l\pi}{W}\right)^2} \tag{1.1}$$

where f_{res} is the resonant frequency, c is speed in vacuum, ε_r is the dielectric constant of the substrate.

The unloaded quality factor of a cavity resonator is composed of three kinds of losses:

$$Q_u = \left(\frac{1}{Q_{cond}} + \frac{1}{Q_{dielec}} + \frac{1}{Q_{rad}}\right)^{-1} \tag{1.2}$$

where Q_{cond}, Q_{dielec} and Q_{rad} are the conductor loss caused by the upper and lower ground planes of the substrate, dielectric loss brought by the substrate and radiation loss between adjacent vias, respectively. The radiation loss can be neglected when the spacing p is smaller than the half guided-wavelength of the highest operation frequency. The conductor loss can be calculated as [36]:

$$Q_{cond} = \frac{(kWL)^3 H\eta}{2\pi^2 R_m (2W^3 H + 2L^3 H + W^3 L + L^3 W)} \tag{1.3}$$

where k is the wave number inside the resonator and equals to $((2\pi f_{res}(\varepsilon_r)^{1/2})/c)$, R_m is the surface resistance corresponding to the upper and lower ground planes and equals to $((\pi f_{res}\mu/\sigma)^{1/2})$, η is the wave impedance of the substrate. The dielectric loss can be calculated as:

$$Q_{dielec} = \frac{1}{\tan(\delta)} \tag{1.4}$$

where $\tan(\delta)$ is the loss tangent of the substrate.

A lot of work has been published using the SIW technology. In term of different types of components, the SIW cavity resonator can be implemented in antennas [37-39], filters [40-43], diplexers [44] and oscillators [45]. In terms of operation frequency range, SIW cavity resonator based components can be implemented in *C*-band [46], *X*-band [47], *Ku*-band [48], *K*-band [49], *Ka*-band [50], *V*-band [51], *W*-band [52] and even Terahertz (THz) band [53]. In terms of fabrication technology, the

SIW cavity resonator can be achieved using PCB [54], LTCC [55] and even silicon [56]. Investigations in the above publications indicate that, the SIW cavity resonator is a good candidate for the design of RF components.

1.4 Thesis Outline

This thesis consists of five chapters. Chapter 2 presents the analysis method and design approach to achieve radiation nulls for SIW cavity filtering antennas. Both element and array designs are proposed and verified. Chapter 3 focus on array designs of filtering antenna using SIW cavity resonators for some specific applications. A monopulse filtering antenna array is proposed for radar tracking systems, while a dual-polarized one is proposed for 5G base stations. Chapter 4 provides a broadband filtering antenna design, in which a dielectric resonator antenna is implemented as the resonator using the synthesized dielectric technology. Chapter 5 gives some conclusions, highlights the limitations in the current project and provides suggestions for future study.

1.5 Original Contributions

In this thesis, the following original contributions have been made:

1. The cross-coupling between inter-cavity modes in a single resonator is proved to be an efficient way to realize radiation nulls for cavity-based filtering antennas.

2. A novel coupling scheme, which can realize two transmission zeros at either side of the passband, is proposed and physically realized using cross couplings between lower/higher modes in an SIW cavity. This SIW cavity is successfully implemented in the design of a filtering antenna with two radiation nulls.
3. A novel filtering antenna array with two radiation nulls at either side of the passband is proposed. The radiation nulls are achieved by using the cross coupling in an oversized SIW cavity. The structure is simple and easy to be applied for array designs.
4. A filtering antenna array which can realize a monopulse radiation pattern is proposed. In this design, a novel monopulse comparator is realized using a dual-mode square SIW cavity with proper excitations.
5. A filtering antenna array with dual-polarization characteristics is proposed. This antenna array is designed using the LTCC process with vertically stacked cavities coupled by proper apertures, in order to achieve both high isolation and low cross-polarization levels.
6. An efficient approach which enables a dielectric resonator antenna to act as the radiator in a filtering antenna to achieve broad bandwidth is proposed.

1.6 Publication List

The following publications are generated in the course of this research.

1 **H. Chu,** C. Jin, J. X. Chen, and Y. X. Guo, "A 3-D millimeter-wave filtering antenna with high selectivity and low cross-polarization," IEEE Transactions on Antennas and Propagation. vol. 63, no. 5 pp. 2375–2380, May 2015.

2 **H. Chu,** J. X. Chen, S. Luo, and Y. X. Guo, "A millimeter-wave filtering monopulse antenna array based on substrate integrated waveguide technology," IEEE Transactions on Antennas and Propagation. vol. 64, no. 1 pp. 316–321, Jan. 2016.

3 **H. Chu,** S. Luo, L. Bian, and Y. X. Guo, "An SIW filtering antenna array with quasi-elliptic gain response based on inter-cavity bypass coupling," International Journal of RF and Microwave Computer-Aided Engineering, vol. 26, no. 3, pp. 191-198, Mar. 2016.

4 **H. Chu** and Y. X. Guo, "A filtering dual-polarized antenna subarray targeting for base stations in millimeter-wave 5G wireless communications," submitted to IEEE Transactions on Components, Packaging and Manufacturing Technology.

5 **H. Chu** and Y. X. Guo, "An approach for efficient implementation of dielectric resonators in filtering antenna designs," submitted to IEEE Transactions on Antennas and Propagation.

Chapter 2 Design and Analysis of SIW Cavity Filtering Antennas with High Out-of-Band Attenuation

This chapter presents a new method of introducing radiation nulls for SIW cavity filtering antennas, including element and array designs, to further improve their attenuation against out-of-band signals. Cross-couplings between inter-cavity modes and a gradient-based optimization for the reference filter synthesis are implemented. Design specifications are also analyzed in order to symmetrically locate radiation nulls with respect to the center working frequency. Details are described in the following sections.

2.1 Introduction

For the purpose of realizing sharp attenuation in the stopband of a filtering antenna, one can either introduce a higher-order coupling scheme, or introduce radiation nulls in its stopband while keep the order of the filtering antenna unchanged. The introduction of a higher-order coupling is simple for the design but suffers large insertion loss. Therefore, the introduction of radiation nulls at both sides of the passband is more desirable to achieve higher out-of-band rejection performance.

Among published filtering antennas designed using the third approach in Figure 1.3, only the microstrip filtering antenna [15] by Chung *et al.* can achieve a quasi-elliptic response for its broadside gain. This microstrip antenna was fed using edge coupled structures and an equivalent circuit can be established for a filter synthesis procedure. However, this method is only applicable for microstrip designs. Moreover, multiple resonators required in this method also lead to a high complexity and bulky size. The selection of a proper and efficient method becomes essential to achieve high out-of-band attenuation for SIW cavity-based filtering antennas.

2.2 Generation of Radiation Nulls for Cavity-Based Filtering Antennas

Radiation nulls of a filtering antenna can be generated by some perturbation structures, e.g., vias and slots on a patch in [9]. These structures will enforce the antenna to resonate at its higher-order mode near the passband, in which case radiations are cancelled in the far-field due to its corresponding out-of-phase current distributions. This method is practical for patch radiators but hard to be implemented in cavity radiators. For cavity based filtering antennas, it is more practical to realize radiation nulls by generating transmission zeros (TZs) in their reference filters, which is similar as the method in [15].

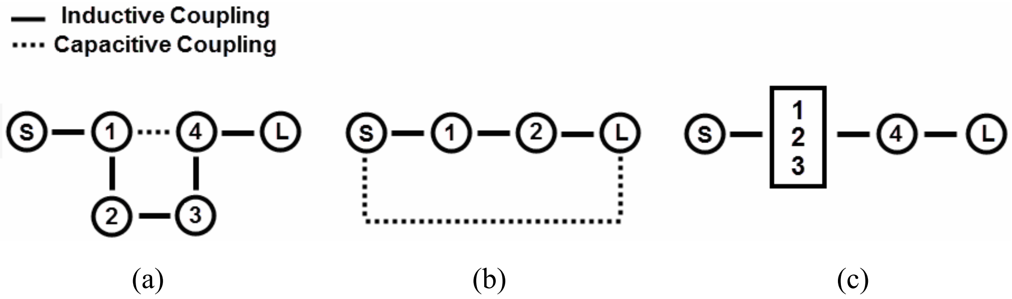

Figure 2.1 Filter coupling schemes with a pair of transmission zeros by introducing the cross-coupling between (a) different resonators, (b) source & load and (c) different modes in a single resonator.

2.2.1 Analysis and Selection of TZ Realization Methods in Reference Filters

The elliptic function filter [57] is a representative kind of filter with transmission zeros. However, this kind of a filter requires cross couplings between several pairs of nonadjacent resonators, which can not always be physically achieved. As an alternative, to introduce only one cross coupling between two nonadjacent resonators [57] is more feasible, together with one or one pair of transmission zeros in the filter's stopband. The cross-coupling not only can be achieved between different resonators, but also can be directly realized between the source and load [58], or between different modes in a single resonator [59]. Figure 2.1 illustrates coupling schemes with one pair of transmission zeros using minimum resonators/modes, for the above three methods of generating cross-coupling, respectively.

Table 2.1 Four Cases of the TZ Realization Method Using Cross-Couplings between Different Inter-Cavity Modes

Case No.	Case	Phase relationship between input and output at f_0 / f_{sp}	Position of TZ
1	$f_0<f_{sp}$	both in phase or both out of phase	$f_0 < f_{TZ} < f_{sp}$
2	$f_0<f_{sp}$	one in phase and one out of phase	$f_{TZ} < f_0 < f_{sp}$
3	$f_{sp}<f_0$	one in phase and one out of phase	$f_{sp} < f_0 < f_{TZ}$
4	$f_{sp}<f_0$	both in phase or both out of phase	$f_{sp} < f_{TZ} < f_0$

When using the coupling topology in Figure 2.1(a), at least 4 resonators are required. Resonator 4 is the last-stage resonator and is supposed to be replaced by a radiator in the filter-antenna synthesis procedure. However, this resonator is coupled with two preceding resonators (Resonator 1 and 3), simultaneously. Two coupling structures are required to achieve these couplings. Moreover, those couplings are of different types, which are capacitive and inductive, respectively. The above two problems make it very complicated for the radiator to achieve identical couplings in the replacement. For the topology shown in Figure 2.1(b), the source-to-load capacitive coupling is even unachievable in the filter-antenna synthesis, since the load becomes the free-space for an antenna. The remaining coupling topology in Figure 2.1(c) requires a multi-mode resonator to generate transmission zeros. Cross couplings between inter-cavity modes [60] are used in this topology. Based on the analysis in Section II in reference [60], a summary about the realization of TZs by

Table 2.2 Comparison between Different Methods for the Realization of Two TZs using the Cross-Coupling

	Different Resonators	Source-to-Load	Multiple Modes in a Single Resonator
Least In-Band Resonators/Modes	4	2	2
Replacement of the Last-Stage Resonator in the Filter-Antenna Synthesis	Hard	Unachievable	Easy

using this method can be drawn. All the four cases are listed in Table 2.1, where f_{sp} is the out-of-band inter-cavity spurious resonant frequency, which is differed by an amount away from the desired in-band working frequency f_0. It can be observed that, three inter-cavity modes, among which at least one is in-band, are required to generate two TZs by using this topology. It should also be pointed out that, in this topology, only one multi-mode resonator is coupled with the last-stage resonator and one coupling structure is required between them, leading to an easier replacement for the radiator in the final filter-antenna synthesis. As a result, this topology can be recognized as a promising candidate and is selected for filtering antenna designs using cavity radiators in this chapter. The reasons for the choice of multi-mode cavity for the generation of two transmission zeros are summarized in Table 2.2.

2.2.2 Reference Filter Synthesis Using Gradient-Based Optimization Method

Modeling a filter in circuit form can give a clear physical explanation of its working mechanism. However, such kind of complex circuit is not easy for the synthesis, performance simulation and reconfiguration. Fortunately, presenting a filter in the matrix form seems to be a more efficient way. The coupling matrix of a filter is more intuitive to provide the coupling scheme, which is very useful in understanding its physical realization. Each element in the matrix can be attributed to a resonator in the finished design prototype. More information of the elements, such as the Q values for each resonator cavity, different dispersion characteristics for the various types of coupling/cross-coupling within the filter, can be obtained.

As noticed in Figure 2.1(c), the coupling scheme is an asymmetric structure, in order to achieve desirable frequency responses with minimum number of elements. Conventional synthesis techniques published in [61-65] are not applicable for our case, as it is very hard to converge [66]. As a result, computer-based optimizations are preferred and also more efficient for the synthesis.

In general, to synthesize the filter by optimizing it with a certain method, a computer-aided analysis (CAA) model is required for the prescribed filter topology. The scattering parameters are assumed to be $S_{21}^{CAA}(f, \underline{\Phi})$ and $S_{11}^{CAA}(f, \underline{\Phi})$, which are obtained by a CAA model for a typical filter topology with two ports. f is the frequency. $\underline{\Phi}$ stands for all design variables of the prescribed filter topology, whose values are to be obtained by optimization. In this thesis, a commonly used least-square objective function is defined for the optimization work

$$U(f,\underline{\Phi}) = \left\{ \sum_{i=1}^{I} \left| S_{21}^{CAA}\left(f_i,\underline{\Phi}\right) - S_{21}\left(f_i\right) \right|^2 + \sum_{i=1}^{J} \left| S_{11}^{CAA}\left(f_i,\underline{\Phi}\right) - S_{11}\left(f_i\right) \right|^2 \right\} \tag{2.1}$$

where $S_{21}(f_i)$ and $S_{11}(f_j)$ are the objective filter frequency responses at sample frequencies f_i and f_j, respectively and can be expressed as

$$S_{21}^{CAA} = -2 \times j \times \left[A\right]_{(n+2)1}^{-1} \tag{2.2}$$

$$S_{11}^{CAA} = 1 + 2 \times j \times \left[A\right]_{11}^{-1} \tag{2.3}$$

with $[A]=-j[q]+\Omega[B]+[M]$, where $[q]$ is an $(n+2) \times (n+2)$ matrix with all entries zero, except for $q_{11}=1$ and $q_{(n+2)(n+2)}=1$. Ω is the normalized lowpass frequency variables, $[B]$ is the $(n+2)\times(n+2)$ unit matrix with $B_{11}=0$ and $B_{(n+2)(n+2)}=0$, and $[M]$ is the general coupling matrix, which is an $(n+2)\times(n+2)$ reciprocal matrix (i.e., $M_{ij}= M_{ji}$).

By searching for a set of optimized design variables defined in $\underline{\Phi}$ using a proper optimization approach which can minimize the error function of (2.1), a filter can be synthesized in a matrix form. In order to evaluate the filter performance during each optimization loop, computer-based analysis techniques need to be implemented. In the optimization, frequency responses obtained from the analysis are compared with objective frequency responses, at sample frequencies. If the results fail to meet the desired specifications, the frequency responses will be analyzed and compared with objective performance again, with a modification of designable parameters. This sequence of optimization [67–69] will be performed iteratively until the performance of the filter is acceptable. It is seen from the above description that, the optimization procedure can be recognized as the realization of a minimized value for the scalar objective function $U(\Phi)$.

In the designs described in following sections, this gradient-based method is used for the optimization of the coupling matrix. The derivatives of an objective function with respect to the designable parameters are used in this method. In the design space, the direction of the largest rate of decrease of the objective function at a certain point is the direction of its negative gradient, which can be calculated with the use of derivatives. In this thesis, the n designable parameters are expressed as a column vector

$$\underline{\Phi} = \left[\phi_1 \quad \phi_2 \quad \dots \quad \phi_n\right]^t \tag{2.4}$$

where t denotes the transposition of matrix. By implementing the Taylor series expansion to the objective function, we can obtain

$$U\left(\underline{\Phi} + \Delta\underline{\Phi}\right) = U\left(\underline{\Phi}\right) + \nabla U^t \cdot \Delta\underline{\Phi} + \frac{1}{2}\Delta\Phi^t \left[H\right] \Delta\underline{\Phi} + \dots \tag{2.5}$$

where

$$\Delta\underline{\Phi} = \left[\Delta\phi_1 \quad \Delta\phi_2 \quad \dots \quad \Delta\phi_n\right]^t \tag{2.6}$$

$$\nabla U = \left[\frac{\partial U}{\partial \phi_1} \quad \frac{\partial U}{\partial \phi_2} \quad \dots \quad \frac{\partial U}{\partial \varphi_n}\right]^t \tag{2.7}$$

$$[H]=\begin{bmatrix} \frac{\partial^2 U}{\partial \phi_1^2} & \frac{\partial^2 U}{\partial \phi_1 \partial \phi_2} & \cdots & \frac{\partial^2 U}{\partial \phi_1 \partial \phi_n} \\ \frac{\partial^2 U}{\partial \phi_2 \partial \phi_1} & \frac{\partial^2 U}{\partial \phi_2^2} & \cdots & \frac{\partial^2 U}{\partial \phi_2 \partial \phi_n} \\ \vdots & \vdots & \vdots & \vdots \\ \frac{\partial^2 U}{\partial \phi_n \partial \phi_1} & \frac{\partial^2 U}{\partial \phi_n \partial \phi_2} & \cdots & \frac{\partial^2 U}{\partial \phi_n^2} \end{bmatrix} \tag{2.8}$$

The column vector $\triangle \underline{\Phi}$ is called the increment vector, ∇U is the gradient vector and $[H]$ is known as the Hessian matrix.

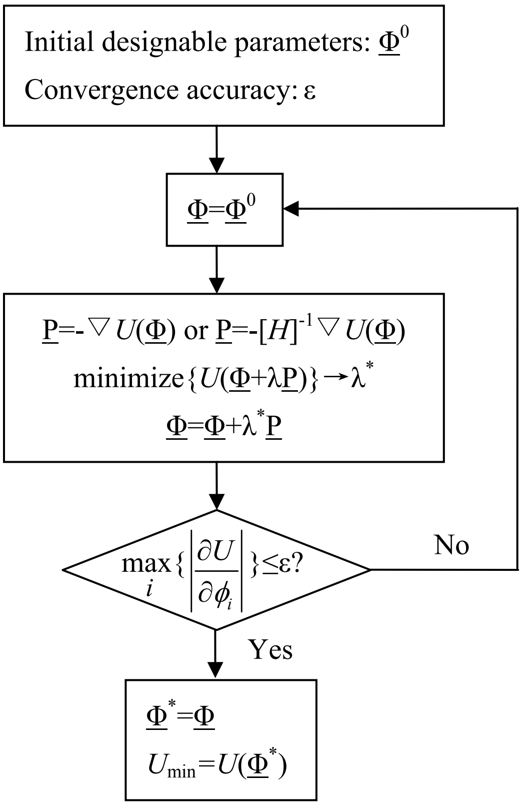

Figure 2.2 Flow of the gradient-based optimization algorithm.

Figure 2.2 illustrates the algorithm for the gradient-based optimization, where λ is a scale parameter known as the step length. Its optimum value denoted by λ^* is obtained by one-dimensional optimization.

The two formulas of *P* in Figure 2.2 are searching directions of the first- and second-order approximation of (2.5) results.

The first-order approximation of (2.5) results in a simple gradient-based optimization method known as the steepest descent method. In this method, the search for the minimum of the objective function is based on the direction

$$\underline{P} = -\nabla U \tag{2.9}$$

If the second order approximation is made in (2.5), a method known as Newton–Raphson method can be formulated. The searching direction in this method is defined by

$$\underline{P} = -\left[H\right]^{-1} \nabla U \tag{2.10}$$

where [*H*]–1 is the inverse of the Hessian matrix.

2.3 A 3-D Millimeter-Wave Filtering Antenna with High Selectivity and Low Cross-Polarization

In this section, a 3-D filtering antenna with features of high selectivity and low cross-polarization is presented. Two major contributions have been made. The first one is realizing two radiation nulls at either side of the passband of the filtering antenna, by using cross-coupling between in-band and out-of-band modes within a single cavity. The second one is realizing low cross polarization by using a dual-slot cavity-backed antenna. This dual-slot antenna performs as both the radiator and the

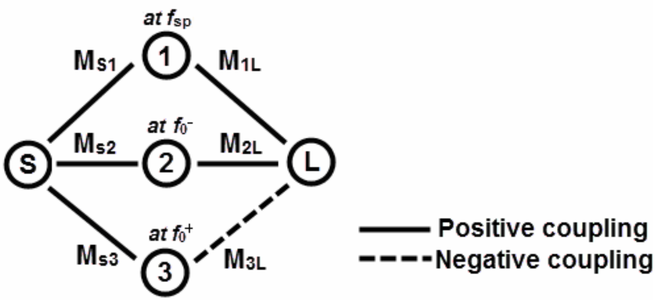

(a)

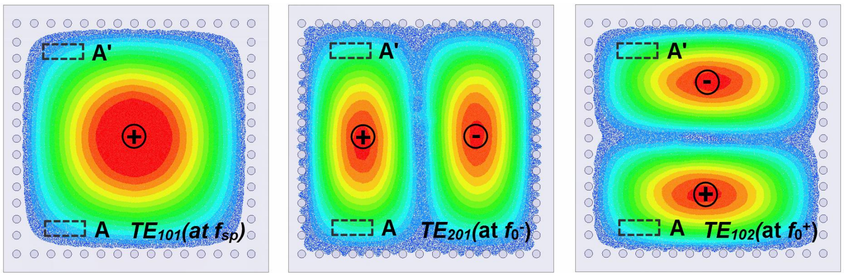

(b)

Figure 2.3 (a) Proposed coupling scheme exhibiting two transmission zeros. (b) Electric field distributions of the spurious TE_{101} mode and resonant TE_{102} & TE_{201} modes in a nearly square SIW cavity.

last resonator in the proposed filtering antenna. A prototype operating at *Ka*-band is demonstrated. The detailed design procedures and measurement results are described in the following sections.

2.3.1 Design of A Single Cavity to Realize a Coupling Scheme with Two Out-of-Band TZs

Conventionally, in order to obtain two TZs at each side of the resonant frequency using one cavity resonator, some slots are required to realize more modes or coupling paths in its coupling scheme [70], [71]. However, a cavity design without any extra structure is preferred for a more efficient implementation, especially for mm-Wave applications. A coupling scheme, which can enable two TZs and be realized inside a single resonant cavity without using additional structures stated above, is plotted in Figure 2.3(a). As can be seen, there is a spurious node f_{sp} located out of the passband of this cavity, as well as two in-band nodes located at f_0^+ and f_0^-, separately. It has already been demonstrated in [60] that, the introduction of a spurious node can generate a TZ with proper cross-coupling between the spurious node and one in-band node (f_0^- in our case). Another transmission zero in our design can be achieved since the input and output are in phase for the node resonating at f_0^- , while they are out of phase for f_0^+ [72]. Therefore, if the above topology can be achieved and those resonating nodes are properly coupled, there would be two TZs locating at each side out of the passband.

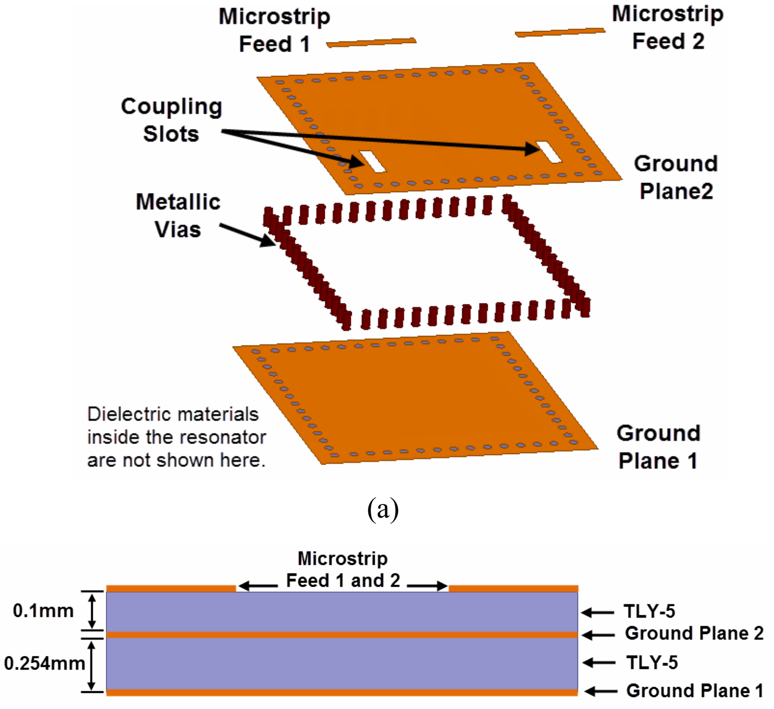

(a)

(b)

Figure 2.4 (a) 3-D view and (b) side-view of the proposed single-cavity with two transmission zeros fed by microstrip lines.

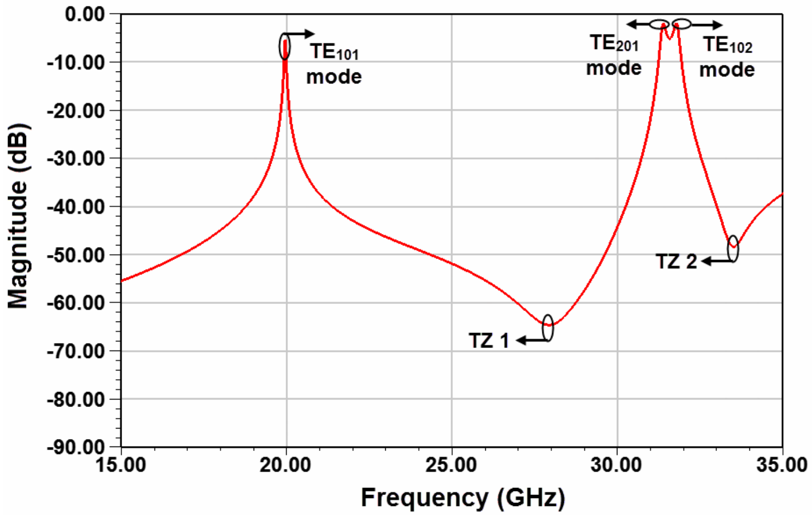

Figure 2.5 Simulated $|S_{21}|$ results of the proposed single-cavity with two TZs.

In our design, a single cavity with in-band TE_{102} & TE_{201} resonance and out-of-band TE_{101} resonance is used for the physical realization of the topology in Figure 2.3(a). Figure 2.3(b) illustrates field distributions of the above modes to describe related working mechanisms. In this cavity, the TE_{101} mode can be treated as the spurious node. The transmission zero in our design below the passband is realized by the cross-coupling between the TE_{101} and TE_{201} modes. Moreover, as can be seen, the input & output are located at regions A&A' in our design, to enable the couplings of the input & output to the TE_{201} mode to be of same signs, while enable the couplings of the input & output to the TE_{102} mode to be of opposite signs. Consequently, another transmission zero can be obtained by the cross-coupling between the TE_{201} and TE_{102} modes.

A physical model as shown in Figure 2.4 is built to verify the above analysis. Two 50 Ω microstrip lines located at regions A&A' are used to excite the cavity through two slots. Two layers of Taconic TLY-5 substrate are utilized for the design. The relative permittivity for the substrate is 2.2, while its loss tangent is 0.0009. Simulated $|S_{21}|$ results are shown in Figure 2.5. It should be noted that, the results are obtained under weak external couplings. Two TZs that are located at either side of the passband can be clearly observed.

2.3.2 A Low Cross-Polarization Antenna Realized using the Dual-Slot Structure and Backed by a Cavity

A single slot antenna backed by a TE_{102} cavity is proposed in [73] and later improved into the dual-slot form in [74] for a larger radiation gain performance. It is noted in [73] and [44] that, either the radiator or the feed has not been placed symmetrically with respect to the center of the cavity, which will worsen the cross-

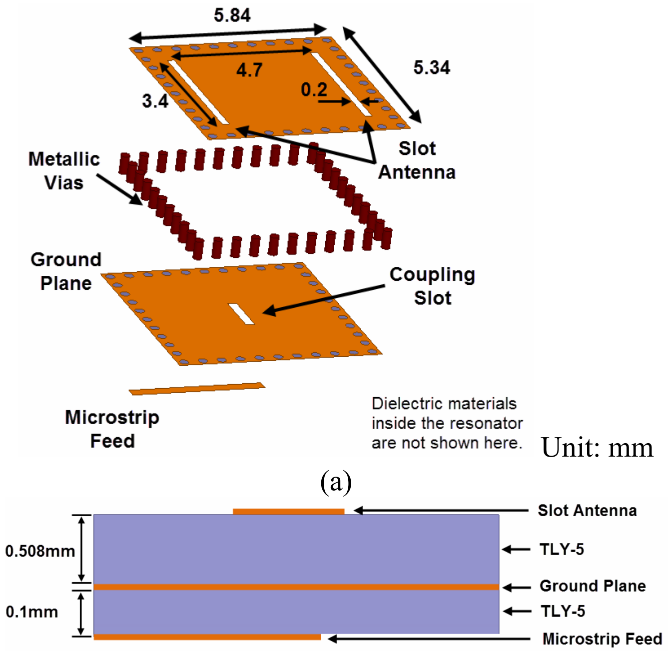

(a)

(b)

Figure 2.6 (a) 3-D view and (b) side view of the proposed dual-slot antenna backed by a cavity.

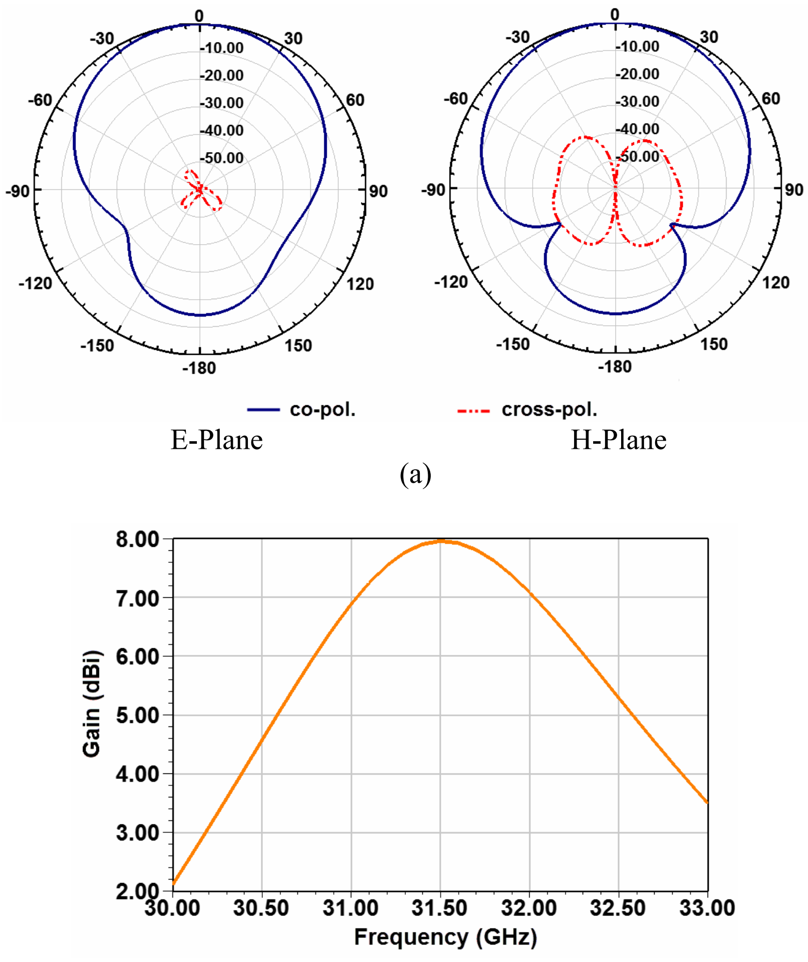

E-Plane H-Plane

(a)

(b)

Figure 2.7 (a) Radiation patterns and (b) gain responses of the proposed dual-slot antenna operating at 31.5 GHz.

polarization performance of those antennas. An improved structure, whose coupling slot used for the excitation is located at the center of the ground, is proposed in Figure 2.6. A low cross-polarization level can be estimated, since the two radiation slots and the coupling slot are all symmetric with respect to the center of the cavity.

A prototype is constructed and centered at 31.5 GHz to verify its performance. A 50 Ω microstrip line is used for the excitation through the external coupling slot. Geometry parameters of the antenna are all illustrated in Figure 2.6. The achieved bandwidth in simulation is about 700 MHz. As shown in Figure 2.7, a cross-polarization level of 50 dB lower than the co-polarization level and gain of 8 dBi are obtained at its broadside direction.

2.3.3 Design of Reference Filter and Its Corresponding Filter-Antenna Synthesis

By synthesizing the proposed multi-mode cavity in Section 2.3.1 and the dual-slot antenna backed by a cavity in Section 2.3.2, a filtering antenna with two nulls at its gain response and low cross-polarization levels can be achieved. In this section, a prototype operating at *Ka*-band is designed. A 3rd-order bandpass reference filter needs to be designed before conducting the filter-antenna synthesis.

Figure 2.8 illustrates the coupling scheme of the reference filter. It can be physically realized as shown in Figure 2.9. The structure shown in Figure 2.9 is composed of two layers of substrate using the TLY-5 material, while another layer of *fast*Rise 28 prepreg is inserted between them for the adherence. A multi-mode cavity and a single-mode cavity are located in the lower and upper TLY-5 substrate, respectively. 50-Ω microstrip lines are used for the excitations. Coupling slot 2 is used to realize the internal coupling.

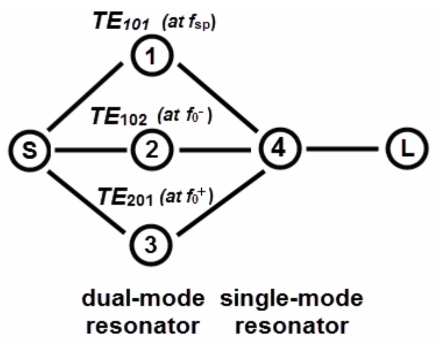

Figure 2.8 Proposed third-order coupling scheme for a reference BPF with two TZs.

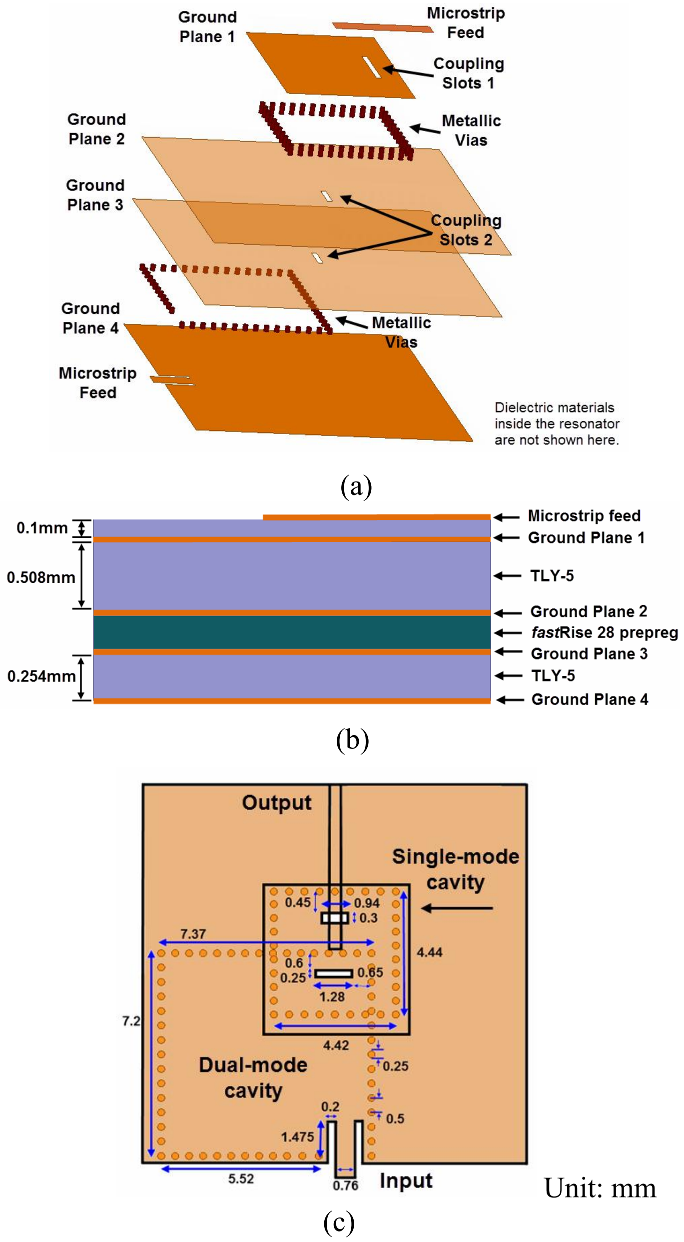

(a)

(b)

(c)

Figure 2.9 (a) Cross-section view, (b) side view and (c) top view of a three-pole cavity BPF.

The diameter of the metallic vias is 0.25 mm, while the spacing between adjacent vias is set to be 0.5 mm, in order to minimize possible radiation leakage. Based on the coupling scheme in Figure 2.8, its corresponding coupling matrix can be written as

$$M = \begin{bmatrix} 0 & M_{S1} & M_{S2} & M_{S3} & 0 & 0 \\ M_{S1} & M_{11} & 0 & 0 & M_{14} & 0 \\ M_{S2} & 0 & M_{22} & 0 & M_{24} & 0 \\ M_{S3} & 0 & 0 & M_{33} & M_{34} & 0 \\ 0 & M_{14} & M_{24} & M_{34} & M_{44} & M_{4L} \\ 0 & 0 & 0 & 0 & M_{4L} & 0 \end{bmatrix}$$

By enforcing $|S_{21}|$ obtained from the above coupling matrix to be zero, the locations of the two TZs can be determined as

$$\Omega_{z\pm} = (-b \pm \sqrt{b^2 - 4ac})/2a \tag{2.11a}$$

where

$$a = M_{14}M_{S1} + M_{24}M_{S2} + M_{34}M_{S3} \tag{2.11b}$$

$$b = M_{11}(M_{24}M_{S2} + M_{34}M_{S3}) + M_{22}(M_{14}M_{S1}$$

$$+ M_{34}M_{S3}) + M_{33}(M_{14}M_{S1} + M_{24}M_{S2}) \tag{2.11c}$$

$$c = M_{11}M_{22}M_{S3}M_{34} + M_{11}M_{33}M_{S2}M_{24}$$

$$+ M_{22}M_{33}M_{S1}M_{14} \tag{2.11d}$$

The offset between the central frequency and their median is

$$\Omega_m = \frac{\Omega_{z+} + \Omega_{z-}}{2} = -[M_{11}(M_{24}M_{S2} + M_{34}M_{S3})$$

$$+ M_{22}(M_{14}M_{S1} + M_{34}M_{S3}) + M_{33}(M_{14}M_{S1}$$

$$+ M_{24}M_{S2})]/2(M_{14}M_{S1} + M_{24}M_{S2}$$

$$+M_{34}M_{S3}) \tag{2.12}$$

It can be clearly observed that, the two transmission zeros are not symmetrically located around the passband. Since M_{11} represents the self-coupling coefficient of the spurious node, whose value is usually much larger than M_{22} and M_{33}, Ω_m can be approximately rewritten as

$$\Omega_m \approx M_{11}(M_{24}M_{S2}+M_{34}M_{S3})/2(M_{14}M_{S1}+M_{24}M_{S2}+M_{34}M_{S3}) \tag{2.13}$$

In (2.13), the value of M_{S2}, M_{S3} and M_{24} are all positive, while the value of M_{34} is negative. Therefore, when $M_{24} = -M_{34}$ and $M_{S2} = M_{S3}$ are both satisfied, a pair of transmission zeros nearly symmetric ($\Omega_m \approx 0$) can be achieved. In order to physically achieve the above two conditions, positions for the internal slot and the external one should be located at places where the field density is almost identical for both node 2 (TE_{102}) and node 3 (TE_{201}), as shown in Figure 2.9.

The specifications for this design are: BW=500 MHz, f_0=31.5 GHz, in-band $|S_{11}|$<-15 dB, f_{TZ1}=29.5 GHz, f_{TZ2}=33.3 GHz. It should be pointed out that these two transmission zeros are intended to be symmetrically located out of the passband. Optimization-based approach is performed here to obtain the generalized coupling matrix for this filter and the S-parameters of this topology can be described as

$$S_{21}^{CAA} = -2\times j\times\left[A\right]_{6,1}^{-1} \tag{2.14}$$

$$S_{11}^{CAA} = 1+2\times j\times\left[A\right]_{1,1}^{-1} \tag{2.15}$$

$$[A]=\begin{bmatrix} -j & 0 & 0 & 0 & 0 & 0 \\ 0 & \Omega & 0 & 0 & 0 & 0 \\ 0 & 0 & \Omega & 0 & 0 & 0 \\ 0 & 0 & 0 & \Omega & 0 & 0 \\ 0 & 0 & 0 & 0 & \Omega & 0 \\ 0 & 0 & 0 & 0 & 0 & -j \end{bmatrix}+\begin{bmatrix} 0 & M_{S1} & M_{S2} & M_{S2} & 0 & 0 \\ M_{S1} & M_{11} & 0 & 0 & M_{14} & 0 \\ M_{S2} & 0 & M_{22} & 0 & M_{24} & 0 \\ M_{S2} & 0 & 0 & M_{33} & -M_{24} & 0 \\ 0 & M_{14} & M_{24} & -M_{24} & M_{44} & M_{4L} \\ 0 & 0 & 0 & 0 & M_{4L} & 0 \end{bmatrix} \qquad (2.16)$$

Following constraints have been applied to parameters in the coupling matrix: M_{S2}=M_{S3} and M_{24}= -M_{34} based on the analysis described above. All the diagonal elements in the coupling matrix will also have nonzero entry values. Therefore, there are nine unknown design parameters in the optimization and are defined as

$$\underline{\Phi}=\begin{bmatrix} M_{S1} & M_{S2} & M_{14} & M_{24} & M_{4L} & M_{11} & M_{22} & M_{33} & M_{44} \end{bmatrix} \qquad (2.17)$$

Most of the initial values in $\underline{\Phi}$ related to mode 2, 3 and 4 can be estimated from a Chebyshev filter. When considering the physical constrain between operating frequencies of different modes in a resonant cavity, and assuming mode 2 (TE_{102}) and mode 3 (TE_{201}) in Figure 2.8 resonate at f_0, the initial value of M_{11} can also be estimated. Detailed values are given as below:

$$\underline{\Phi}^{\text{initial}}=\begin{bmatrix} 0 & 0.74 & 0 & 0.919 & 1.037 & 113.75 & 0 & 0 & 0 \end{bmatrix} \qquad (2.18)$$

(2.1) is used as the error function for our synthesis example at some chosen characteristic frequencies. Optimized results obtained from the above synthesis are

$$\underline{\Phi}^*=\begin{bmatrix} 1.316 & 1.005 & 1.316 & 1.101 & 1.425 & 118.998 & 1.512 & -1.587 & 0.039 \end{bmatrix} \qquad (2.19)$$

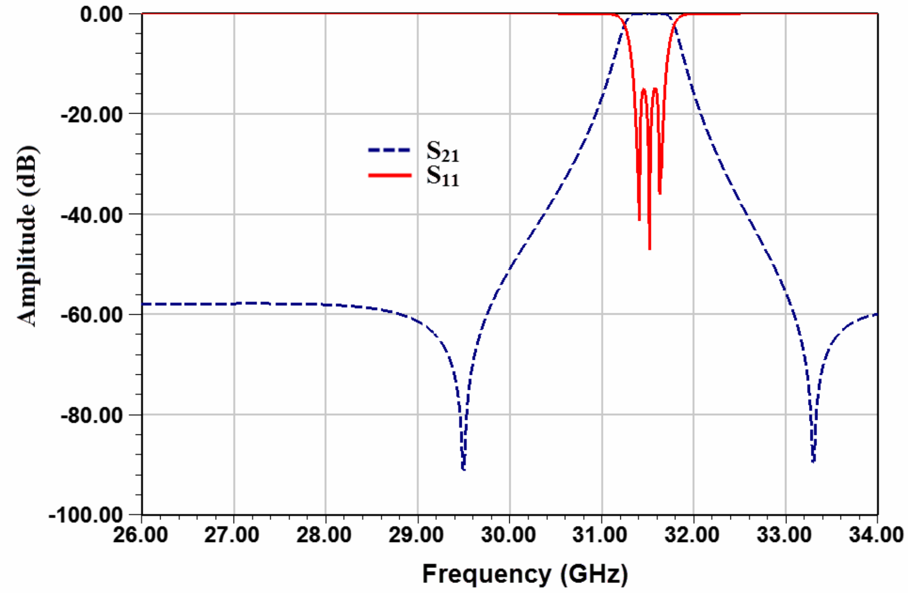

Figure 2.10 Calculated frequency responses using optimized parameters.

The corresponding coupling matrix for this filter can be given:

$$\mathbf{M} = \left[\begin{array}{ccccccc} & S & 1 & 2 & 3 & 4 & L \\ S & 0 & 1.316 & 1.005 & 1.005 & 0 & 0 \\ 1 & 1.316 & 118.998 & 0 & 0 & 1.316 & 0 \\ 2 & 1.005 & 0 & 1.512 & 0 & 1.101 & 0 \\ 3 & 1.005 & 0 & 0 & -1.587 & -1.101 & 0 \\ 4 & 0 & 1.316 & 1.101 & -1.101 & 0.039 & 1.425 \\ L & 0 & 0 & 0 & 0 & 1.425 & 0 \end{array}\right]$$

Figure 2.10 plots calculated frequency responses using optimized parameters. Then, the generalized coupling matrix is de-normalized by using the following formulas:

$$k_{ij}= FBW\times M_{\mathrm{ij}} \qquad Q_{\mathrm{en}}=\frac{1}{FBW\times \mathrm{M}_{\mathrm{sn}}^{2}} \qquad FBW=\frac{BW}{f_0} \tag{2.20}$$

where k_{ij} is the internal coupling coefficients between operating modes in each cavity, Q_{en} is the external quality factors for each operating mode, FBW is the fractional bandwidth, BW is the absolute bandwidth and f_0 is the center frequency of the passband.

After desired design parameters are obtained, the resonant frequencies f for each in-band mode in this BPF can be determined from the coupling matrix by:

$$k_{ii} = \frac{f_0}{f} - \frac{f}{f_0} \tag{2.21}$$

The external quality factors for each in-band mode (Q_{e2}, Q_{e3} and Q_{e4}) in this bandpass filter (BPF) are extracted in simulation to meet those desired values. The external quality factors are extracted from simulation by [75]:

$$Q_e = \frac{2f_{res}}{\Delta f_{3dB}} \tag{2.22}$$

where f_{res} is the frequency at which S_{21} reaches its maximum value and $\triangle f_{\mathrm{3dB}}$ is the 3-dB bandwidth for which S_{21} is reduced by 3 dB from its maximum value. The internal coupling coefficients k_{ij} can be obtained from full-wave simulations as follows [75]:

$$k_{ij} = \frac{f_{p2}^{\;2} - f_{p1}^{\;2}}{f_{p2}^{\;2} + f_{p1}^{\;2}} \tag{2.23}$$

where f_{p1} and f_{p2} are the two characteristic frequencies that are the resonant frequencies in the transmission response of the coupled structure under weak external couplings. It should be pointed out that, when tuning the geometry of the filter using procedures described above, a priority of the physical realization is given to those design specifications related to in-band responses. The summary of all design parameters are given in Figure 2.9(c). EM field distributions of different modes at passband edges in the two cavities are plotted as in Figure 2.12. It can be observed

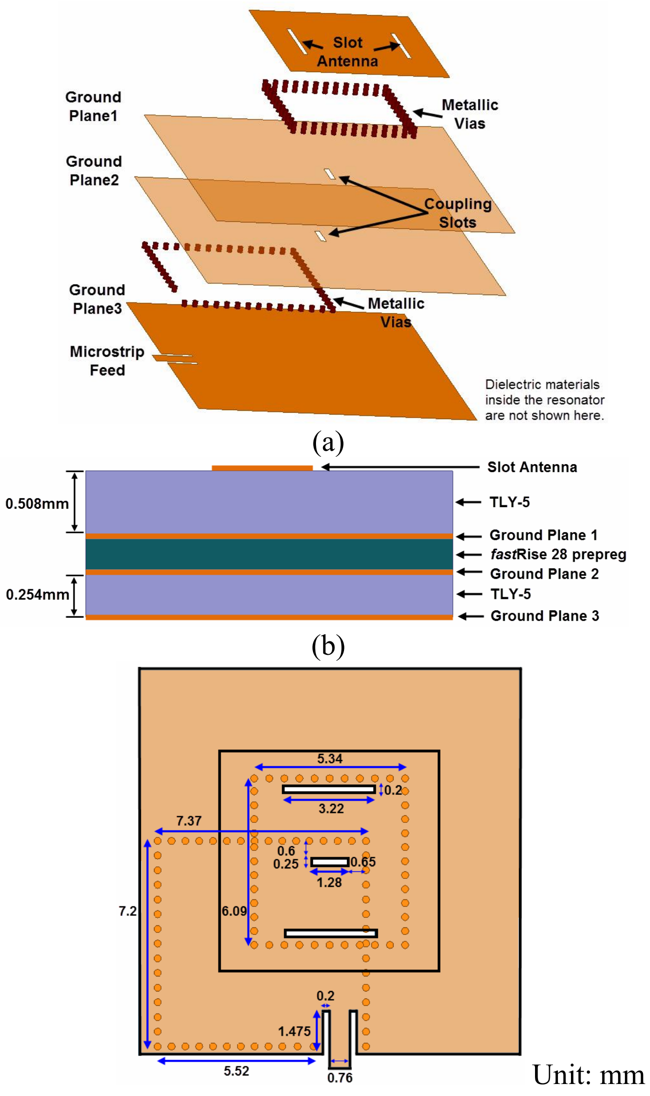

(a)

(b)

(c)

Figure 2.11 Geometry of the proposed filtering antenna. (a) 3-D view, (b) side view and (c) top view.

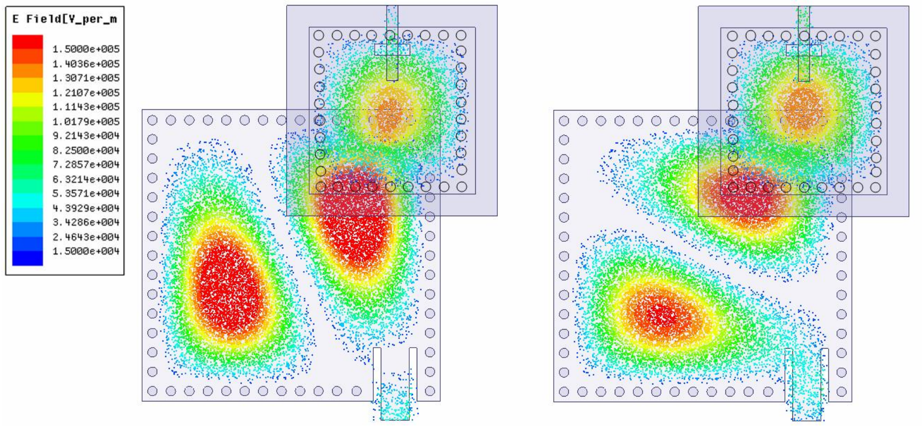

(a) (b)

Figure 2.12 EM field distributions in resonant cavities at (a) 31.25 GHz and (b) 31.75 GHz.

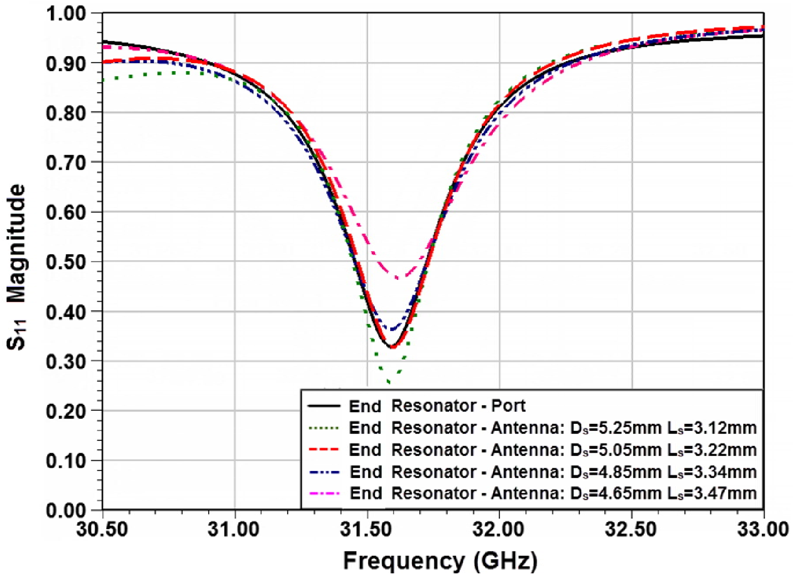

Figure 2.13 Reflection coefficients of the waveguide port 1 for the end resonator of either a single-mode cavity in the filter or a dual-slot antenna backed by a cavity in the filtering antenna.

that, resonant modes in the dual-mode cavity changes from TE_{201} mode to TE_{102} mode along with the incensement of frequency, while resonant mode in the single-mode cavity remains to be TE_{101} mode.

After the reference filter has been established, a filter-antenna synthesis is required to be applied for the construction of a filtering antenna. It is already known that, the bandwidth for the dual-slot cavity-backed antenna is about 700 MHz, which is wider than the required bandwidth of 500 MHz in design specifications. Based on the analysis discussed in [27], this larger bandwidth can enable this antenna to act as an equivalent resonator to the filter within the passband, as long as the coupling between the lower multi-mode cavity resonator and the antenna is identical to that between the

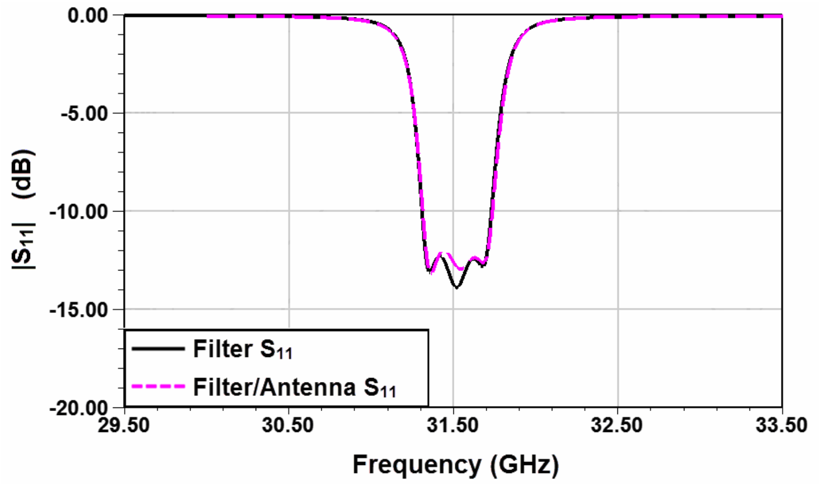

Figure 2.14 Simulated $|S_{11}|$ results of the filter and filtering antenna.

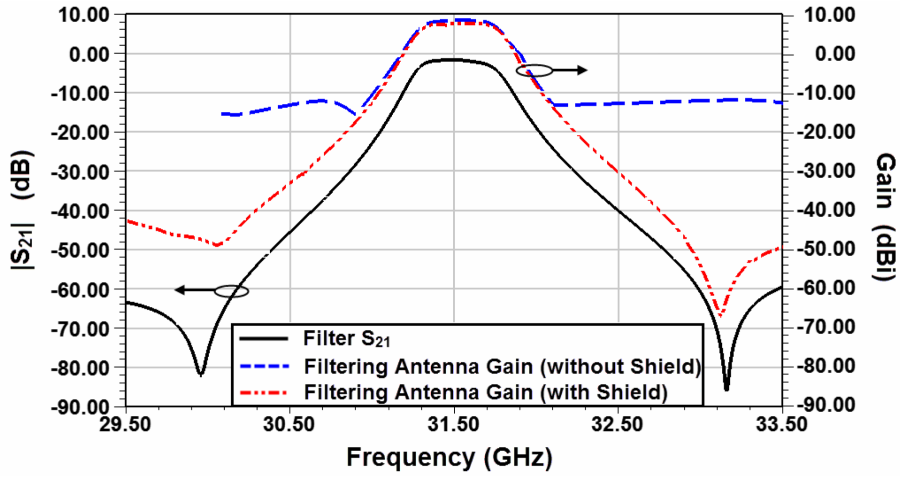

Figure 2.15 Simulated $|S_{21}|$ results of the filter and gain of the filtering antenna.

multi-mode cavity and the single-mode one, and identical external quality factor can be obtained for the radiator in the filtering antenna and the end resonator of the filter.

The above two considerations can be evaluated at the same time, using a waveguide port to excite the end resonator through the coupling slot [28]. A dielectric material of ε_r=20 is filled in the waveguide to enable a smaller cross-section. The waveguide is coupled with the internal coupling slot of the end-resonators for both cases. The waveguide port is named as Port 1 so that the reflection coefficients are S_{11}. In order to match the $|S_{11}|$ results between the filter and the filtering antenna, a parameter study with D_s and L_s is conducted. Simulated magnitudes of S_{11} versus different parameters are plotted in Figure 2.13. Simulated results for the reference filter case are illustrated in the solid line. Results for each combination of D_s and L_s for the filtering antenna case are illustrated in the dashed/dotted lines. As can be observed, when D_s=5.05 mm and L_s=3.22 mm, results for the filtering antenna case can match the reference filter case best, which indicates that an almost identical loaded quality factor Q_L can be achieved between these two cases. Final dimensions of the proposed filtering antenna are optimized and illustrated in Figure 2.11(c).

Figure 2.14 shows the simulated return loss for the reference filter and filtering antenna. They are very close to each other which verified above synthesis procedures. The simulated working frequency band of the filtering antenna is centered at 31.52 GHz with a fractional bandwidth of 1.36%. Figure 2.15 shows the simulated gain results of the proposed filtering antenna. Due to the radiation from the microstrip line feed on the ground plane 3 in Figure 2.11, the gain results do not roll off as sharp as the $|S_{21}|$ results of the filter. Therefore, a metallic cavity shield is designed and located on top of the ground plane 3 to prevent this radiation leakage. By taking this measure, a better match can be achieved between the solid line and the dot-dot-dashed line in Figure 2.15.

2.3.4 Measurement Results and Discussions

Photograph of the fabricated prototype is shown in Figure 2.16. A 2.92mm southwest super SMA connector is utilized for the measurement of the input impedances. A metallic cavity is also implemented to shield the radiation leakage from the microstrip feed. A comparison between measured and simulated $|S_{11}|$ of

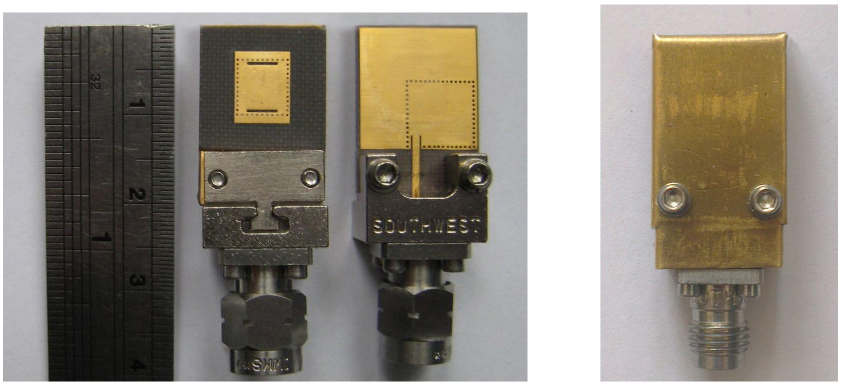

(a) (b)

Figure 2.16 (a) Top and bottom views of the fabricated prototype. (b) Fabricated antenna enclosed by a metallic cavity.

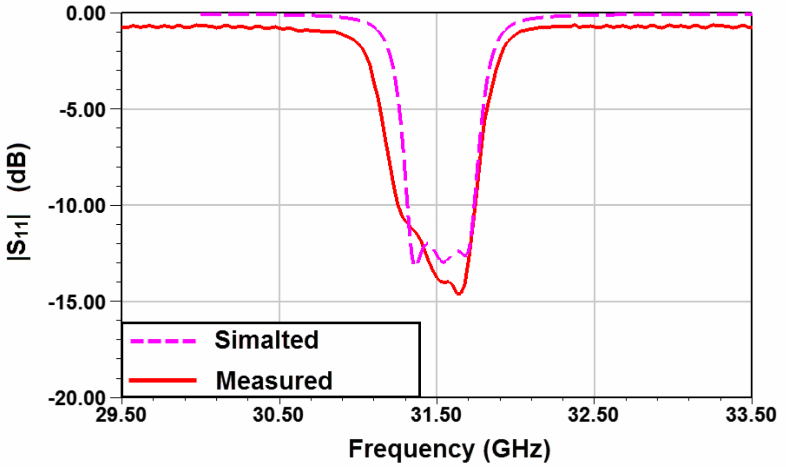

Figure 2.17 Simulated and measured $|S_{11}|$ of the proposed filtering antenna.

the filtering antenna is plotted in Figure 2.17. The center working frequency is 31.495 GHz and very close to the simulated 31.52 GHz. Measured bandwidth for $|S_{11}|<-10$ dB is from 31.25 GHz to 31.74 GHz, which is slightly larger than the simulated one. The small discrepancy between the measured and simulated $|S_{11}|$ results may be resulted by the effect of the feeding super SMA connector and the fabrication tolerance of multi-layer PCB process at millimeter-wave range. An anechoic chamber is used for the far-field measurement. Measured gain values are

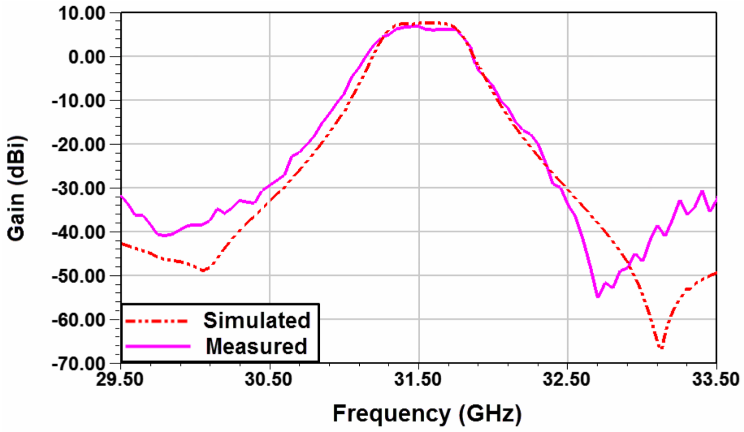

Figure 2.18 Simulated and measured broadside gain results of the proposed filtering antenna.

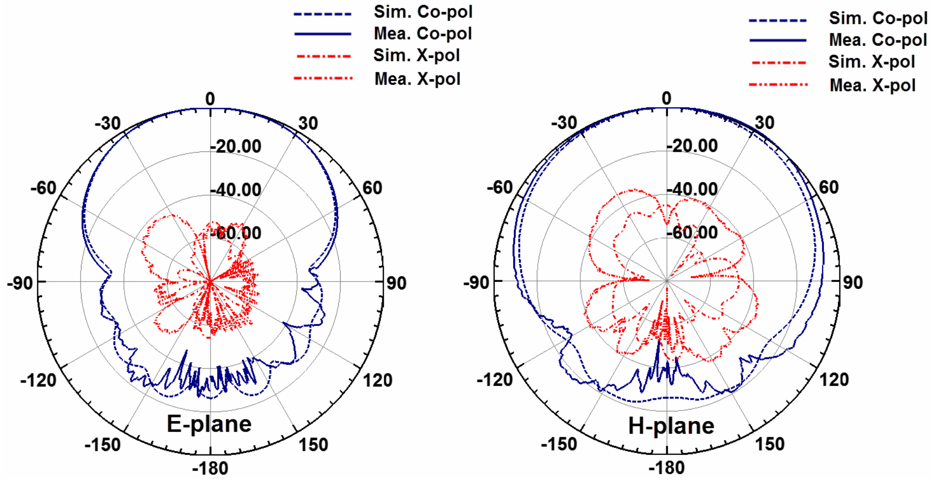

Figure 2.19 Simulated and measured radiation patterns at 31.5 GHz for the proposed filtering antenna.

obtained at the broadside of the proposed filtering antenna. The measured maximum gain within the passband is 6.79 dBi [as shown in Figure 2.18], in which the connector loss has been included. A good matching has been achieved between simulation and measurement in Figure 2.18 as well. Radiation patterns for the frequency of 31.5 GHz are plotted in Figure 2.19. Measured cross-polarization level is about 30 dB lower than the co-polarization at the broadside of the antenna.

2.4 An SIW Filtering Antenna Array with Quasi-Elliptic Gain Response

In this section, an SIW filtering antenna array with quasi-elliptic gain responses is presented. The proposed design is based on the cross-coupling between different operation modes inside a substrate integrated waveguide (SIW) cavity. Two radiation nulls are generated in the gain curve at each side of the antenna's passband. Firstly, a two-output filter is designed as a reference, in which an oversized TE_{103}-mode cavity resonator is utilized for the generation of transmission zeros and realization of power division. Afterwards, cavity-backed slot antennas are used to replace resonators coupled with the two outputs in the reference filter, so that a filtering antenna array can be obtained. The complexity of our design is relatively low, due to the implementation of the oversized cavity. A *Ka*-band prototype is demonstrated. The

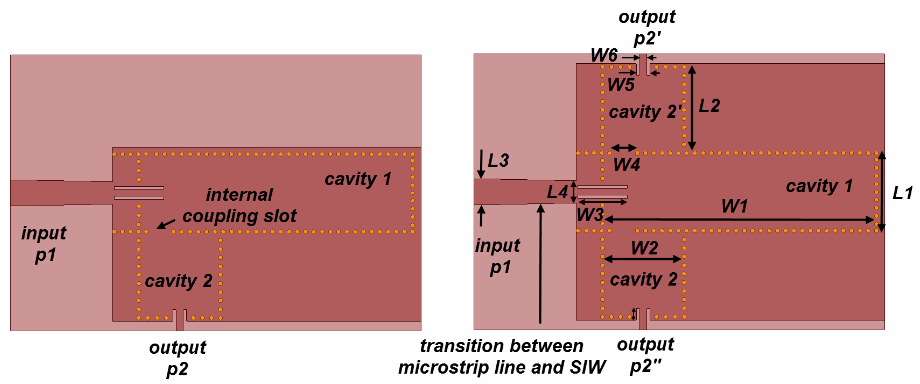

(a) (b)

Figure 2.20 The geometric configuration of (a) a one-output filter and (b) the proposed two-output filter with quasi-elliptic response. $L1$=4.8mm, $L2$=5.34mm, $L3$=1.6mm, $L4$=1.4mm, $W1$=16.8mm, $W2$=5mm, $W3$=3.14mm, $W4$=1.68mm, $W5$=0.85mm, $W6$=0.45mm.

proposed antenna array with filtering characteristics is very suitable for the integration with other millimeter-wave circuits.

2.4.1 A Two-Output Reference Filter with Quasi-Elliptic Response

The physical layout of the proposed two-output reference filter is plotted in Figure 2.20(b). This filter is extended from a one-output filter shown in Figure 2.20(a). Two TE_{101}-mode cavities [cavity 2 and cavity 2'] and one TE_{103}-mode cavity [cavity 1] are included. Desired transmission zeros (TZs) are generated by the cross-coupling between those out-of-band TE_{102} and TE_{104} modes in this TE_{103}-mode cavity. 100 Ω microstrip lines are used for the excitation of two TE_{101} cavities, while a waveguide together with a mixed grounded coplanar waveguide (GCPW) coupling structure is used to excite the TE_{103} cavity. A transition is also designed at the input side for the power transmission between the mircrostrip line and waveguide. The following two

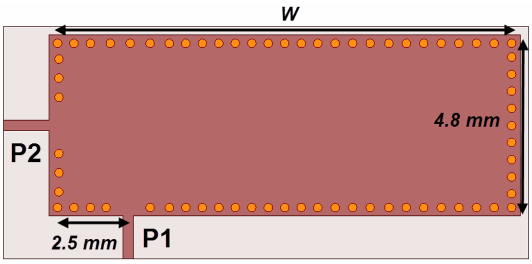

Figure 2.21 Geometry and feed arrangement of the TE_{103}-mode Cavity

issues have been taken into considerations for the design of this two-output reference filter.

1) Generation of Two Transmission Zeros (TZs) within A Single Cavity: Figure 2.21 shows the model of the TE_{103}-mode cavity used in this design, together with its corresponding excitation arrangement. Transmission zeros (TZs) at each side of the in-band resonance of TE_{103} mode can be achieved, by taking the advantage of cross-couplings between different in-band and out-of-band inter-cavity modes. The summary about TZ realizations and locations in different cases when using this method has already been given in Table 2.1. In the cavity shown in Figure 2.21, both TE_{102} and TE_{104} modes are treated as spurious resonances, while TE_{103} mode is the in-band resonance. Figure 2.22 plots field distributions for the above three modes. Both case 1 and case 4 can be satisfied, as long as the input and output are located at regions A and B illustrated in Figure 2.22. The details are explained below.

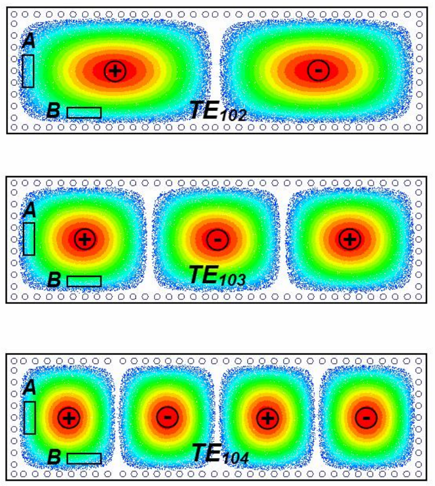

Figure 2.22 Electric field distributions of TE_{102}, TE_{103} and TE_{104} modes in a single cavity.

For modes TE_{102} and TE_{103}, the relationship between the input and output are both in phase. When the TE_{103}-mode is treated as the in-band resonance and TE_{104}-mode is treated as the spurious one, the requirement described in case 1, Table 2.1 can be fulfilled, which means a TZ above the passband can be generated. Similarly, the relationship between in-band TE_{103} mode and out-of-band TE_{102} mode can meet the requirement described as case 4 in Table 2.1. Consequently, a TZ below the passband can be realized. The dashed lines plotted in Figure 2.23 illustrates simulated S-parameter results for the cavity model in Figure 2.21, when W=16.8 mm. It can be observed that, the TE_{103} mode of this cavity resonates at 28.1 GHz. Meanwhile, there is one TZ between the resonances of TE_{102} and TE_{103} modes, as well as another one between the modes of TE_{103} and TE_{104}. Furthermore, TZs can be observed at either

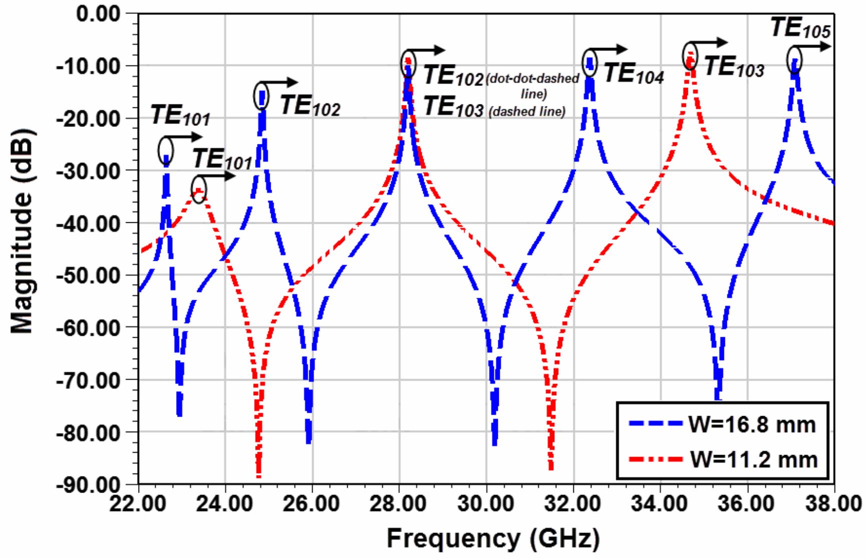

Figure 2.23 Simulated S-parameter results of cavities with the feed arrangement shown in Figure 2.22, whose resonance at 28.1 GHz is of TE_{102} mode (dashed line) and TE_{103} mode (dot-dot-dashed line), separately.

Table 2.3 Frequency Distance between Adjacent Transmission Zeros

Mode at Center Frequency	Frequency Distance Between Adjacent Transmission Zeros	
TE_{102}	4.8 GHz (with respect to TE_{101})	6.5 GHz (with respect to TE_{103})
TE_{103}	3.3 GHz (with respect to TE_{102})	4.2 GHz (with respect to TE_{104})
TE_{104}	2.6 GHz (with respect to TE_{103})	3.1 GHz (with respect to TE_{105})

side of the TE_{102} mode resonance as well, which means the cavity width can be shortened so as to allocate the TE_{102} mode at 28.1 GHz. Figure 2.23 also plots simulated results for W=11.2 mm with dot-dot-dashed lines. When comparing to results from a larger cavity [W=16.8 mm], the frequency distance between adjacent TZs is larger which results in a worse selectivity [plotted in Table 2.3]. On the contrary, sharper cutoff skirts can be achieved when TE_{104} mode of this cavity

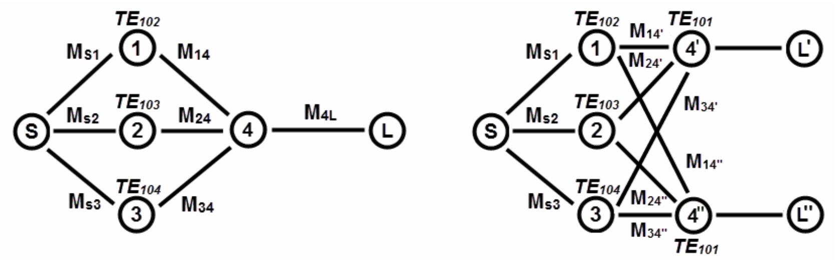

(a) (b)

Figure 2.24 Coupling schemes of (a) a 2nd-order bandpass filter and (b) a 2nd-order two-output filter extended from the previous filter.

resonates at 28.1 GHz [listed in Table 2.3], while the cavity size needs to be enlarged. In this design, the in-band resonance is chosen to resonate at TE_{103} mode for a trade-off between the cavity size and performance of selectivity.

2) Design of a Two-Output Filter with Quasi-Elliptic Response: After the resonant mode of the oversized cavity is determined, the detailed design of the proposed two-output filter will start from its one-output counterpart, whose coupling scheme is plotted in Figure 2.24 (a). As already shown in Figure 2.20(a), this one-output filter consists of one TE_{103}-mode cavity analyzed above and one TE_{101}-mode cavity. In order to obtain a proper coupling, the internal coupling slot is located at region B in the TE_{103}-mode cavity, while the input is located at region A.

By enforcing $|S_{21}|$ obtained from the above coupling scheme to be zero, the locations of the two TZs can be determined as

$$\Omega_{z\pm} = [a \pm b] / [2(M_{14}M_{1S} + M_{24}M_{2S} + M_{34}M_{3S})] \tag{2.24a}$$

where

$$a = -(M_{24}M_{2S} + M_{34}M_{3S})M_{11} - (M_{14}M_{1S}$$

$$+M_{24}M_{2S})M_{33} \qquad (2.24b)$$

$$b = \{[(M_{24}M_{2S} + M_{34}M_{3S})M_{11} + (M_{14}M_{1S}$$

$$+M_{24}M_{2S})M_{33}]^2 - 4\times(M_{14}M_{1S} + M_{24}M_{2S}$$

$$+M_{34}M_{3S})\times M_{24}M_{11}M_{2S}M_{33}\}^{1/2} \qquad (2.22c)$$

This pair of TZs is not symmetrically located around the passband and the distance between their median and the central frequency is

$$\Omega_m = \frac{\Omega_{z+} + \Omega_{z-}}{2} = -[(M_{24}M_{2S} + M_{34}M_{3S})M_{11} + (M_{14}M_{1S}$$

$$+M_{24}M_{2S})M_{33}] / 2\left(M_{14}M_{1S} + M_{24}M_{2S}\right.$$

$$\left.+M_{34}M_{3S}\right) \qquad (2.25)$$

Obviously, a pair of TZs symmetric ($\Omega_m = 0$) can be obtained when the conditions shown below are both satisfied:

$$M_{11} = -M_{33} \qquad (2.26)$$

$$M_{14}M_{1S} = M_{34}M_{3S} \qquad (2.27)$$

M_{ii} is the self coupling co-efficiencies which can be expressed by

$$M_{ii} = \frac{1}{FBW}\left(\frac{f_0}{f_i} - \frac{f_i}{f_0}\right) \qquad (2.28)$$

where *FBW* is the fractional bandwidth, f_0 is the center frequency of the passband and f_i is the resonant frequency for each resonant mode. By using (2.28), equation (2.26) can be re-written as

$$\frac{f_2}{f_1}-\frac{f_1}{f_2}=-(\frac{f_2}{f_3}-\frac{f_3}{f_2}) \tag{2.29}$$

which will be satisfied when

$$f_2^2=f_1f_3 \tag{2.30}$$

Meanwhile, the resonant frequencies for each mode can be physically achieved by optimizing the cavity size, based on the equations below:

$$f_1=\frac{c}{2\pi\sqrt{\mu_r\varepsilon_r}}\sqrt{\left(\frac{\pi}{L}\right)^2+\left(\frac{2\pi}{W}\right)^2} \tag{2.31}$$

$$f_2=\frac{c}{2\pi\sqrt{\mu_r\varepsilon_r}}\sqrt{\left(\frac{\pi}{L}\right)^2+\left(\frac{3\pi}{W}\right)^2} \tag{2.32}$$

$$f_3=\frac{c}{2\pi\sqrt{\mu_r\varepsilon_r}}\sqrt{\left(\frac{\pi}{L}\right)^2+\left(\frac{4\pi}{W}\right)^2} \tag{2.33}$$

where μ_r and ε_r are the relative permeability and relative permittivity of the cavity substrate, c is the speed of light in free space. Based on (2.30)-(2.33), it can be calculated that equation (2.26) will be fulfilled when $W/L \approx 2.92$.

Equation (2.27) can be rewritten in the form of

$$\frac{M_{1S}}{M_{3S}}=\frac{M_{34}}{M_{14}} \tag{2.34}$$

Since both the location of input port 1 and the input coupling density related to *W3* has already been fixed to meet the required $M_{2\mathrm{S}}$, which also leads to a fixed ratio of $M_{1\mathrm{S}}/M_{3\mathrm{S}}$, we have to satisfy (2.34) by adjusting the value of M_{34}/M_{14}. In Figure 2.22, it can be observed from the electric field distributions around the internal coupling slot at region B that, when moving the internal coupling slot away from the input side, the electric field becomes stronger for the TE_{102} mode and weaker for the TE_{104} mode, which will result in a smaller value for M_{34}/M_{14}. On the contrary, the value of M_{34}/M_{14} will be increased when moving the internal coupling slot towards the input.

Design specifications of the one-output reference filter in this design are listed below: The center frequency is f_0=27.95 GHz, the fractional bandwidth is FBW= 1.25%, two transmission zeros are at $\pm 11.1j$, and the in-band reflection coefficient is smaller than 20 dB. Since the initial size of cavity 1 can be determined based on the above analysis, those out-of-band transmission poles corresponding to TE_{102} and TE_{104} modes of cavity 1 can be obtained as well, which are at $\pm 70j$ in this case. The generalized coupling matrix is optimized to be:

$$M = \left[\begin{array}{ccccccc} & S & 1 & 2 & 3 & 4 & L \\ S & 0 & 1.1038 & 1.4675 & 2.9752 & 0 & 0 \\ 1 & 1.1038 & 66.9959 & 0 & 0 & 3.0171 & 0 \\ 2 & 1.4675 & 0 & 0 & 0 & 2.3842 & 0 \\ 3 & 2.9752 & 0 & 0 & -66.9969 & 1.1031 & 0 \\ 4 & 0 & 3.0171 & 2.3842 & 1.1031 & 0 & 1.4598 \\ L & 0 & 0 & 0 & 0 & 1.4598 & 0 \end{array}\right]$$

The values in the coupling scheme [shown in Figure 2.24(b)] for the two-output filter can be extracted from its one-output counterpart by keeping power transmitted to loads to be the same:

$$M_{14'} = M_{14''} = M_{14} / \sqrt{2} \tag{2.35}$$

$$M_{24'} = M_{24''} = M_{24} / \sqrt{2} \tag{2.36}$$

$$M_{34'} = M_{34''} = M_{34} / \sqrt{2} \tag{2.37}$$

A 20 mil Rogers 5880 substrate with its relative permittivity of 2.2 and loss tangent

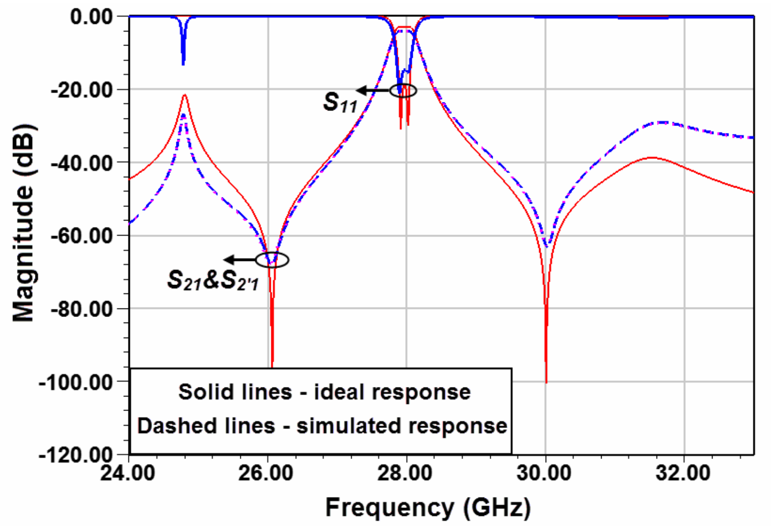

Figure 2.25 Frequency responses of the two-output filter.

0.0009 is used for the physical realization of the two-output reference filter. The diameter of metallic vias is 0.25 mm, while the space between adjacent ones is 0.5 mm. Those initial design parameters can then be obtained by de-normalizing the coupling matrix [75]. The ratio of $W1/L1$ is initially set to be 2.92 when Cavity 1 resonates at TE_{103}. Cavities 2 and 2' both resonate at their TE_{101} mode. In order to achieve a quasi-elliptic response with symmetric TZs, locations of those internal coupling slots need to be optimized first. Then, by using the HFSS simulator, the whole filter is tuned to obtain desired frequency responses. Finalized parameters are given in Figure 2.20. Figure 2.25 shows simulated frequency responses of the two-output reference filter, in which a good correspondence can be observed with responses from its ideal circuit.

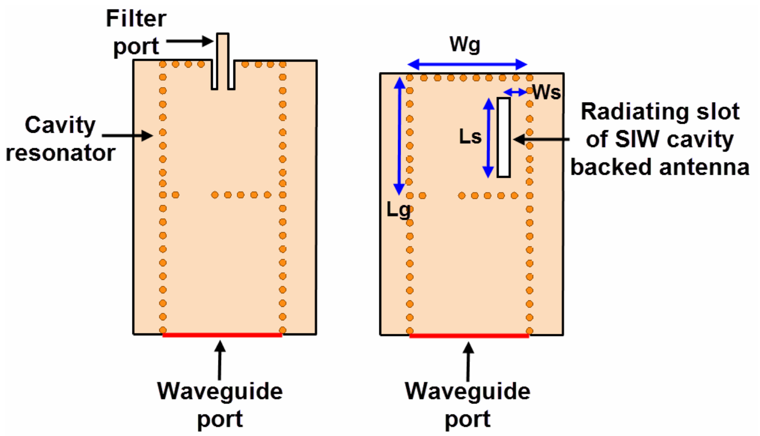

(a) (b)

Figure 2.26 Schematics of simulation models used for evaluating the reflection coefficients of a waveguide port used to excite (a) a cavity resonator with a filter port and (b) an SIW cavity-backed slot antenna.

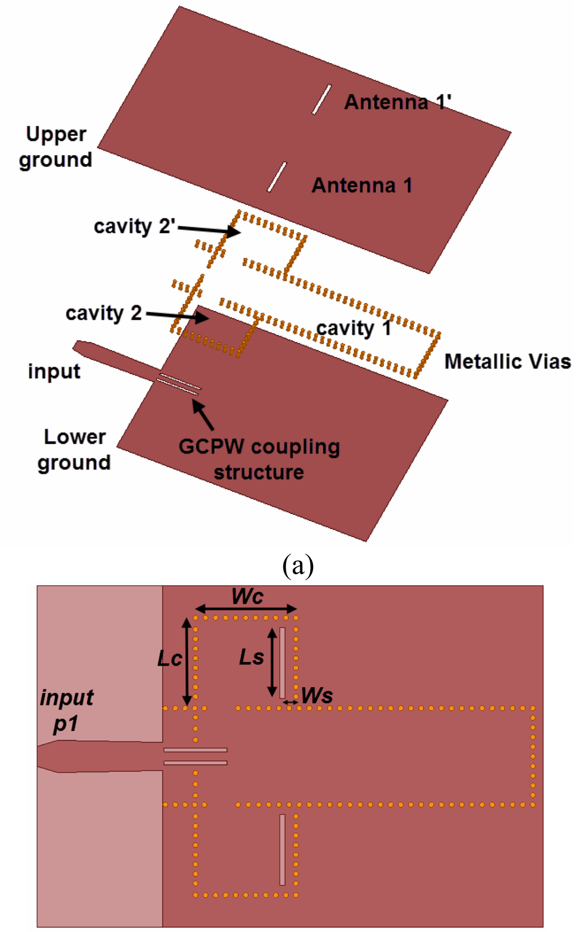

(a)

(b)

Figure 2.27 (a) Cross-section view and (b) geometrical parameters of the proposed filtering antenna array. *Lc*=4.5mm, *Ls*=3.54mm, *Wc*=5mm, *Ws*=0.66mm.

2.4.2 Filtering Antenna Array Synthesis

It is possible for an SIW cavity-backed slot antenna to act as an equivalent load to the filter, because the bandwidth for this antenna is larger than the required 1.25%fractional bandwidth in this design. To this aim, the coupling between the TE_{103}-mode cavity and the antenna unit need to be identical to that between the TE_{103}-mode cavity and the TE_{101}-mode one. Meanwhile, the same external quality factor needs to be obtained between the TE_{101}-mode cavity of the reference filter and the antenna unit. The above two considerations can be evaluated at the same time, by using the method described in [28]. A waveguide port [assumed to be port 1] will be used to excite the cavity resonator with a filter port [shown in Figure 2.26 (a)] and the cavity-backed slot antenna [shown in Figure 2.26 (b)], to compare their reflection coefficients. The cavity size for the antenna is fixed to be W_g=5 mm and L_g=4.5 mm. A parameter study will be conducted versus W_s and L_g to match the reflection coefficients in the above two cases. The best matching is found when L_s=3.535 mm and W_s=0.66 mm, in which the reflection coefficients for both cases are close to each other within a wide frequency range. After the above evaluations have been done, cavity-backed antennas are used to replace the end resonators in the reference filter, and a desired filtering antenna array can be successfully established as shown in Figure 2.27.

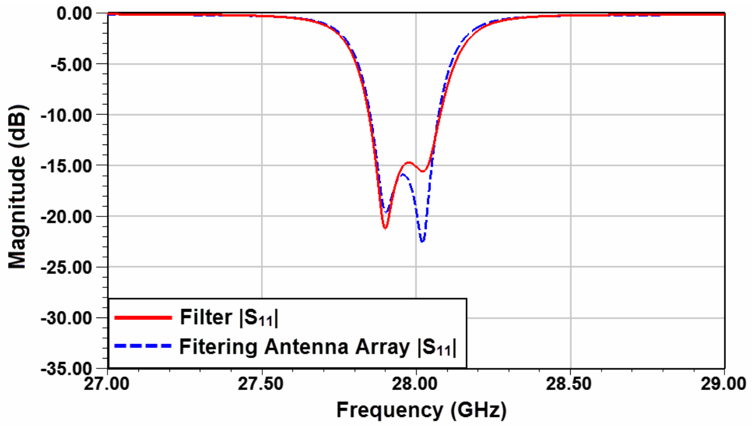

Figure 2.28 Simulated $|S_{11}|$ results of the filter and filtering antenna array.

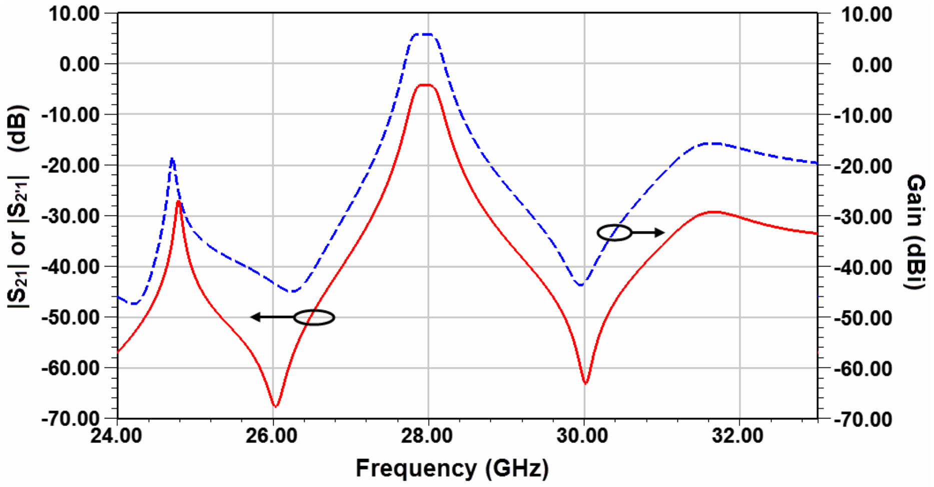

Figure 2.29 Simulated $|S_{21}|$ results of the filter and gain of the filtering antenna array.

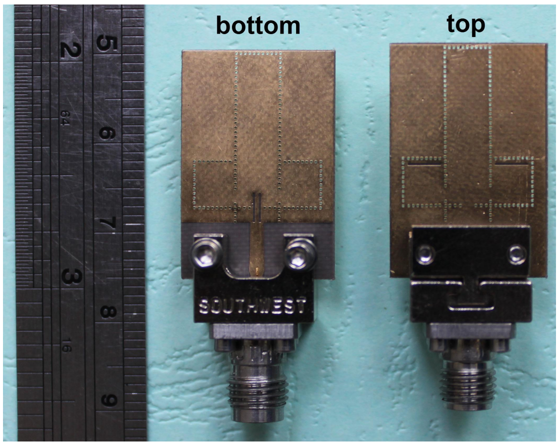

Figure 2.30 Top and bottom views of the fabricated filtering antenna array.

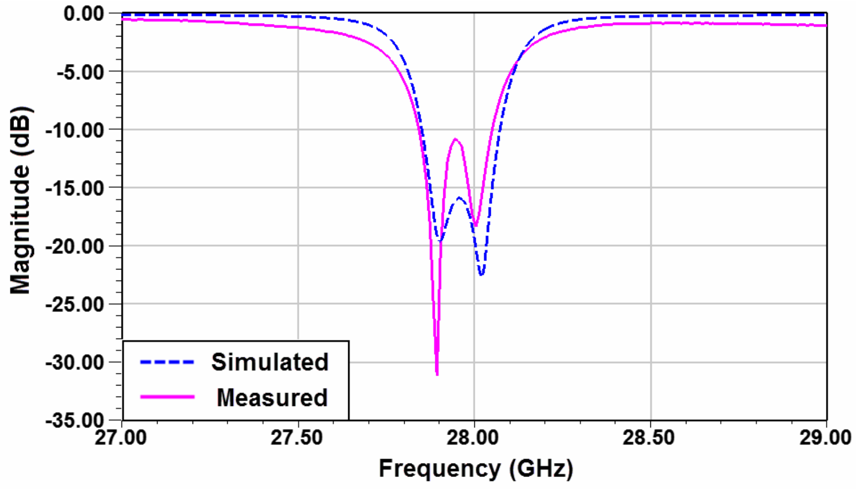

Figure 2.31 Simulated and measured $|S_{11}|$ results of the filtering antenna array.

In Figure 2.27, the feeding microstrip line is designed at the opposite side with respect to the radiating slots, in order to avoid possible radiation leakage from it. Parameters of the optimized filtering antenna are given in Figure 2.27. Figure 2.28 compares simulated reflection coefficients of the proposed filtering antenna array and its two-output reference filter. It can be observed that, they operate at the same working frequency with almost identical bandwidth. In-band return loss values are both better than 15 dB. Two radiation nulls can be observed at the gain curve of the filtering antenna array shown in Figure 2.29, whose locations are almost the same as those in its reference filter.

2.4.3 Measurement Results and Discussions

The photograph of the fabricated prototype is shown in Figure 2.30. A 2.92mm southwest super SMA connector is used for the measurement. Measured reflection

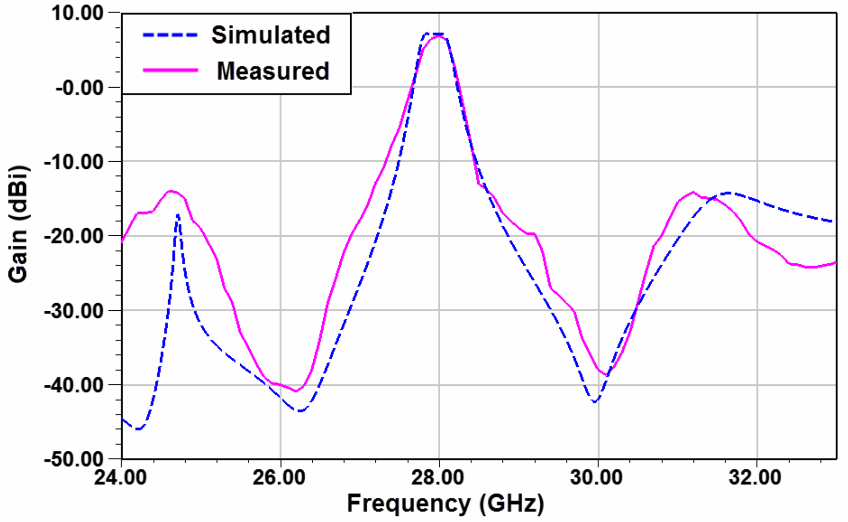

Figure 2.32 Simulated and measured gain of the filtering antenna array.

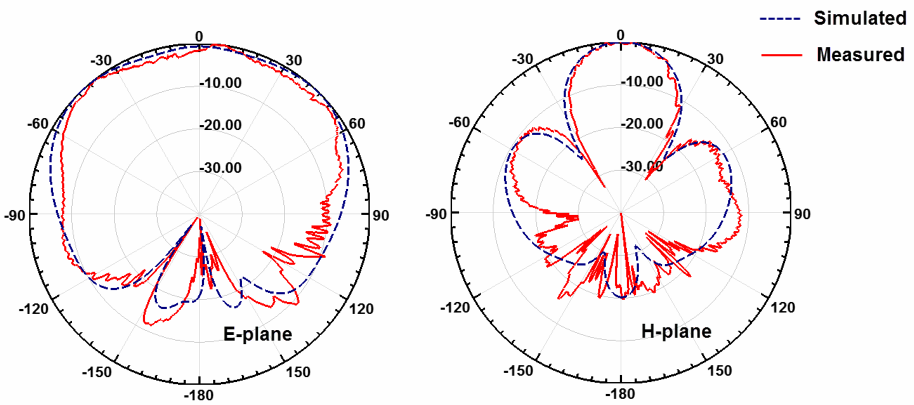

Figure 2.33 Simulated and measured radiation patterns of the proposed filtering antenna array at 27.94 GHz (unit: dB)

coefficients are plotted in Figure 2.31, whose center working frequency is located at 27.94 GHz and very close to the simulation. Measured bandwidth is from 27.85 GHz to 28.03 GHz, which is slightly smaller than the simulated one. An anechoic chamber is used for the measurement of the antenna's far-field performance. The measured maximum gain is 6.8 dBi as shown in Figure 2.32 within the passband. Meanwhile, the measured gain curve also basically follows the shape of transmission coefficients of the reference filter. Measured radiation patterns at 27.94 GHz are plotted in Figure 2.33.

2.5 Summary

A complete approach for the aim of improving the selectivity of cavity-based filtering antennas is proposed and analyzed in this chapter. Cross-couplings inside a single multi-mode cavity are selected as the TZ generation method in a reference filter to realize radiation nulls in its corresponding filtering antenna, due to its easy implementation to the filter-antenna synthesis procedure. Design specifications of these reference filters are synthesized by the gradient-based optimization method. Two design examples, which are separately an element and an array, are proposed and physically realized. Good correspondences can also be found between simulation and measurement.

Chapter 3 Array Designs of SIW Cavity Filtering Antennas for Specific Applications

This chapter presents two filtering antenna arrays operating at *Ka*-band, which can achieve monopulse and dual-polarization functions, respectively. All resonators and radiators in the above two designs are based on cavity structures, in order to improve the efficiency for mm-Wave applications. Detailed design procedures and analysis are described in the following sections.

3.1 Introduction

An antenna array is a set of N spatially separated antennas. The number of antennas in an array can be as small as 2, or as large as several thousand. In general, the performance of an antenna array increases with the number of antenna elements in the array, while the drawback is the increased cost, size, loss and complexity. The antenna array can be used to increase the overall gain, provide diversity transmission/reception, cancel out interference from a particular set of directions, steer the beam so that it is most sensitive in a particular direction or determine the direction of arrival of the incoming signals.

Expanding the filtering antenna concept from a single element to an array is very meaningful for practical applications. Initially almost all published articles related to filtering antenna designs are with single antenna element. Only a transmission-line based design published in 2011 by Chung *et al.* is in the array configuration [30]. The challenge lies in the design of a proper feeding network with both power-division and filtering functions. In 2015, another filtering antenna array with dual-polarization is proposed by Chu *et al*. [22]. The above two filtering antenna arrays are both based on transmission-line resonators and patch radiators, and those techniques involved in them are not suitable to be applied in SIW cavity-based designs.

3.2 A Millimeter-wave Filtering Monopulse Antenna Array Based on Substrate Integrated Waveguide Technology

For the aim of precision angle estimation in a radar tracking system, monopulse antenna arrays [76] are widely used. In conventional designs, e.g. Cassegrain parabolic antennas and lens antennas, corresponding monopulse comparators are typically bulky and heavy. To eliminate the above disadvantages, microstrip transmission-line based comparators were proposed for those lightweight and low profile designs [77-80]. However, for millimeter-wave applications, there will be large radiation losses during power transmission when using microstrip transmission-line based transmission structures. To this end, substrate integrated waveguide (SIW) based comparators [81-83], which suffers much less radiation losses, were proposed and implemented in the design of monopulse comparators in recent years.

This section presents a substrate integrated waveguide (SIW) based filtering antenna array [as shown in Figure 3.1] operating at millimeter-wave range with monopulse functions. The proposed antenna array is composed of 4 antenna elements. A monopulse comparator and necessary feeding network are also included to achieve required filtering properties. The monopulse comparator is realized by using a square dual-mode SIW cavity, whose internal coupling slots are designed along its diagonals to simultaneously achieve required internal coupling co-efficiencies for both sum and difference channels. Before the design of the proposed filtering antenna array, a reference filter with four outputs is synthesized based on its one-output counterpart. Then, four cavity-backed slot antennas are used to replace the four end-resonators in the reference filter. A *Ka*-band prototype with a center frequency of 29.25 GHz and fractional bandwidth of 1.2% is demonstrated. The sidelobe levels of the sum pattern are less than -15 dB and the null depth of the difference pattern is less than -28 dB in the *H*-plane far-field measurement. Meanwhile, for the sum channel, a maximum gain of 8.1 dBi is obtained.

3.2.1 A Four-Output Filter Composed of One Monopulse Comparator

1) Design of a Monopulse Comparator: Figure 3.2 illustrates the proposed SIW

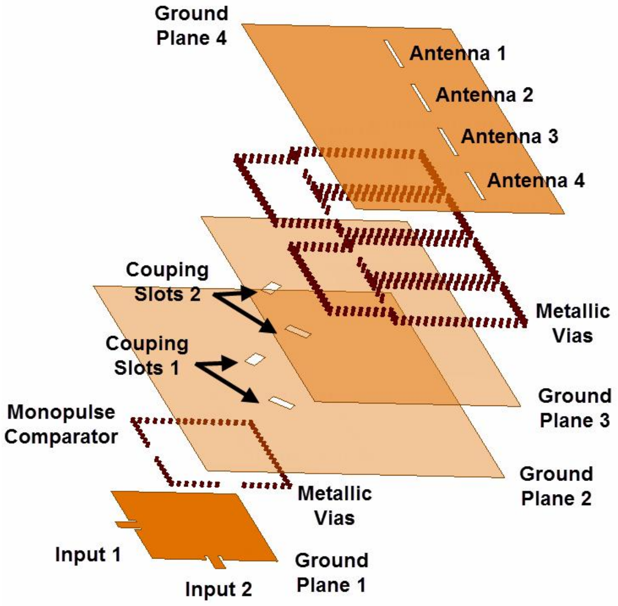

Figure 3.1 Cross-section view of the proposed filtering monopulse antenna array.

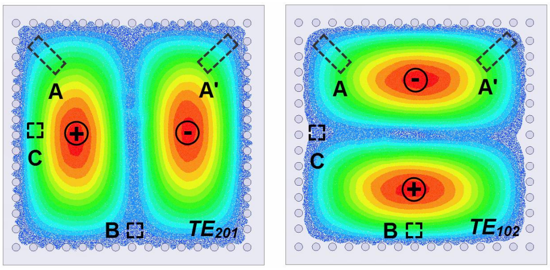

Figure 3.2 Electric field distributions of two degenerated modes (TE_{201} and TE_{102}) in the proposed monopulse comparator.

cavity-based monopulse comparator, together with electric field distributions related to its operation modes. The comparator is a square cavity resonator. The input for the TE_{201} mode is located at region C, while it is at region B for the TE_{102} mode. The outputs for both operation modes are located at regions A and A'. It can be observed from Figure 3.2 that, in region B, the electric field is strong for the TE_{102} mode but weak for the TE_{201} mode, while region C is strong for the TE_{201} mode but weak for the TE_{102} mode. Based on the above mechanism, region B can be used for the excitation of TE_{102} mode without affecting the resonance of the TE_{201} mode. If region C is used for the excitation of the TE_{201} mode, no coupling will be generated to the TE_{102} mode either.

It is also noticed that, when the TE_{201} mode is excited inside this cavity resonator, the electric field densities are identical at regions A & A', while the directions for them are opposite to each other. On the contrary, when the TE_{102} mode is excited, the electric field at regions A & A' is of the same direction and intensity. The above features can exactly meet those requirements for a monopulse comparator. Moreover, regions A & A' are both symmetrically located along the diagonal of the square cavity, for the aim of achieving the same field intensity for TE_{102} and TE_{201} modes in this comparator. This feature will contribute to achieve equal internal couplings between the comparator and resonators in the next stage for both sum and difference channels, since the proposed design is based on the same coupling scheme with same specifications.

2) Design of a Four-Output Filter: A 3rd-order Chebyshev four-output filter is designed at first, as the reference for the synthesis of a filtering monopulse antenna array with four antenna units. Figure 3.3 plots the detailed geometry of the proposed reference filter. As can be seen, two layers of TLY-5 substrate ($\varepsilon_r = 2.2$, $\tan\delta = 0.0009$) have been used, and a layer of *fast*Rise 28 prepreg ($\varepsilon_r = 2.75$) is used for the

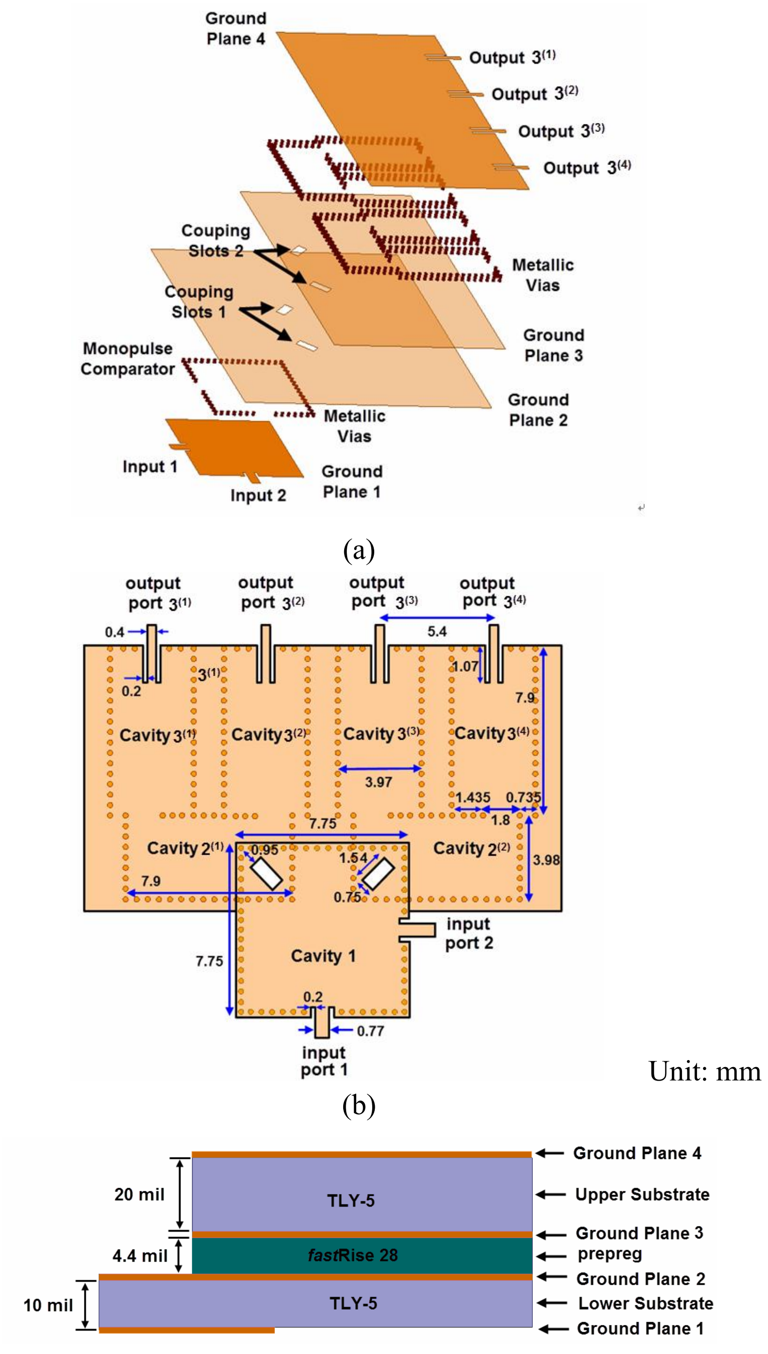

(a)

(b)

(c)

Figure 3.3 (a) Cross-section view, (b) top view and (c) side view of a four-output filter.

connection between them. In this filter, a monopulse comparator (cavity 1 in the lower substrate), two horizontal arranged TE_{101}-mode rectangular cavities (cavity 2 and $2^{(1)}$ in the upper substrate) and four vertically arranged TE_{101}-mode cavities

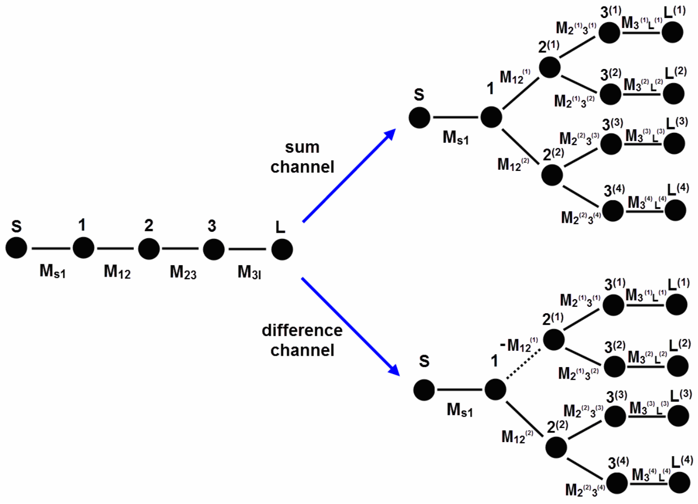

(a) (b)

Figure 3.4 Coupling schemes of (a) a three-order bandpass filter and (b) three-order four-output filters (sum and difference channel) extended from the previous filter.

(cavity $3^{(1)}$—$3^{(4)}$ in the upper substrate) are included. Microstrip lines with coupling slots are used for the excitations. In order to achieve a one-to-four power divider, two horizontally arranged rectangular cavities are connected with the comparator at regions A and A' first. Then, each horizontal arranged cavity is coupled with another two vertically arranged cavities. Port 1 is used for the excitation of the sum channel, while port 2 is for the difference channel.

A 3rd-order one-output filter shown in Figure 3.4(a) is used for the extraction of the coupling scheme for the proposed four-output reference filter shown in Figure 3.4 (b). The coupling matrix for the reference filter can be given as:

$$\mathbf{M} = \left[\begin{array}{ccccccccccccc}
 & S & 1 & 2^{(1)} & 2^{(2)} & 3^{(1)} & 3^{(2)} & 3^{(3)} & 3^{(4)} & L^{(1)} & L^{(2)} & L^{(3)} & L^{(4)} \\
S & 0 & M_{s1} & 0 & 0 & 0 & 0 & 0 & 0 & 0 & 0 & 0 & 0 \\
1 & M_{s1} & 0 & M_{12^{(1)}} & M_{12^{(2)}} & 0 & 0 & 0 & 0 & 0 & 0 & 0 & 0 \\
2^{(1)} & 0 & M_{12^{(1)}} & 0 & 0 & M_{2^{(1)}3^{(1)}} & M_{2^{(1)}3^{(2)}} & 0 & 0 & 0 & 0 & 0 & 0 \\
2^{(2)} & 0 & M_{12^{(2)}} & 0 & 0 & 0 & 0 & M_{2^{(2)}3^{(3)}} & M_{2^{(2)}3^{(4)}} & 0 & 0 & 0 & 0 \\
3^{(1)} & 0 & 0 & M_{2^{(1)}3^{(1)}} & 0 & 0 & 0 & 0 & 0 & M_{3^{(1)}L^{(1)}} & 0 & 0 & 0 \\
3^{(2)} & 0 & 0 & M_{2^{(1)}3^{(2)}} & 0 & 0 & 0 & 0 & 0 & 0 & M_{3^{(2)}L^{(2)}} & 0 & 0 \\
3^{(3)} & 0 & 0 & 0 & M_{2^{(2)}3^{(3)}} & 0 & 0 & 0 & 0 & 0 & 0 & M_{3^{(3)}L^{(3)}} & 0 \\
3^{(4)} & 0 & 0 & 0 & M_{2^{(2)}3^{(4)}} & 0 & 0 & 0 & 0 & 0 & 0 & 0 & M_{3^{(4)}L^{(4)}} \\
L^{(1)} & 0 & 0 & 0 & 0 & M_{3^{(1)}L^{(1)}} & 0 & 0 & 0 & 0 & 0 & 0 & 0 \\
L^{(2)} & 0 & 0 & 0 & 0 & 0 & M_{3^{(2)}L^{(2)}} & 0 & 0 & 0 & 0 & 0 & 0 \\
L^{(3)} & 0 & 0 & 0 & 0 & 0 & 0 & M_{3^{(3)}L^{(3)}} & 0 & 0 & 0 & 0 & 0 \\
L^{(4)} & 0 & 0 & 0 & 0 & 0 & 0 & 0 & M_{3^{(4)}L^{(4)}} & 0 & 0 & 0 & 0
\end{array}\right]$$

In the sum channel shown in Figure 3.4(b), the first node 1 and second nodes $2^{(1)}\&2^{(2)}$ all act as two-way dividers. In order to keep the total transmitted power unchanged, we can have

$$M_{12^{(1)}} = M_{12^{(2)}} = M_{12} / \sqrt{2} \tag{3.1}$$

$$M_{2^{(1)}3^{(1)}} = M_{2^{(1)}3^{(2)}} = M_{2^{(2)}3^{(3)}} = M_{2^{(2)}3^{(4)}} = M_{23} / \sqrt{2} \tag{3.2}$$

for internal coupling coefficients, and

$$M_{3^{(1)}L^{(1)}} = M_{3^{(2)}L^{(2)}} = M_{3^{(3)}L^{(3)}} = M_{3^{(4)}L^{(4)}} = M_{3L} \tag{3.3}$$

for external coupling coefficients.

For the case of the difference channel, node 1 will also act as an 180° phase shifter and we will have

$$-M_{12^{(1)}} = M_{12^{(2)}} = M_{12} / \sqrt{2} \tag{3.4}$$

in this channel. Other coupling coefficients will be kept the same as those in the sum channel.

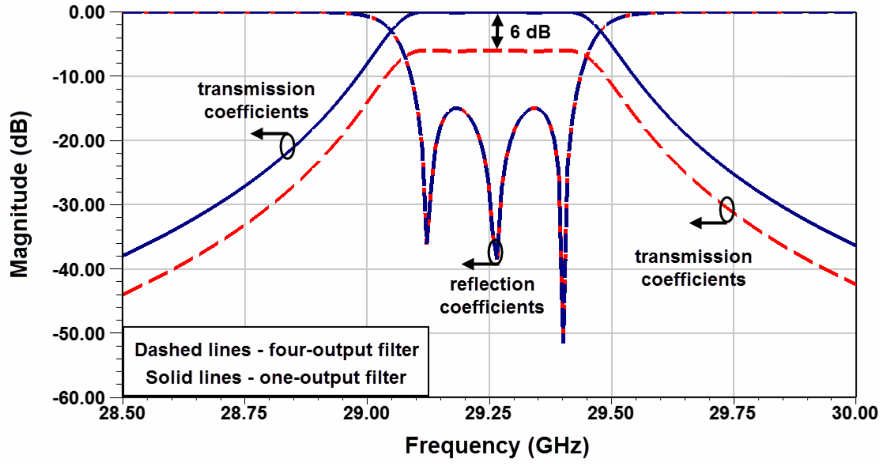

Figure 3.5 Synthesized frequency responses of the four-output filter and its one-output counterpart.

Coupling coefficients are calculated to be M_{S1}=0.9453, M_{12}=0.6223, M_{23}=0.6223, M_{3L}= 0.9453 for the four-output filter with an in-band return loss of 15 dB. The synthesized responses when f_0=29.25 GHz and BW=340 MHz is plotted in Figure 3.5. Only one curve related to the output is illustrated in this figure due to frequency responses for all the four outputs are the same. The only difference between reflection coefficients of the four-output filter and its one-output counterpart is the 6-dB difference between their transmission coefficients.

In the physical modeling of this four-output filter, the diameter and spacing of those grounded vias are 0.4 mm and 0.8 mm, respectively. By properly de-normalizing the coupling matrix, initial design parameters and physical parameters can be obtained [75] for this reference filter. The HFSS simulator is used for the optimization of the geometry parameters. Figure 3.3(b) illustrates detailed dimensions

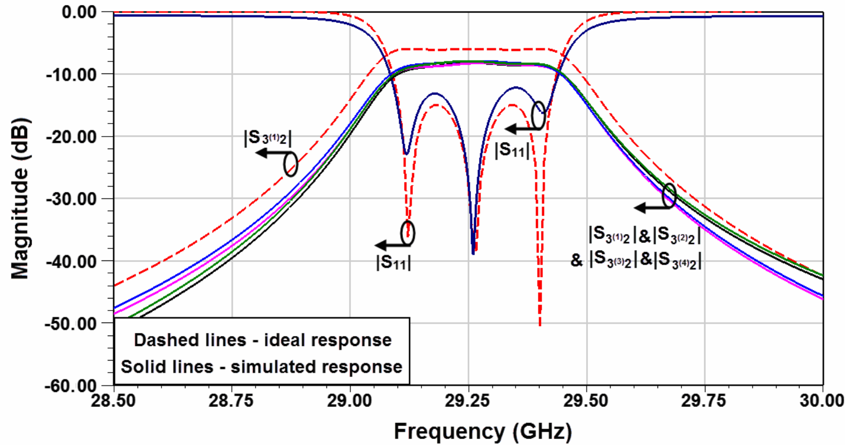

(a)

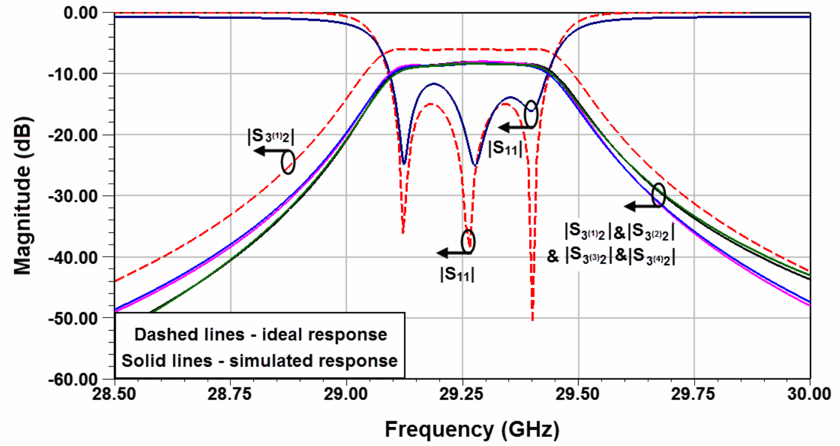

(b)

Figure 3.6 Simulated frequency responses of the four-output filter operating in the (a) difference channel and (b) sum channel.

of the whole filter. Figure 3.6 plots the frequency responses from both ideal circuit and physical model. Simulated amplitude obtained from the physical model is given in Table 3.1, in which "m" denotes the number of the output port while "n" for the input port. Simulated phases are given in Table 3.2. The largest phase different between corresponding output ports is around 2^{o} while it is 183^{o} for the difference channel, which are both very close to ideal values of 0^{o} and 180^{o}.

Table 3.1 Amplitude of S_{mn}

$dB(S_{3^{(1)}1})$	$dB(S_{3^{(2)}1})$	$dB(S_{3^{(3)}1})$	$dB(S_{3^{(4)}1})$
-8.01	-8.02	-8.28	-8.29
$dB(S_{3^{(1)}2})$	$dB(S_{3^{(2)}2})$	$dB(S_{3^{(3)}2})$	$dB(S_{3^{(4)}2})$
-8.31	-8.35	-8.14	-8.17

Table 3.2 Phase of S_{mn}

$Ang(S_{3^{(1)}1})$	$Ang(S_{3^{(2)}1})$	$Ang(S_{3^{(3)}1})$	$Ang(S_{3^{(4)}1})$
89.84°	91.02°	92.84°	91.91°
$Ang(S_{3^{(1)}2})$	$Ang(S_{3^{(2)}2})$	$Ang(S_{3^{(3)}2})$	$Ang(S_{3^{(4)}2})$
-131.2°	-130.64°	52.41	51.25

3.2.2 Filtering Monopulse Antenna Array Synthesis

In [73], the cavity-backed single slot antenna can achieve a bandwidth of about 1.7%, whose absolute value is 490 MHz and wider than the 340 MHz bandwidth of the reference filter designed in the above section. Based on the analysis in [27], as long as the same internal coupling can be acquired between the antenna unit & a cavity resonator of the second-order [nodes 2' or 2"] and an end resonator [nodes 3' or 3" or 3''' or 3''''] & a second-order one, together with the same external coupling can be acquired between the end resonator of the filter and the antenna unit, the antenna unit will perform as an equivalent load to the filter as the end resonator. The above two considerations can be evaluated in the same procedure using the method in [28] and models for this evaluation are given in Figure 3.7. By changing W_s and L_g [W_g=4.5 mm is fixed], $|S_{11}|$ of the end resonator in the filter case is adjusted to match

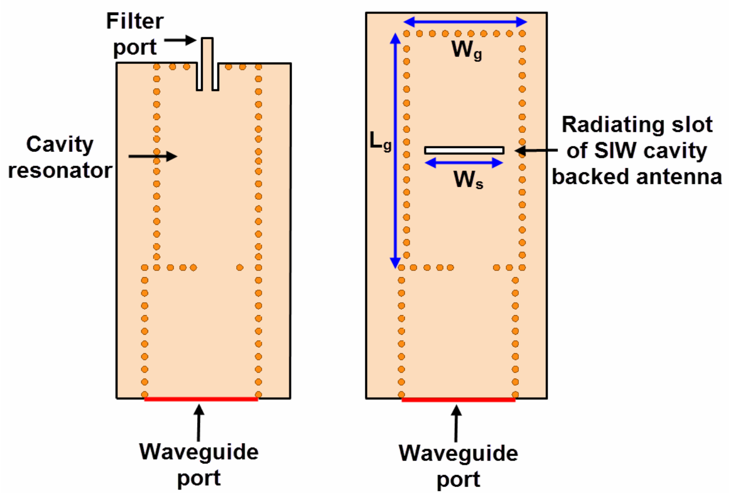

(a) (b)

Figure 3.7 Schematics of simulation models used for evaluating the reflection coefficients of a waveguide port used to excite (a) cavity resonator with a filter port and (b) SIW cavity backed slot antenna.

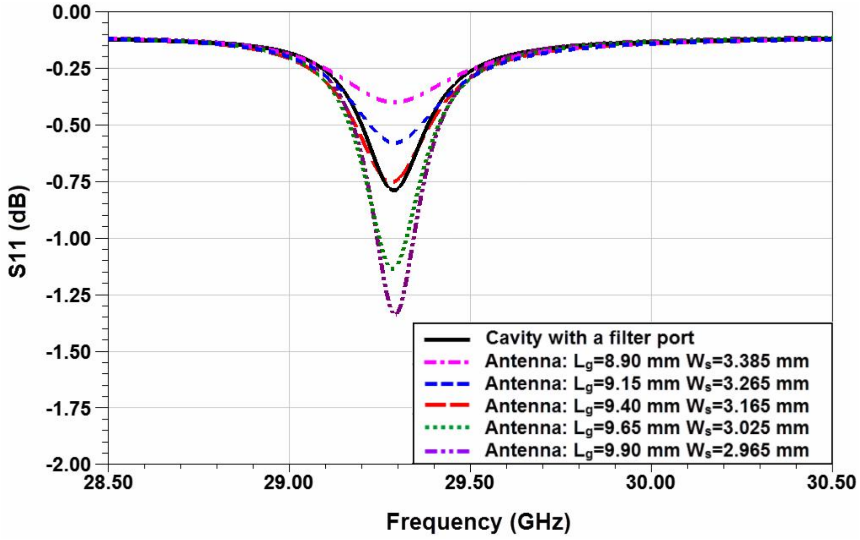

Figure 3.8 Reflection coefficients of the waveguide port 1 for the end resonator of either a cavity resonator or a cavity-backed slot antenna.

the one of the antenna unit case.

Figure 3.8 plots different simulated $|S_{11}|$ results of the above two cases, in which the results for the filter case is presented in solid line and those for the antennas are plotted in dashed/dotted lines. It should be pointed out that, the combinations *of* W_s

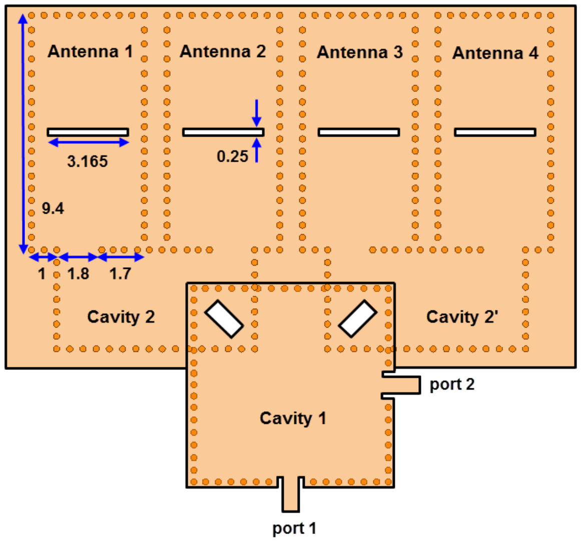

Unit: mm

Figure 3.9 Geometrical parameters of the proposed filtering monopulse antenna array.

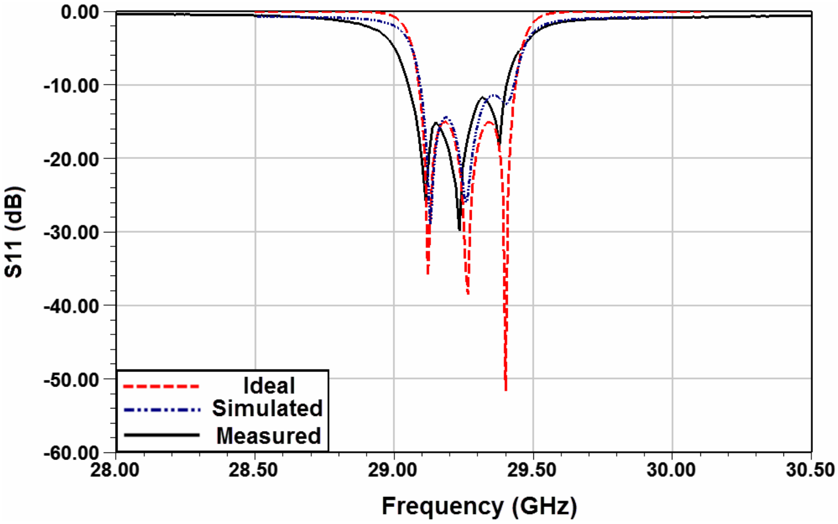

Figure 3.10 Simulated and measured reflection coefficients of the filtering monopulse antenna array for the sum channel, as well as ideal frequency responses of the four-output filter.

and L_g are all tuned to enable the filtering antenna case to resonate at the same frequency as the one in the filter case. The combination of L_g=9.40 mm and W_s=3.165 mm will obtain the best match for the proposed design. By using cavity-backed slot antennas with the optimized parameters above to replace those four cavities coupled with the four outputs in the filter shown in Figure 3.3, an SIW filtering antenna array

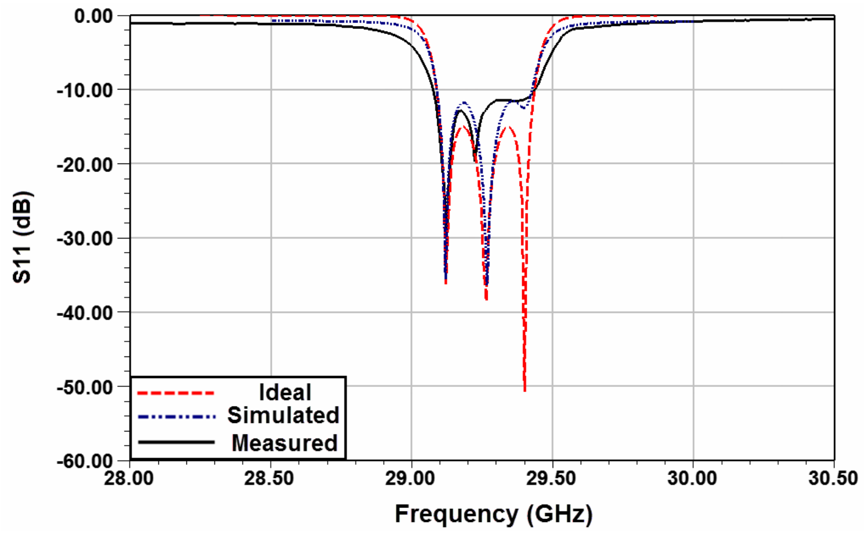

Figure 3.11 Simulated and measured reflection coefficients of the filtering monopulse antenna array for the difference channel, as well as ideal frequency responses of the four-output filter.

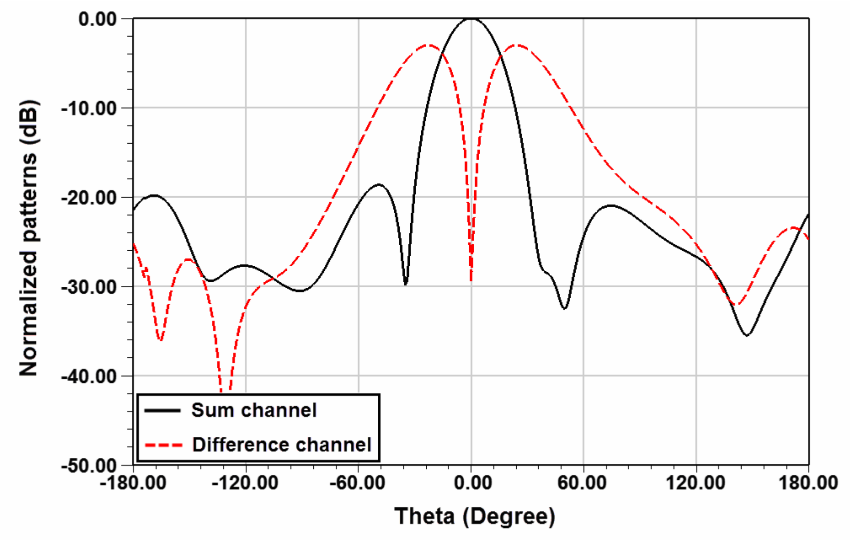

Figure 3.12 Simulated radiation patterns of the filtering antenna at 29.25 GHz.

with monopulse functions can be established as shown in Figure 3.1. Figure 3.9 illustrates the finalized parameters of the filtering antenna.

Figure 3.10 and Figure 3.11 plot simulated frequency responses of the proposed antenna array for sum and difference channels, respectively. A good correspondence

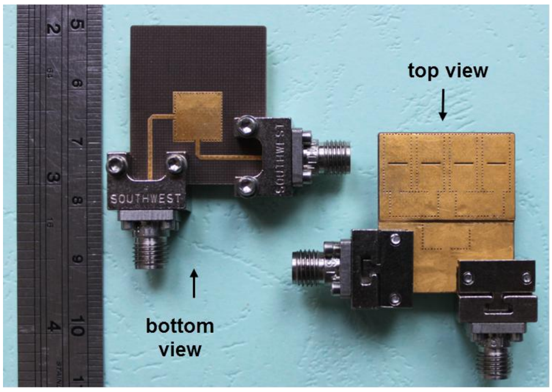

Figure 3.13 Top and bottom views of the fabricated filtering monopulse antenna array.

can be observed between simulated results and those obtained from the ideal circuit. Figure 3.12 plots simulated far-field radiation patterns. A maximum gain of 8.5 dBi can be obtained in the sum beam, while a null depth better than 29 dB can be obtained for the difference beam.

3.2.3 Measurement Results and Discussions

The photograph of a fabricated prototype is given in Figure 3.13. A 2.92 mm southwest super SMA connector and an Agilent E8363C vector network analyzer are used for the measurement of its impedance characteristics. Measured results of the reflection coefficients are also given in Figure 3.10 and Figure 3.11. In the measurement of the difference channel, the center frequency is close to the simulated value, while it does not exactly match the simulated one for the sum channel. The implementation of the super SMA connector and those fabrication tolerances might result in the discrepancy between simulation and measurement. An anechoic chamber is used for the far-field measurement. For the sum channel, a maximum gain of about

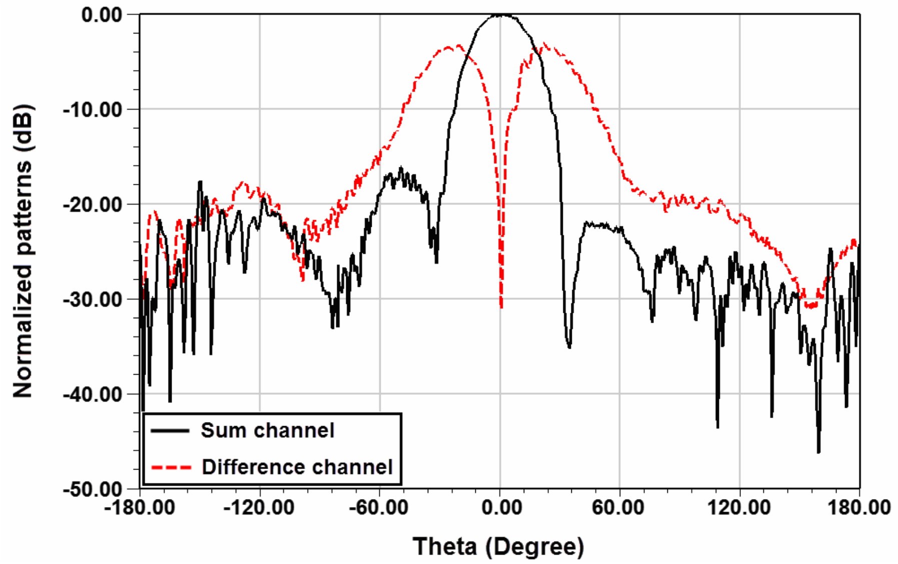

Figure 3.14 Measured radiation patterns of the filtering antenna at 29.25 GHz.

8.1 dBi is obtained at the broadside of this antenna array in the measurement. Using the method by comparing the measured gain and simulated directivity, the overall efficiency of the proposed filtering antenna array is found to be 54.4%, which is equivalent to a 2.65-dB loss. This loss is mainly resulted by the finite *Q*-factor of the utilized SIW cavity resonators. Radiation patterns are measured at 29.25 GHz and illustrated in Figure 3.14. A beamwidth of about 30.5° is achieved in the measurement for the sum channel. A null depth around 27 dB is obtained in the difference channel. A good correspondence can be observed between measurement and simulation.

3.3 A Filtering Dual-Polarized Antenna Subarray Targeting for Base Stations in Millimeter-Wave 5G Wireless Communications

In order to meet the increasing demand for higher data rate, the fifth generation (5G) mobile and wireless communication technologies are becoming a hot research topic. For spectrum bandwidth below 10 GHz, it becomes almost crammed. Therefore, a higher frequency spectrum, e.g. the millimeter-wave (mm-Wave) band has gained significant interest [84-86]. There are mainly two challenges when applying these underutilized spectra for future outdoor cellular applications. One is the geographical coverage range, another is the connection in non-line-of-sight (NLoS) environments [87]. The above two challenges can be resolved by using a large number of antenna elements to achieve directional beams together with large gain values, since the wave-lengths of mm-Wave frequencies are relative small. In order to achieve proper beam pointing to a desired direction, the digital beamforming (DBF) scheme is one efficient approach [88].

Theoretically, implementing the same number of transceivers as the antenna number can provide the optimal performance for a base station. However, this may not be feasible due to high complexity and cost, especially when the antenna number is very large. A more practical and cost-effective design is to deploy much smaller

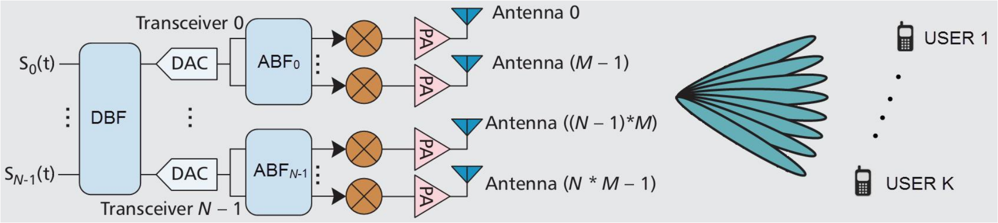

Figure 3.15 A hybrid beamforming structure (digital beamforming and analog beamforming) for 5G mmWave base station applications. [89]

number of digital transceivers than total antenna number. It can be achieved via an analog beamforming scheme [89], in which each transceiver is connected with multiple active antennas. A network of analog phase shifters is used to individually control the signal phase on each antenna. Figure 3.15 shows the architecture of the beamforming structure described above. This architecture also has been successfully implemented in [87] and demonstrated in system level. Another approach to reduce the transceiver numbers is the subarray technology [89]. As presented in [89], only 4 RF units were required in per channel, which is much less than the original system requiring 32 RF units.

In typical antenna designs for base stations, dual-polarized antennas [90] are preferred, so as to provide the polarization diversity and increase the channel capacity [91]. If the dual-polarized concept can be integrated with the filtering antenna concept, an improved efficiency to the whole functional block is able to be achieved, which is very attractive for system designs.

This section presents a filtering dual-polarized antenna subarray including 4 elements in the form of 2×2. This proposed filtering antenna subarray targets at the application of base stations in mm-Wave 5G wireless communications, and will work as a building block for a beamforming system operating at *Ka*-band. A dual-path 1×4 feeding network and four slot antennas backed by cavities are included in a multilayered 3-D structure, by implementing the low temperature co-fired ceramic (LTCC) technology. The two operating modes in each cavity for different paths are always orthogonal to each other, in order to achieve a low cross-polarization in its radiation. Meanwhile, for the purpose of obtaining a good isolation between the two inputs, a novel method by modifying the arrangement of some vias in the cavity of the first stage is proposed. The fabricated prototype is centered at 37 GHz with a bandwidth of 600 MHz. Its performance has also been verified in the measurement.

3.3.1 Design of A Dual-Path Filter

A key issue for 5G wireless communications is to find out enough available bandwidth. Nowadays, most research is focused on the 28 GHz band, the 38 GHz band, the 60 GHz band, and the E-band (71-76 GHz and 81-86 GHz) [92]. Among the above frequency spectrums, it is found that the 28 GHz (25.25-29.5 GHz) and 38 GHz (36.25-40.5 GHz) bands suffer less rain attenuation and oxygen absorption than others. This feature is very important to improve the communication range for mm-

Wave wireless systems [93]. Therefore, in this design, the center frequency and bandwidth are determined to be 37 GHz and 500 MHz, which are similar as the one in [87], to meet data rates required by next generation communications.

In order to successfully realize a desired dual-polarized antenna subarray with filtering characteristics, a reference filter with two isolated transmission paths needs to be designed first. This reference filter is of 4th-order, in which one input and four outputs in each path are included. Each output corresponds to one radiating element in the final filtering antenna. Good isolation is required between the two paths, in order to minimize the cross-polarization level after the last-stage resonators are replaced by suitable antennas in the synthesis of the filter and antenna. An LTCC material Ferro-A6 with a dielectric constant ε_r of 5.9 and loss tangent of 0.002 is used in this design, with 20 substrate layers. The thickness for each layer is 0.1 mm. To achieve the frequency selection and EM-wave radiation with low radiation loss, SIW cavity resonators are implemented. The diameter of the metallic via d and distance between adjacent vias s, are 0.2 mm and 0.5 mm, respectively.

Three major considerations need to be taken into account in the design of the proposed dual-path filter.

1) Cavities and Arrangement: Square SIW cavities operating at two orthogonal modes, which are diagonal TE_{102} mode (mode 1) and TE_{201} mode (mode 2), are used

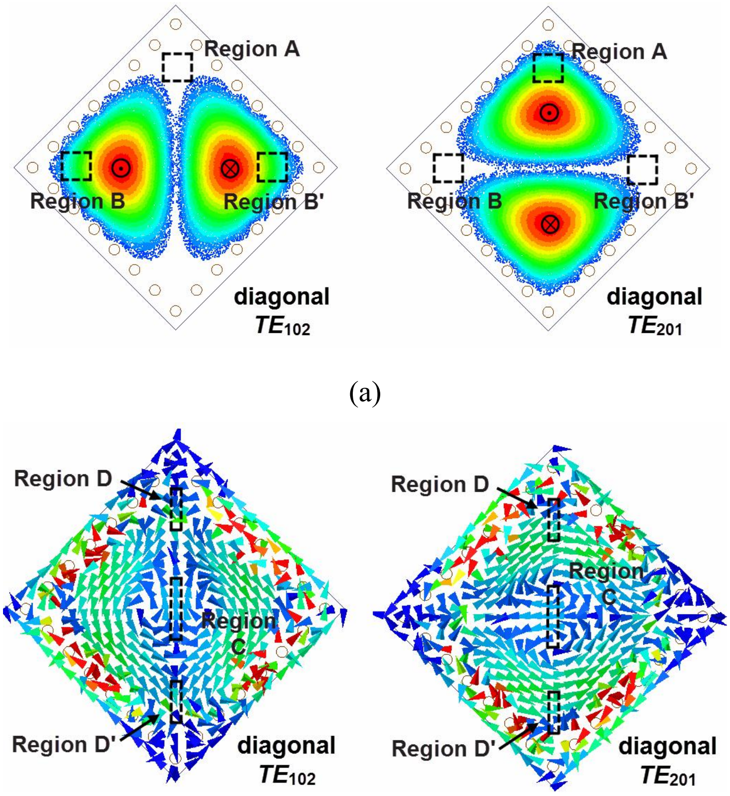

(a)

(b)

Figure 3.16 (a) The electric field and (b) magnetic field distributions of two degenerated modes (diagonal TE_{102} and TE_{201}) in a square SIW cavity.

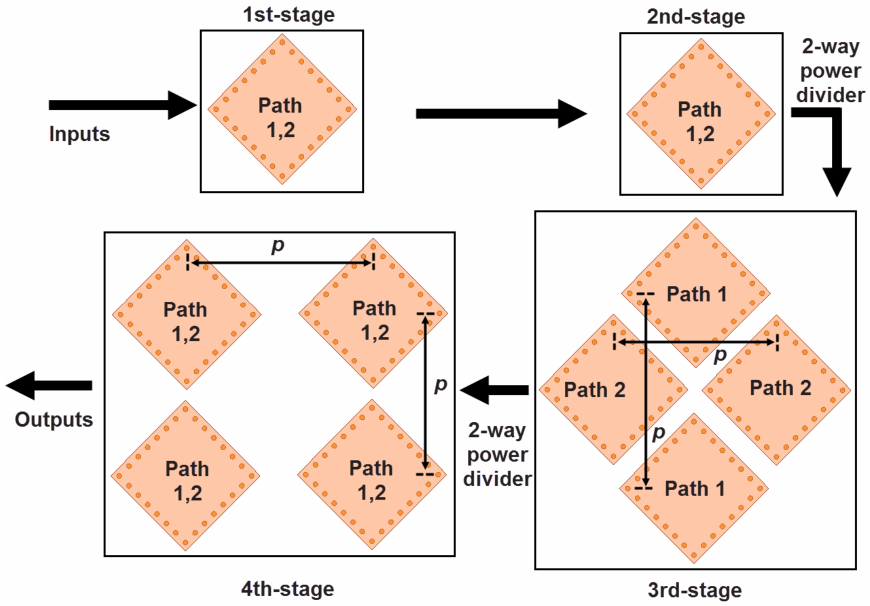

Figure 3.17 Stage-by-stage cavity arrangement in the dual-path filter.

as resonators in this filter. Figure 3.16 plots the electric and magnetic field distributions of the two operating modes, using HFSS simulation software. It can be estimated that, if the operating mode in each path of this filter is the same, to be either mode 1 or mode 2, good isolation can be achieved between these two paths.

It is also very important to properly arrange those resonant cavities in this reference filter. Power-division and isolation between the two paths need to be realized within the same structure. Figure 3.17 illustrates the proposed stage-by-stage cavity arrangement in our design. It is seen that, cavities of the 1st-, 2nd- and 4th-stages are dual-mode ones and operate in both paths. Cavities of the 3rd-stage are single-mode ones and operate in only one path. Furthermore, the cavity of the 2nd-stage also works as a power divider for both paths, while the ones of the 3rd-stage only work in one path to achieve the power-division functions. In the ideal case, when input port related to path 1 is excited, those cavities corresponding to this path are expected to resonate only at mode 1. This is also desired when input port related to path 2 is excited. Detailed realization methods will be discussed in following sections. The distance *p* between those adjacent cavities in the 4th-stage should be restricted to be less than one wavelength. This is to ensure no grating lobe will be generated after replacing those cavities in the 4th-stage by radiating elements.

2) External Coupling: Choice of locations for external input/output ports is primarily based on one consideration, which is that one input/output port should relate to only one resonant mode (either mode 1 or mode 2) in the cavities of the 1st- or 4th-stage. Therefore, regions A and B in Figure 3.16(a) are selected to locate external ports. It can be observed that, the electric field in region A is strong for the diagonal TE_{201} mode but weak for the diagonal TE_{102} mode, while region B is strong for the diagonal TE_{102} mode but weak for the diagonal TE_{201} mode. When a port is located at region A, it causes a strong coupling at the diagonal TE_{201} mode and almost null coupling at the diagonal TE_{102} mode. On the contrary, when a port is located at region B, only diagonal TE_{102} mode will be excited.

Good isolation between the two input ports is also very important in a dual-polarized antenna design. The electric field distributions excited by port 2 in the cavity of the 1st-stage are illustrated in Figure 3.18(a). It can be observed that, the electric field inside this cavity is not the same as the ideal case, whose electric field should be symmetrical with respect to its symmetrical plane [dashed line], but rotated by a certain angle represented by the dot-dot-dashed line due to the perturbation of the two ports. Therefore, a weak coupling will be resulted between port 2 and port 1, leading to a degraded isolation performance. This is also verified by simulated results plotted in Figure 3.19. It is seen that, the isolation between port 2 and port 1 is only

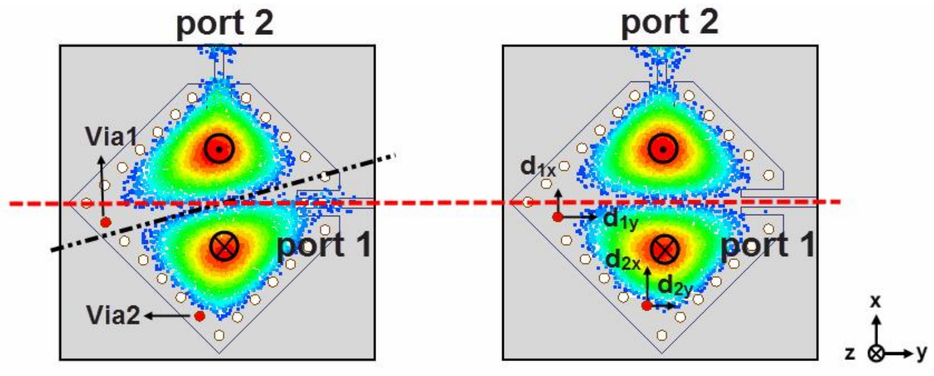

(a) (b)

Figure 3.18 Field distributions of the 1st-stage cavity (a) before geometry modification and (b) after geometry modification.

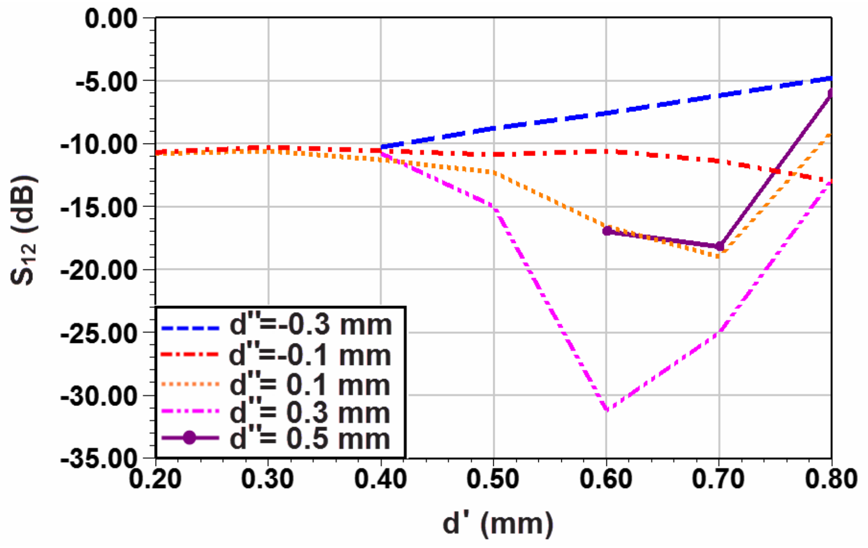

Figure 3.19 Simulated $|S_{12}|$ versus d' with different d'' as a parameter.

around -11 dB, when the cavity shown in Figure 3.18(a) resonates at 37 GHz.

In order to solve this problem, the geometry of this cavity is modified by changing positions of several vias as shown in Figure 3.18(b). The location of two vias [via 1 and via 2 marked in red in Figure 3.18(a)] are both symmetrically shifted, which means $d_{1y}=d_{2x}=d'$ and $d_{1x}=d_{2y}=d''$. Simulated $|S_{12}|$ results are plotted in Figure 3.19 at the resonant frequency versus d' with different d'' as a parameter. It is found that, in the case when d'=0.6mm and d''=0.3 mm, the isolation can be as high as 31 dB, which is much better than the value obtained without any geometry modification. The electric field distributions inside the cavity become symmetrical again as shown in Figure 3.18(b), which also well verifies the improved performance.

3) Internal Coupling: Structures for the realization of internal couplings are also essential for this dual-path filter design. The design principle is that, when adjacent cavities at different stages resonate under the same mode [marked as "case 1"], proper couplings can be generated. On the contrary, when they resonate under orthogonal modes [marked as "case 2"], no coupling can be generated. Meanwhile, power division should be achieved between resonators of the 2nd- and 3rd-stages, as well as between resonators of the 3rd- and 4th-stages. Moreover, interference between adjacent coupling structures should be avoided. This kind of interference can be minimized by locating those coupling structures at different cavity regions. In order to achieve the above aims, three different coupling structures are employed.

A rectangular slot with a small width, located at the center of the square cavity [e.g. region C in Figure 3.16(b)], is used as the coupling structure between cavities of the 1st- and the 2nd-stage. The electric field is relative weak around region C, while it is strong for magnetic field. Therefore, magnetic couplings can be generated around this

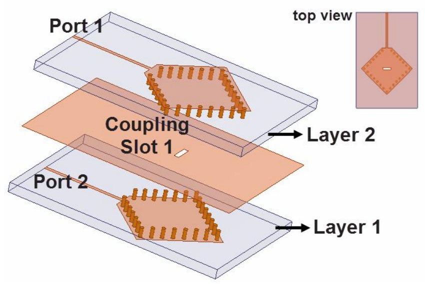

(a)

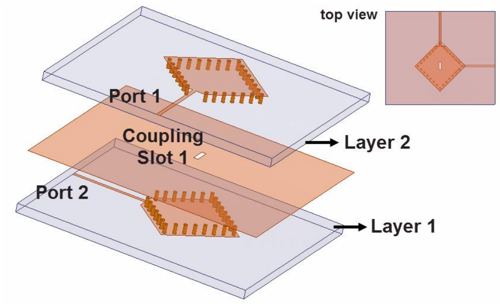

(b)

Figure 3.20 Models for the coupling simulation between cavities of the 1st- and 2nd-stage. (a) Cavities resonating under the same mode (case 1). (b) Cavities resonating under orthogonal modes (case 2).

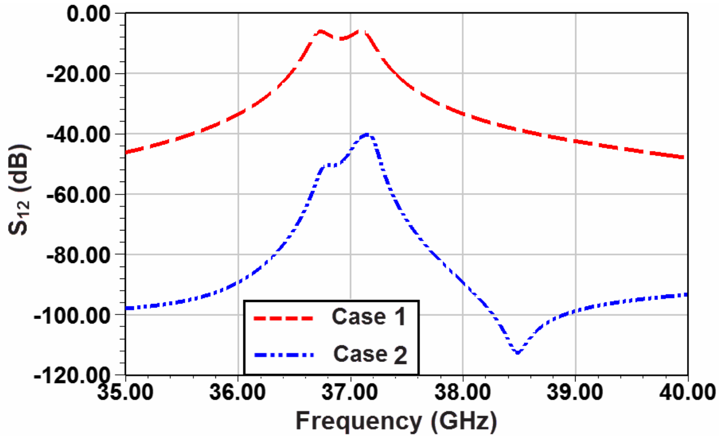

Figure 3.21 Couplings between adjacent cavities of the 1st- and 2nd-stage in different situations.

slot only when the two vertically stacked cavities operate at the same mode. Models shown in Figure 3.20 are used to evaluate the coupling strength under the two cases mentioned above. Results are plotted in Figure 3.21, in which the coupling strength

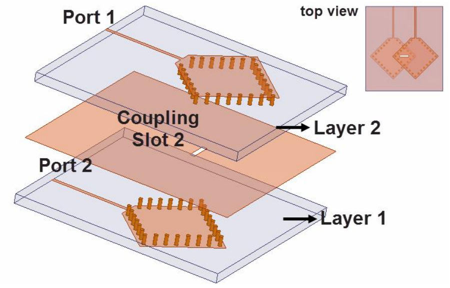

(a)

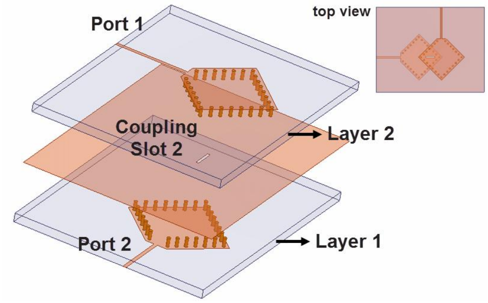

(b)

Figure 3.22 Models for coupling simulation between cavities of the 2nd- and 3rd-stage. (a) Cavities resonating under the same mode (case 1). (b) Cavities resonating under orthogonal modes (case 2).

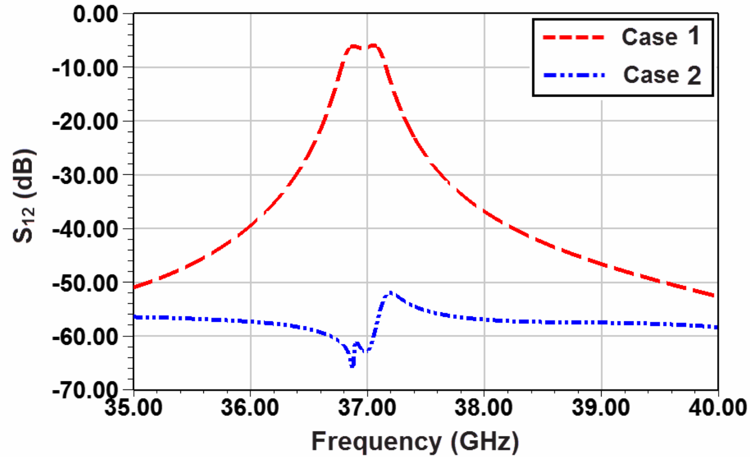

Figure 3.23 Couplings between adjacent cavities of the 2nd- and 3rd-stage in different situations.

for case 1 is about 35 dB higher than the one for case 2.

Couplings between cavities of the 2nd- and 3rd-stage are also of magnetic kind, by using rectangular slots symmetrically located at regions D and D' [shown in Figure 3.16(b)]. The working mechanism is the same as that of coupling slots in region C.

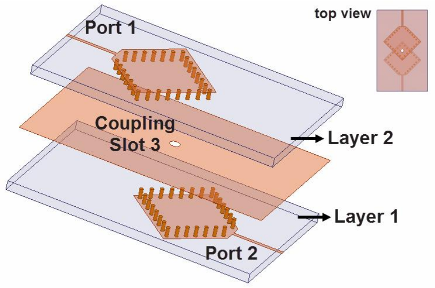

(a)

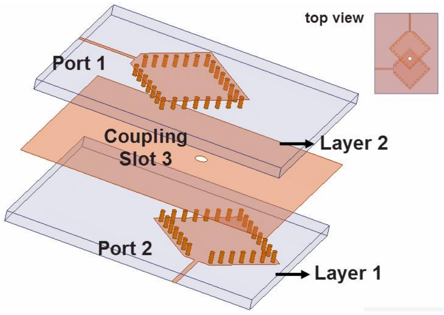

(b)

Figure 3.24 Models for coupling simulation between cavities of the 3rd- and 4th-stage. (a) Cavities resonating under the same mode (case 1). (b) Cavities resonating under orthogonal modes (case 2).

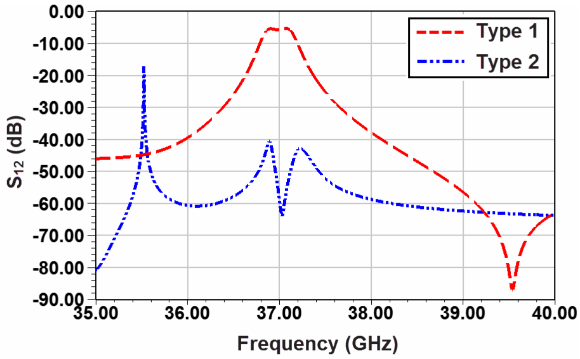

Figure 3.25 Couplings between adjacent cavities of the 3rd- and 4th-stage in different situations.

Figure 3.22(a) and (b) shows simulation models for the validation, respectively. Results plotted in Figure 3.23 indicate a 45 dB lower attenuation for case 2 when compared with the one for case 1.

The coupling between cavities of the 3rd- and the 4th-stages are realized by circle slots located at regions B and B' [as plotted in Figure 3.16(a)]. This structure can achieve a mixed electric and magnetic coupling for the diagonal TE_{102} mode, and almost no coupling for the diagonal TE_{201} mode. It is found that, within two cavities coupled by this coupling structure, the magnetic fields of the low mode near the coupling section are of the same direction [either both clockwise or both anti-clockwise], while they are of different directions [e.g. one is clockwise another is anti-clockwise] for the high mode. The above phenomenon indicates that the electric coupling is the dominant one within this coupling structure [94]. Regions B and B' are located symmetrically with respect to the center of a cavity, in order to obtain an equal power division. A 35 dB higher coupling strength than that for case 2 is achieved for case 1 as plotted in Figure 3.25.

By vertically cascading cavities shown in Figure 3.17 using coupling structures described above, a 4th-order Chebyshev reference filter shown in Figure 3.26(a) is designed. Cavities of each stage include 5 layers of LTCC substrate [seen in Figure 3.26(b)]. Inputs & outputs are achieved by using microstrip lines with coupling slots. The coupling strength can be controlled by varying the length of the coupling slots. In this filter, input port P1 and output ports P3-P6 correspond to path 1, while input port P2 and output ports P7- P10 correspond to path 2. This filter is also symmetrical with respect to the center of cavity 1. Figure 3.27(b) illustrates the coupling scheme for the

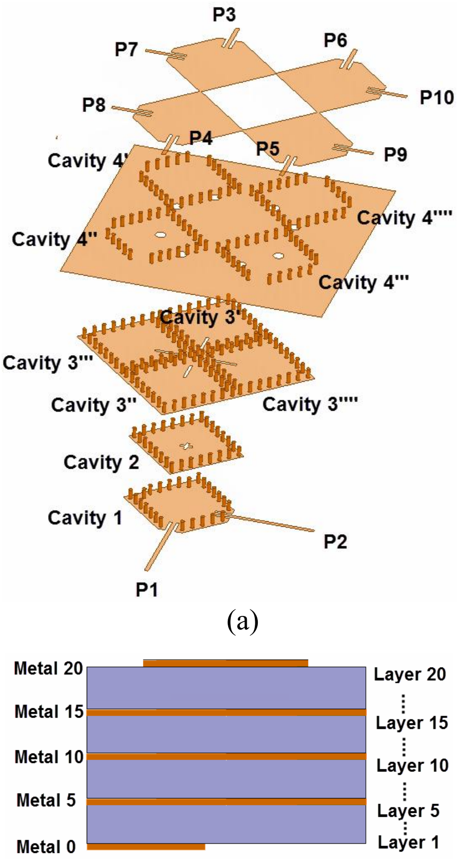

(a)

(b)

Figure 3.26 (a) Cross-section view of the proposed dual-path filter and (b) its layer definition.

proposed dual-path filter with eight outputs, which is extracted from a conventional 4th-order filter with one output as shown in Figure 3.27(a). Since node 2 and nodes 3'&3" act as two-way dividers, we can have

$$M_{23'} = M_{23''} = M_{23} / \sqrt{2} \tag{3.5}$$

$$M_{3'4'} = M_{3'4''} = M_{3''4'''} = M_{3''4''''} = M_{34} / \sqrt{2} \tag{3.6}$$

so that the total transmitted power can be kept unchanged. The coupling coefficients for the output are identical to those in Figure 3.27 (a):

$$M_{4'L'} = M_{4''L''} = M_{4'''L'''} = M_{4''''L''''} = M_{4L} \tag{3.7}$$

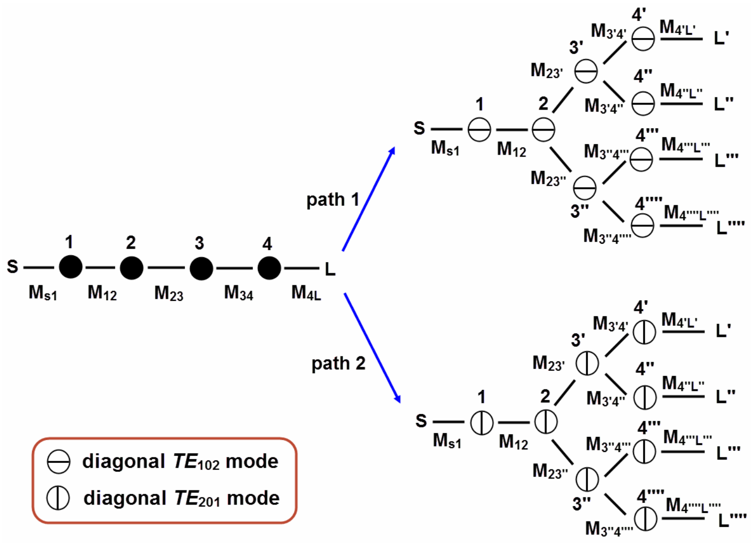

(a) (b)

Figure 3.27 Coupling schemes of a (a) 4th-order bandpass filter and (b) 4th-order dual-path filter (path 1 and path 2) extended from the previous filter.

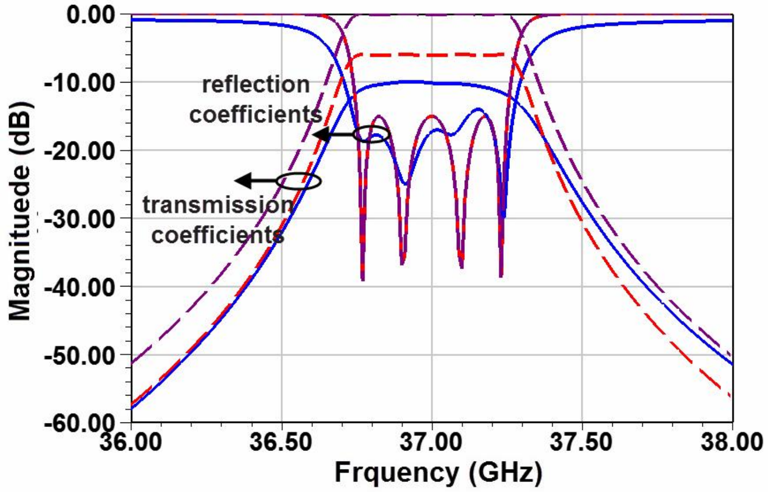

Figure 3.28 Synthesized frequency responses of one path in the dual-path filter with four outputs and its one output counterpart. (dashed line: synthesized responses, solid line: full-wave simulation responses)

Synthesized responses of one path in this dual-path filter, with in-band return loss of 15 dB, are plotted in Figure 3.28. Coupling coefficients for this filter are below: M_{S1}=0.9146, M_{12}=0.8021, M_{23}=0.6426, M_{34}=0.8021, M_{4L}= 0.9146. The filter is

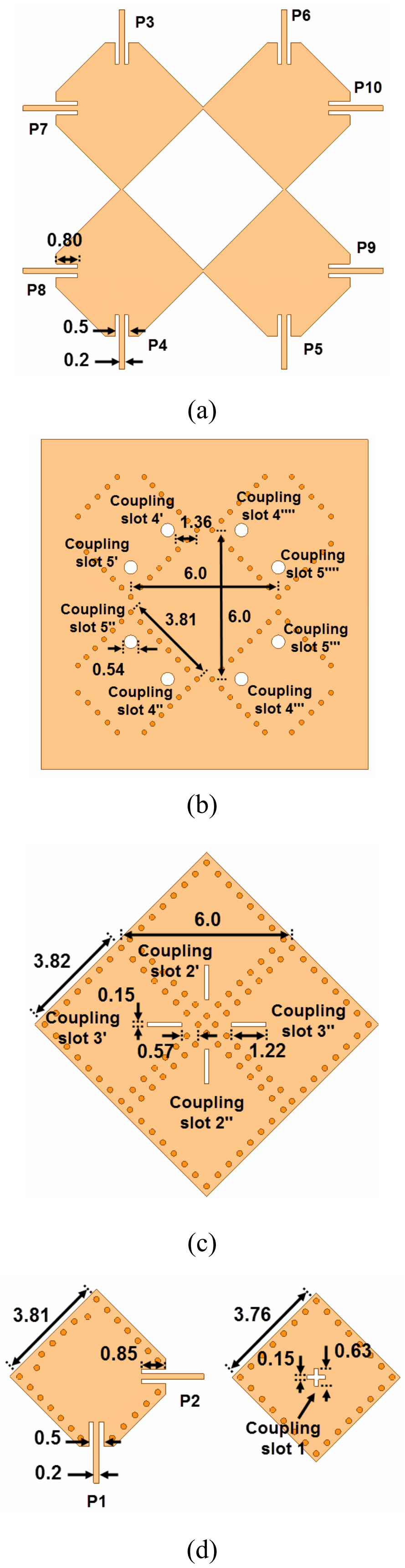

Figure 3.29 Dimensions of the proposed dual-path filter in different stages. (a) The 4th-stage. (b) The 3rd-stage. (c) The 2nd-stage. (d) The 1st-stage. (Unit:mm)

centered at f_0=37.0 GHz with a bandwidth of BW=600 MHz. Only one curve for the transmission coefficients is included, due to frequency responses of the four outputs are identical to each other. It is seen that, the reflection coefficients of the four-output bandpass filter coincide with those in the one-output filter, while the transmission coefficients are all 6 dB lower than those in its counterpart.

Coupling coefficients are de-normalized to obtain initial design parameters for the physical realization of the proposed four-output filter [75]. A fine tuning procedure is conducted to achieve the desired frequency responses using the HFSS simulator. Figure 3.29 (a)-(d) list detailed dimensions of the reference filter, in which p is finalized to be 6 mm ($\approx 0.75\lambda_0$). Full-wave simulated frequency responses are compared with ideal results in Figure 3.28. As can be seen, the transmission coefficients within the passband are about 4 dB lower than synthesized ones, which is mainly caused by the finite quality factors ($Q_u \approx 400$) of the SIW cavity.

3.3.2 Design of Dual-Polarized Filtering Antenna Subarray

1) Selection of Radiator: In the filter-antenna synthesis, planar cavity-backed slot antennas are selected as radiators. Those radiators also perform as equivalent loads to the filter within its passband. Figure 3.30 lists 4 possible candidates for the radiator [marked by radiator 1 to 4], in which two of them operate in diagonal TE_{201}&TE_{102} modes [Figure 3.30(a)&(b)], while the other two in conventional TE_{201}&TE_{102} modes

[Figure 3.30(c)&(d)]. Electric field distributions for two orthogonal operation modes are also plotted. Radiating slots are indicated by dashed lines. Coupling slots between radiators and its preceding cavities are illustrated by circles. All these radiators are capable to generate two orthogonal linear polarizations. Two radiating slots are included in radiator 2 [shown in Figure 3.30(b)] and radiator 4 [shown in Figure 3.30(d)]. These two kinds of radiators are actually extended from their single slot prototypes proposed in [73]. Four radiating slots are included in radiator 2, which is extended from its two-slot prototype proposed in [74]. In all the above 3 kinds of radiators, only one/one pair of the slots will work when one operation mode is excited, to achieve a radiation with linear polarization. However, the situation is quite different for radiator 1. By observing the field distributions, it is noticed that, all the four slots will work for either operation mode in radiator 1. Linearly polarized waves are achieved by the sum of their radiation.

Dimensions of these 4 kinds of radiators are also given in Figure 3.30. It can be observed that, radiators 1 and 2 are relative larger ones, whose sizes are close to one wavelength in free space. For radiator 3, those coupling slots overlap the radiating slots in the vertical direction and might bring in some interference. Among these radiators, radiator 4 is the smallest one, which gives the designer more flexibility in the final integration of the filter and radiators. To this end, radiator 4 is selected as

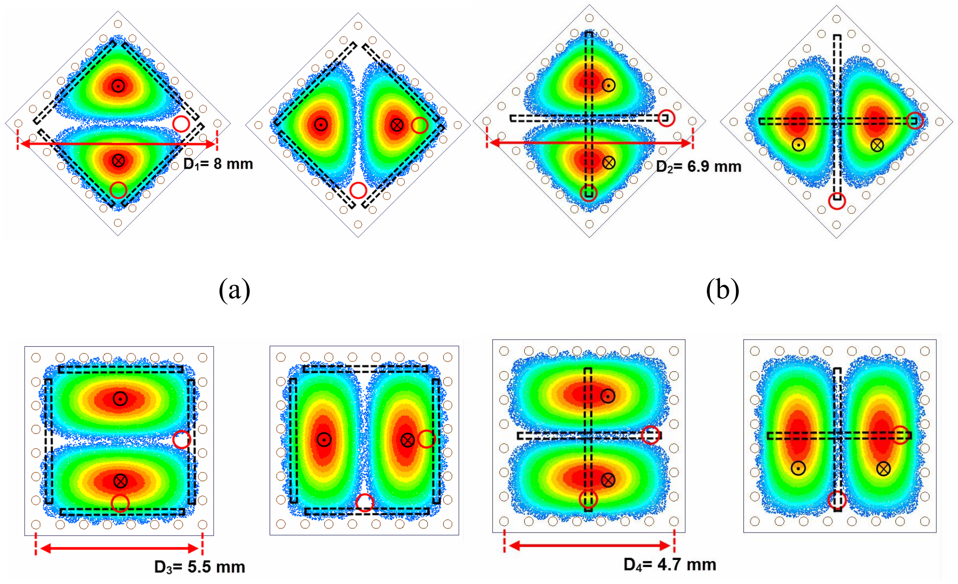

(a) (b)

(c) (d)

Figure 3.30 Geometries and electric field distributions for (a) radiator 1 [quad-slot operating in diagonal $TE_{201}\&TE_{102}$ modes], (b) radiator 2 [dual-slot operating in diagonal $TE_{201}\&TE_{102}$ modes], (c) radiator 3 [quad-slot operating in $TE_{201}\&TE_{102}$ modes] and (d) radiator 4 [dual-slot operating in $TE_{201}\&TE_{102}$ modes].

the radiator in the proposed filtering antenna subarray.

2) Antenna Subarray Synthesis: In order to successfully replace those last-stage resonators in the filter by radiators, the coupling between a radiator and a cavity resonator of the 3rd-stage [one of nodes 3' to 3""] need to be identical to the one between an end resonator [one of nodes 4' to 4""] and a 3rd-stage one, and the same external quality factor can be acquired for an end resonator of the filter and a radiator. The above two considerations can be evaluated simultaneously, by using the method introduced in [28] and two evaluation structures shown in Figure 3.31(a) and (b). The waveguide port is assumed to be port 1 in this evaluation.

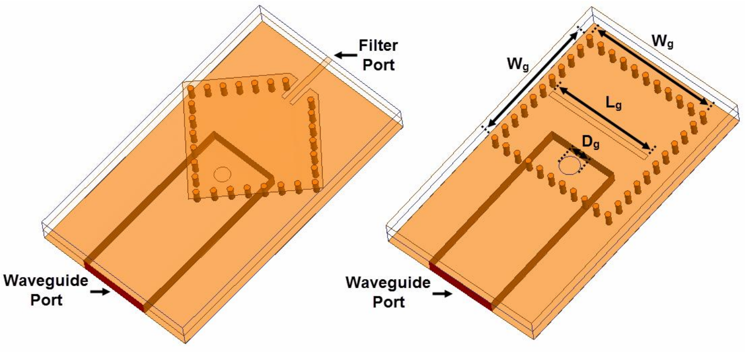

(a) (b)

Figure 3.31. Schematics of simulation models used for evaluating the reflection coefficients of a waveguide port used to excite (a) a cavity resonator with a filter port and (b) an SIW cavity backed slot antenna.

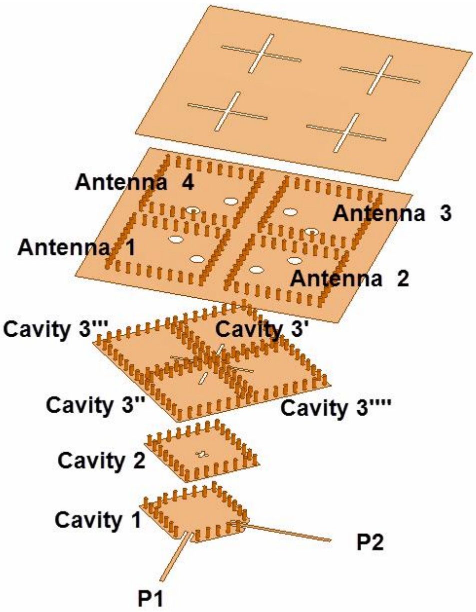

Figure 3.32 Cross-section view of the proposed filtering dual-polarized antenna sub-array.

A parametric study versus different combinations of W_g, L_g and D_g is conducted to match $|S_{11}|$ results obtained from the two structures in Figure 3.31. In our case, the best match is found when W_g=4.74 mm, L_g=4 mm and D_g=0.69 mm. After parameters of the radiators and their internal coupling slots are finalized, SIW resonators of the 4th-stage will be replaced by radiators in the filter-antenna synthesis. Figure 3.32

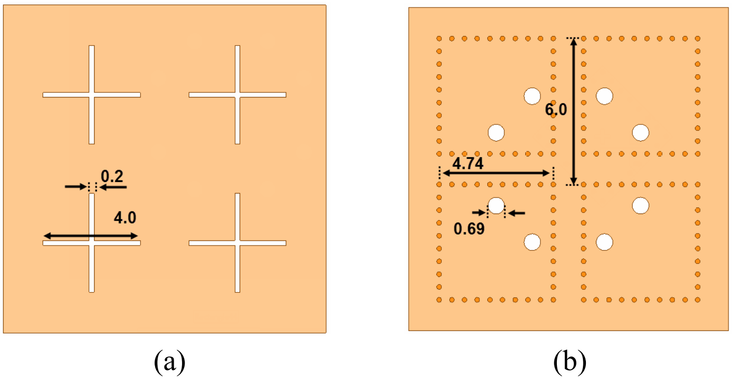

(a) (b)

Figure 3.33 Geometrical parameters of the radiation part for the proposed filtering monopulse antenna array.

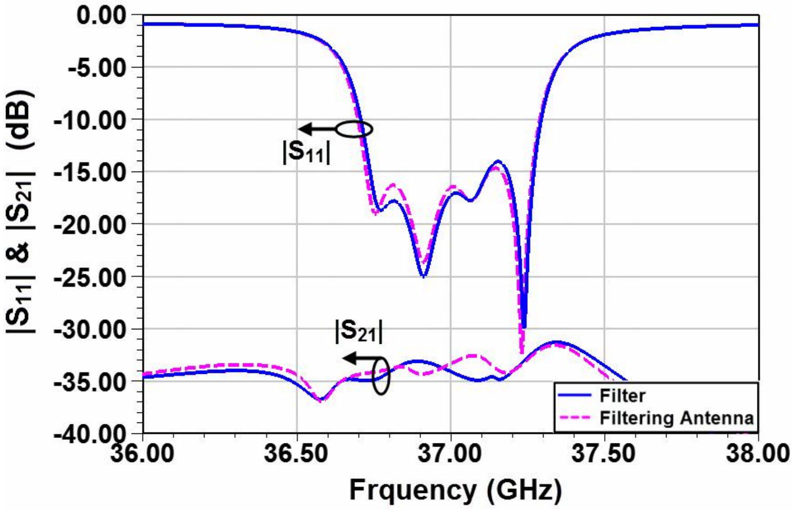

Figure 3.34 Simulated $|S_{11}|$&$|S_{21}|$ results of the filter (proposed in Section 3.3.1) and the filtering antenna (proposed in Section 3.3.2).

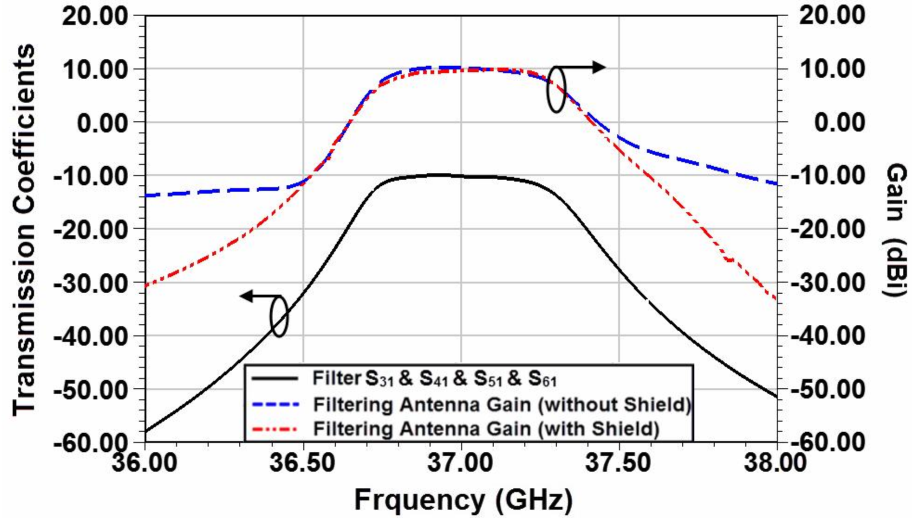

Figure 3.35 Simulated $|S_{21}|$ results of the filter and gain of the filtering antenna.

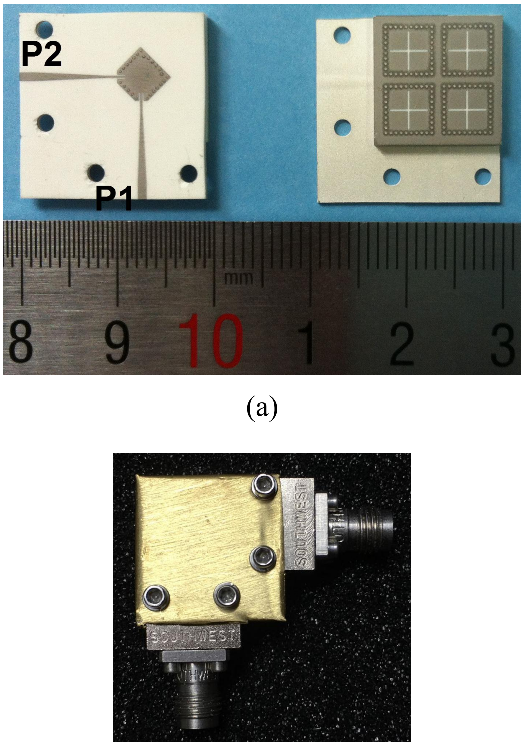

(a)

(b)

Figure 3.36 (a) Top view and bottom view of the fabricated filtering antenna and (b) fabricated antenna with a metallic shield.

shows the established filtering antenna subarray with dual-polarized radiations. Its dimensions are illustrated in Figure 3.33. Figure 3.34 plots simulated reflection coefficients for the two input ports of the proposed filtering dual-polarized antenna subarray. Simulated center frequency and bandwidth both coincide with its dual-path reference filter. Within the passband, $|S_{11}|$ and $|S_{12}|$ are smaller than -14.5 dB and -30 dB, respectively. Figure 3.35 plots simulated gain versus frequency. It can be observed that, the gain results do not roll off as sharply as the $|S_{21}|$ results of the filter. Radiation leakage from microstrip input lines are possible reasons. Therefore, a metallic cavity is designed to shield those microstrip lines as shown in Figure 3.36(b), and enable the roll off of the filtering antenna to coincide with the filter.

3.3.3 Measurement and Discussions

The above design has been fabricated and measured for validation purpose. The photograph of the fabricated prototype is shown in Figure 3.36. 2.92mm southwest super SMA connectors are used for the measurement. Measured and simulated $|S_{11}|$ results are compared in Figure 3.37. In the measurement, the working frequency range for $|S_{11}|$<-10 dB is from 36.8 GHz to 37.33 GHz, which is slightly smaller than the one in simulation. This can be attributed to the super SMA connector, the ± 0.8% tolerance of the shrinkage rate of the material, possible deviation of the dielectric loss of LTCC and the fabrication tolerance. Isolation better than 32 dB, which can meet the typical requirement for base station applications, is achieved in the measurement.

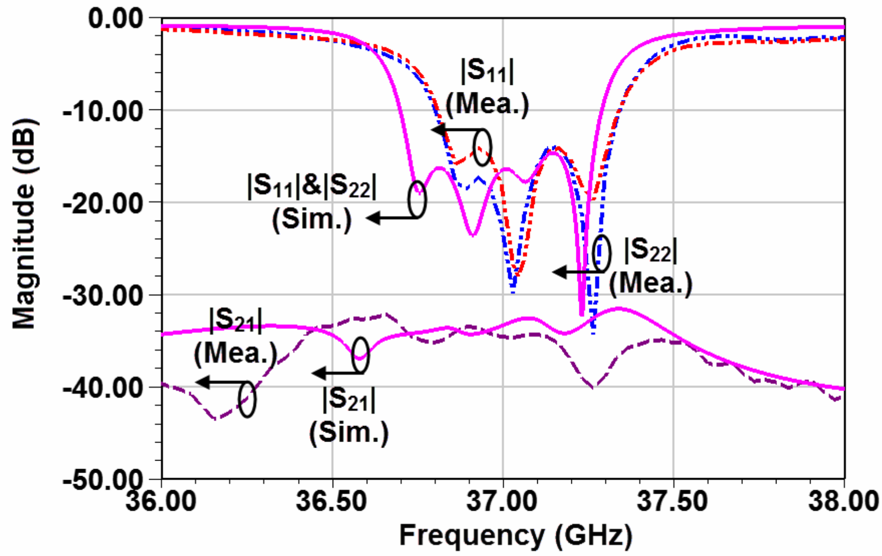

Figure 3.37 Simulated and measured reflection coefficients and isolation of the proposed filtering antenna.

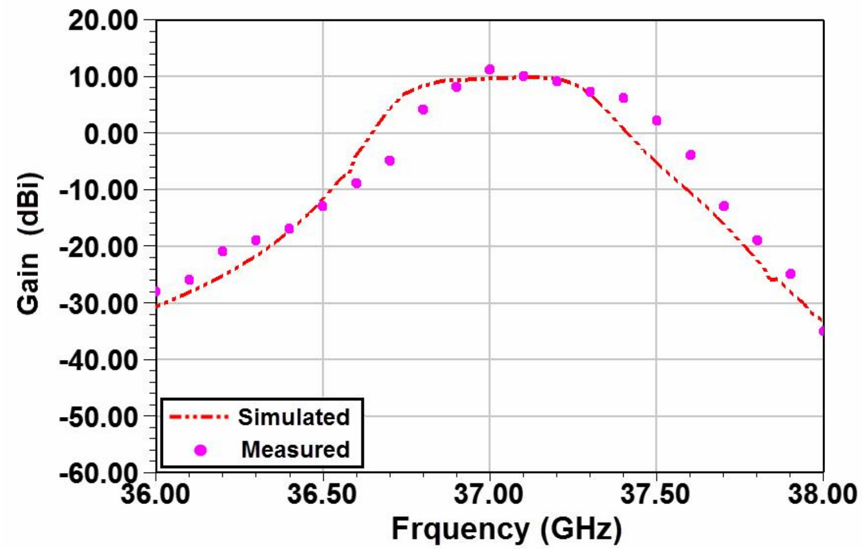

Figure 3.38 Simulated and measured gain of the proposed filtering antenna subarray.

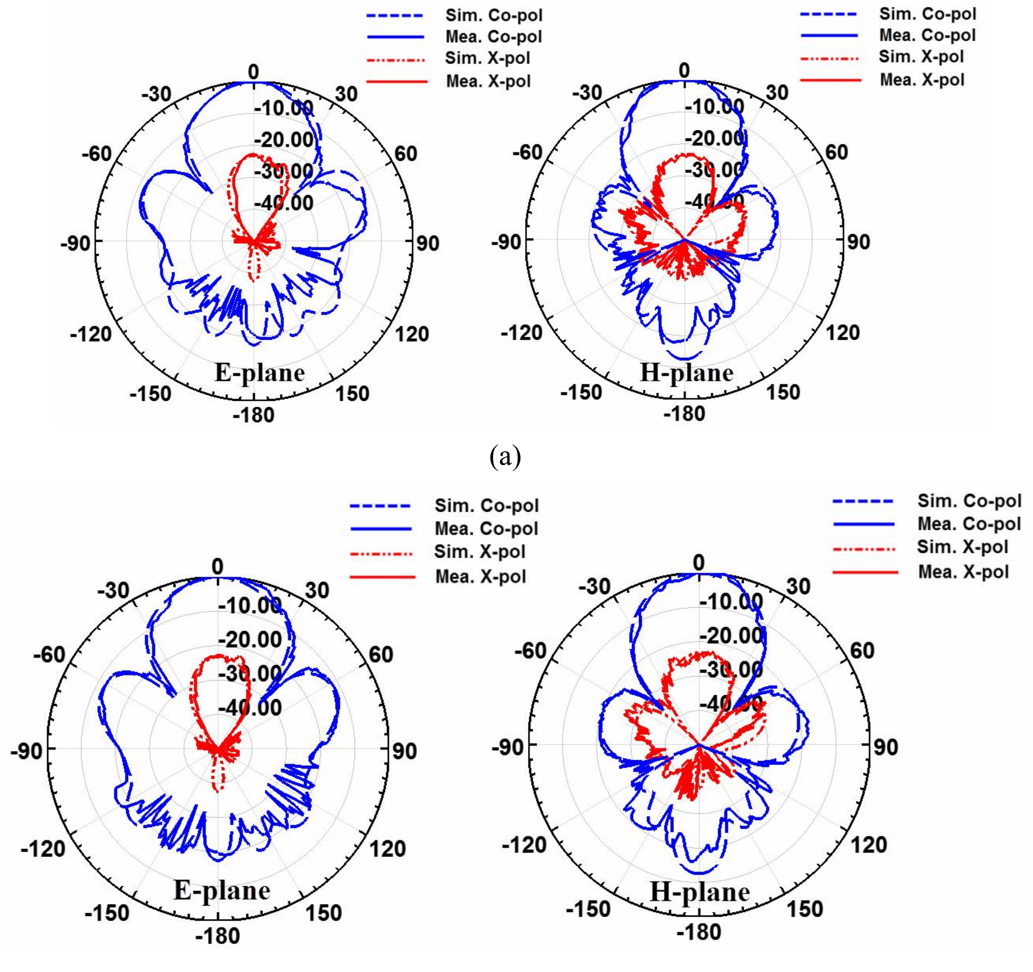

(a)

(b)

Figure 3.39 Simulated and measured radiation patterns of the filtering antenna subarray at 37 GHz. (a) Excitation at P1 and (b) Excitation at P2.

Far-field results are measured in an anechoic chamber. The gain measurement is conducted at the boresight of the proposed antenna subarray. As shown in Figure 3.38, the maximum measured gain is 10.8 dBi within the passband. It should be pointed out that, the connector loss has been de-embeded based on the data sheet of the super SMA [95]. Measured gain responses also agree well with simulated results. Figure 3.39 plots measured radiation patterns at 37 GHz for both polarization directions. The achieved cross-polarization level is about 22 dB lower than its co-polarization counterpart. Even if the individual array patterns shown in Figure 3.39 have no grating lobes, conventional beamforming with periodic distributed digital subarrays will have an output response with grating lobes that would increase the peak sidelobe level [96]. Several solutions based on heuristic algorithms (e.g. Genetic Algorithm (GA) [97] and Particle Swarm Optimiser (PSO) [98]) can be implemented to overcome this problem in subarrays.

3.4 Summary

In this chapter, two filtering antenna arrays are proposed for radar tracking systems and 5G base stations, respectively. Investigations show that, the challenge of constructing a filtering antenna array lies in the proper design of its feeding network. Filters with multiple inputs/outputs, whose design specifications can be analyzed from their counterparts with one input & output, are established as references for further filter-antenna synthesis. Prototypes, with monopulse and dual-polarization functions, are physically realized and verified in the measurement, respectively. These proposed filtering antenna arrays expand the application area for this kind of a multifunctional component.

Chapter 4 Implementation of Synthetic Material in Dielectric Resonator Based Filtering Antennas for Broadband Applications

This chapter presents a filtering antenna, whose radiator is a dielectric resonator (DR). In the design procedure, relationships between parameters of a dielectric resonator and its external quality factor (Q_{EXT}) are analyzed. Results obtained from this exploration indicate that a broad bandwidth of 15.5% is achievable for a filtering antenna [2nd-order, RL<15 dB] by using a DR as the radiator. In order to achieve Q_{EXT} values required in different design specifications, for the first time, the utilization of synthetic material with air-filled holes is proposed to continuously adjust the Qext of a DRA. The above two steps also enable the synthetic DR to not only act as a radiator, but also the last resonator of a bandpass filter. A 2nd-order prototype centered at 11 GHz with a bandwidth of 950 MHz is successfully demonstrated using the proposed design procedure. Experimental results also verified the predictions in the simulation.

4.1 Introduction

Different types of radiators have been implemented in the design of a filtering antenna, using the approach proposed by Person *et al.* in [4]. In [30], the use of rectangular patch antennas was reported for a filtering array design. A monopole antenna was applied in [25]. Cavity-backed slot antennas were implemented for filtering antenna designs, in either a planar integration [27] or a 3-D integration [28]. However, there is no such kind of a design using dielectric resonator antennas (DRAs) in reported articles. The structure with a cylinder DR proposed by Leung *et al* in [29] is not a filtering antenna, but two devices sharing a common resonator.

The reason that the DRA is attractive for radiator designs in filtering antennas is not only due to its advantages such as low fabrication cost, low loss (no conductor loss), small size, light weight, reasonable bandwidth (~10% for ε_r ~10) and high radiation efficiency. More importantly, unlike those radiators of dipole, monopole and patch, the resonant frequency of a DR radiator is determined by three dimension parameters (length, width and height), which enables a design flexibility in the continuous choice of bandwidth for a filtering antenna.

The DRA is an antenna that makes use of radiating modes of a dielectric resonator (DR). The DRA is a 3-dimensional device and was first proposed in 1983 [96] in a rectangular shape. It can also be constructed in other shapes, e.g., hemispherical, cylindrical, triangular, etc. The resonant frequency of a DRA is determined by its dimensions and dielectric constant ε_r. Different kinds of feeding technology can be implemented for the excitation of a DRA, such as microstrip line feed [97], aperture coupled feed [98] and coaxial feed [99]. Besides linearly polarized DRAs [96], circularly polarized [100] and even omni-directional circularly polarized [101] antennas can also be realized using dielectric resonators, with the help of parasitic strips. Dual-band [102] and wide-band [103] DRAs have also been proposed.

DRA technology suffers from several inherent limitations as well. Those limitations are mainly related to the variation of the electrical properties of the used material and the integration between DR and its feeding network.

4.2 Q_{EXT} Extraction of a DRA Operating at Its TE^{y}_{111} Mode.

The Q_{EXT} extraction is a key issue in the replacement of the last-stage resonator in the reference filter by a DRA. In this investigation, a DRA whose TE^{y}_{111} mode resonates at 11 GHz, which is also the center frequency of the reference filter, has been implemented. The center frequency f_0 can be achieved as [104]:

$$f_0 = \frac{c}{2\pi\sqrt{\varepsilon_r}}\sqrt{k_x^2 + k_y^2 + k_z^2} \tag{4.1}$$

$$k_x = \frac{\pi}{L}, k_z = \frac{\pi}{2W} \tag{4.2}$$

$$\tan\left(\frac{H}{2}k_x\right) = \left(\frac{k_{x0}}{k_x}\right), k_{x0} = \sqrt{k_y^2 + k_z^2} \tag{4.3}$$

The simulation model used for the extraction of Q_{EXT} is illustrated in Figure 4.1. A rectangular DRA is placed above a ground plane and coupled with a waveguide through a rectangular coupling slot. Input of the waveguide is assumed to be port 1.

For the purpose of realizing a single-mode operation, the waveguide is filled by a material of $\varepsilon_r = 10.2$. As we all know, Q_{EXT} can be expressed by

$$\frac{1}{Q_{EXT}} = \frac{1}{Q_L} - \frac{1}{Q_U} \tag{4.4}$$

It can be noticed that, when assuming the DRA to be lossless ($Q_U = \infty$), Q_{EXT} will be identical to Q_L. Therefore, Q_{EXT} of the DRA can be obtained by removing its

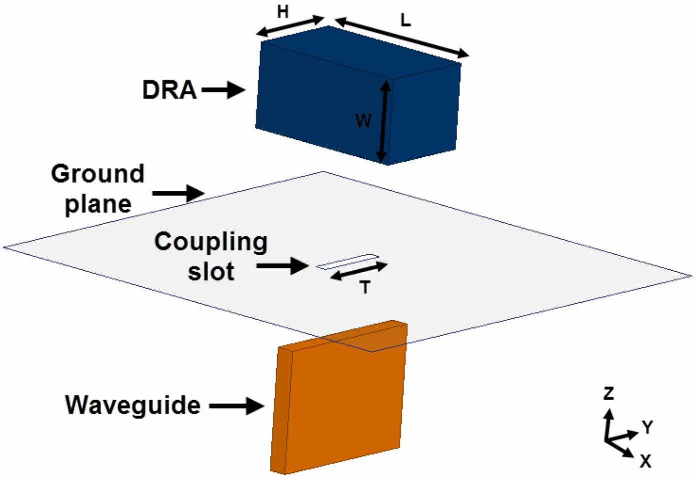

Figure 4.1 Simulation model used to extract the Q_{EXT} of a DRA operating at its TE^y_{111} mode.

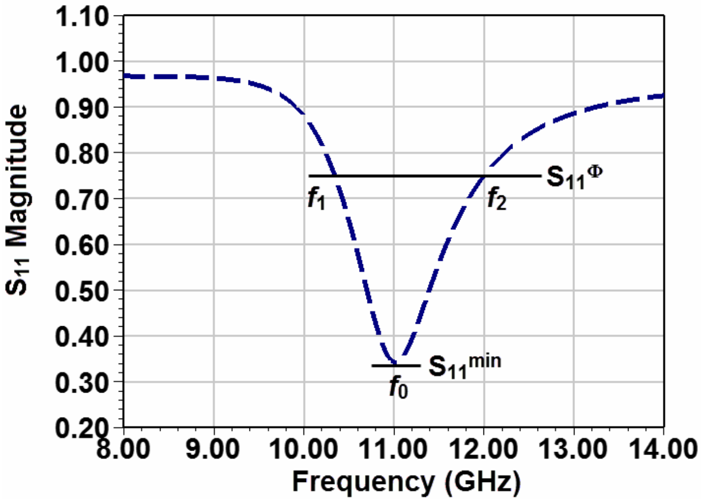

Figure 4.2 Reflection coefficients of the model used for permittivity extraction.

dielectric loss in the simulation and extracting the value of Q_L. Using the method described in [105], Q_L can be extracted from the reflection coefficients of the waveguide port 1. In Figure 4.2, $S_{11}^{\min}$ is the minimum reflection coefficient occurring at the resonant frequency f_0. f_1 and f_2 are those frequencies when $S_{11}= S_{11}^{\Phi}$, where S_{11}^{Φ} is defined as

$$S_{11}^{\Phi} = \sqrt{\frac{1+\left|S_{11}^{\min}\right|^2}{2}} \tag{4.5}$$

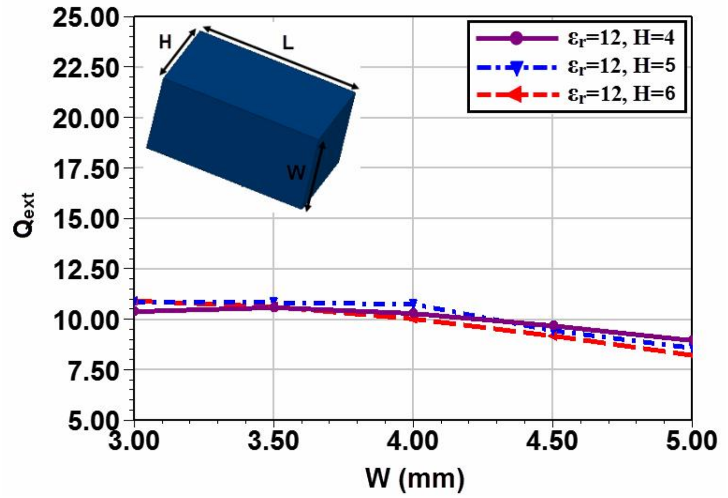

Figure 4.3 Extracted Q_{ext} of a DRA versus its width "H" with different height "W" as a parameter.

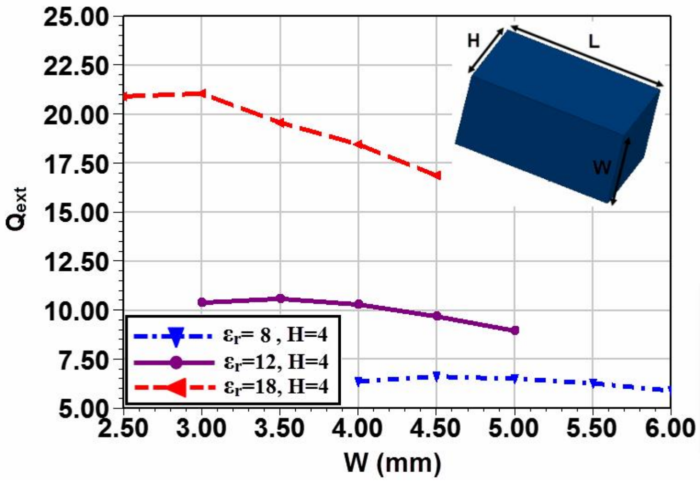

Figure 4.4 Extracted Q_{ext} of a DRA versus its permittivity ε_r with different height "W" as a parameter.

The coupling coefficient k between the waveguide port and the resonator can be found using

$$k = \frac{1 - S_{11}^{\min}}{1 + S_{11}^{\min}} \quad \text{(resonator is under-coupled)} \tag{4.6}$$

$$k = \frac{1 + S_{11}^{\min}}{1 - S_{11}^{\min}} \quad \text{(resonator is over-coupled)} \tag{4.7}$$

The Q_L can be calculated using

$$Q_L = (1 + k)\frac{f_0}{f_2 - f_1} \tag{4.8}$$

Figure 4.3 plots the extracted Q_{EXT} of the DRA versus its width H with different height W as a parameter, when the permittivity of the material is $\varepsilon_r = 12$. Figure 4.4 shows the extracted Q_{EXT} versus its permittivity ε_r with different height W as a parameter, when the width H of the DRA remains 4 mm. It should be pointed out that, the resonance of the DRA is always kept unchanged at the 11 GHz, by varying the length L. As can be observed and compared in these two figures, changing the permittivity of the utilized material can bring in a larger range of achievable Q_{EXT}, which can also enable a much wider filter bandwidth. Moreover, it can also be estimated from Figure 4.3 that, achieving a Q_{EXT} larger than 12.5 is almost impossible by reducing the value of W, since W=3mm is already very close to the minimum height of this DRA that resonates at 11 GHz. Therefore, we can draw a conclusion that, it is more feasible to achieve the required Q_{EXT} by changing the permittivity of the material used for the DRA.

Table 4.1 Performance Comparison between Filtering Antennas with Different Radiators

Radiator Type	Order	Design Flexibility in Continuous Bandwidth	Achievable Bandwidth
Patch [15]	2nd-order	No	2%
Slotline Dipole [4]	3rd-order	No	15%
Monopole [25]	3rd-order	No	16.3%
Cavity-Backed Slot [27]	4th-order	Yes	0.8% — 8%
Dielectric Resonator	2nd-order	Yes	4.4% —15.5%

A performance comparison between filtering antennas with different radiators is conducted in Table 4.1. It can be seen that, all these radiators utilized in the construction of a filtering antenna, which can be categorized into the third design approach, perform only one resonance. This is to ensure that the synthesis of such a filtering antenna can follow a filter design procedure, so that the performance of it can also exactly follow the one of its reference filter. However, among these radiators, only resonant frequencies of the cavity-backed slot and dielectric resonator are determined by more than one dimension parameters, providing design flexibility in the continuous choice of bandwidth for a filtering antenna. When compared with the DRA, the cavity-backed slot antenna is a high Q-factor radiator which is always narrow band [1.7% in [73], 1.5% in [74]]. Even when using a 3.17-mm-thick multilayer RT/Duroid 5880 substrate [27], the achievable minimum Q_{ext} is still around 12, which corresponds to a maximum bandwidth of only 8% [4th-order, RL<20 dB] and 7.7% [2nd-order, RL<15 dB (same as our case)]. Therefore, the bandwidth of a filtering antenna using this kind of a radiator is very hard to be beyond 10%, which reflects the advantage of using DR as the radiator for broadband filtering antenna designs.

4.3 Continuous adjustment of Q_{EXT} of a rectangular dielectric resonator using synthetic dielectric

As discussed above, it is preferred to realize a certain Q_{EXT} for a DRA by changing its permittivity. However, there is one major problem when applying this method, which is, the available permittivity in reality is limited and may not satisfy the specifications required in a filtering antenna. Synthetic dielectric [106], [107], by introducing air-filled holes into the host dielectric, is a good option to solve this problem. The concept of synthesized dielectric has been proposed for over 20 years, while its application is still restricted mainly in two areas: permittivity reduction of substrate [106] and flat lens [107]. Since the effective permittivity ε_{reff} of the synthesized dielectric can be determined by the volume fraction of the host dielectric relative to air, in our design, the utilization of such kind of dielectric is proposed to continuously adjust Q_{ext} for a DR radiator within a certain range, so that filtering antennas with different design specifications can be successfully fulfilled. It should be noticed that, the ε_{reff} of the synthetic dielectric is always smaller than the ε_r of the host dielectric.

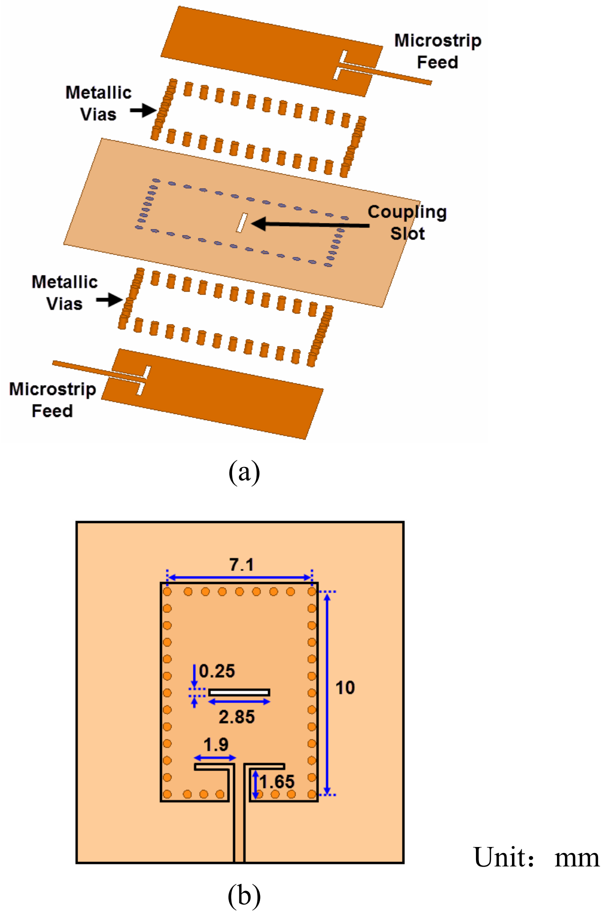

Figure 4.5 (a) Cross-section view and (b) top view of the reference 2nd-order SIW cavity BPF.

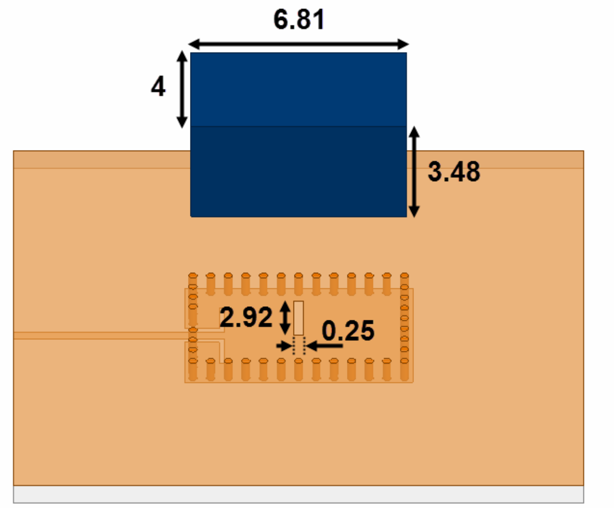

Figure 4.6 Cross-section view of the filtering antenna using ideal dielectric.

4.4 Prototype Demonstration

A prototype operating at 11 GHz with a bandwidth of 950 MHz is demonstrated

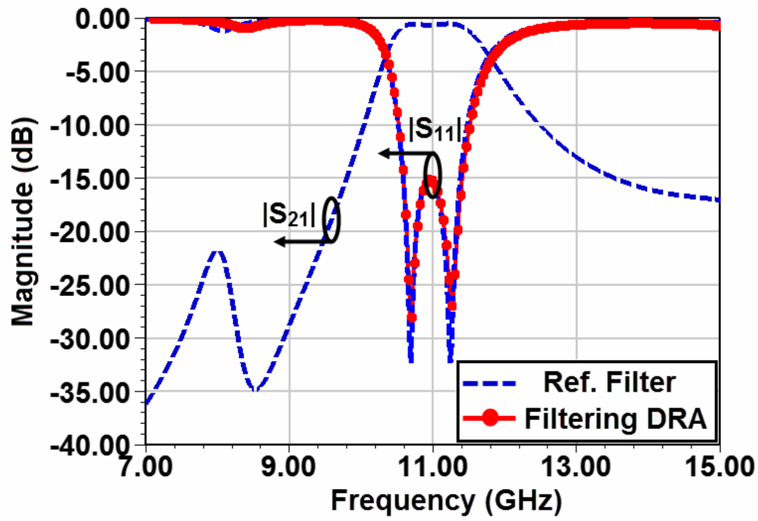

Figure 4.7 Simulated frequency responses of the reference filter and the filtering DRA in Figure 4.6.

in this section, to show the capability of a filtering antenna design with the dielectric resonator radiator.

4.4.1 Reference Filter Synthesis

The prototype is based on a 2nd-order Chebyshev bandpass filter, whose resonators are TE_{201}-mode SIW cavities. As observed in the filter structure shown in Figure 4.5, these two resonators are vertically cascaded and coupled through a rectangular slot. Rogers RO3010 substrate, whose thickness for each substrate layer is 25 mil, is implemented in this prototype. The width of the coupling slot for the two 50-Ω microstrip lines is 0.25 mm. For a 2nd-order filter with in-band return loss of 15 dB, design parameters are:

$$k_{12} = 0.11 \tag{4.9}$$

$$Q_{EXT} = 10.77 \tag{4.10}$$

Dimensions of the filter are obtained as described in [76] and shown in Figure 4.5(b).

4.4.2 Realization of A Filtering Antenna Using Ideal Dielectric

Based on the required Q_{EXT} in the design parameters of the reference filter, a material with dielectric constant of 12 is chosen for the DRA, in the filtering antenna synthesis procedure. The initial height and width are 4 mm and 3.5 mm, respectively. In order to simultaneously evaluate the external coupling, the internal coupling and the frequency loading effect to the DRA, the method proposed in [28] has been implemented to achieve a bandwidth of 950 MHz. It should be pointed out that, the length T of the coupling slot is responsible for identical internal coupling strength and also need to be carefully optimized. Frequency responses for the reference filter and filtering antenna with dimension in Figure 4.6 are compared in Figure 4.7. A very good correspondence can be observed between curves of the in-band return loss.

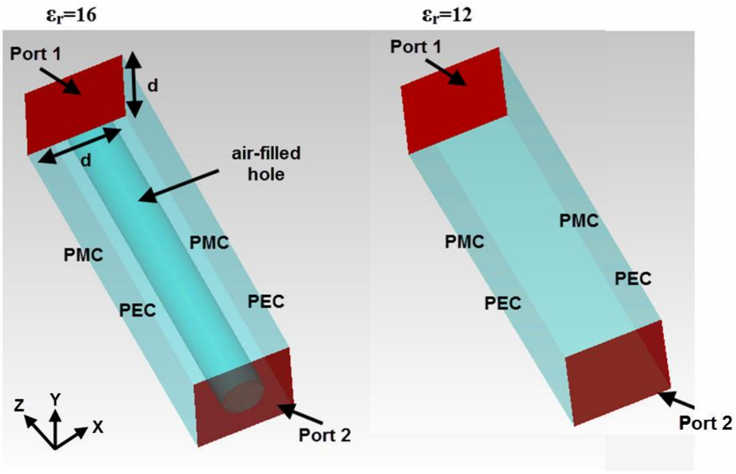

(a) (b)

Figure 4.8 HFSS simulation models for extracting the electromagnetic characteristics along Z-axis of (a) synthetic dielectric with the air-filled hole and (b) conventional dielectric.

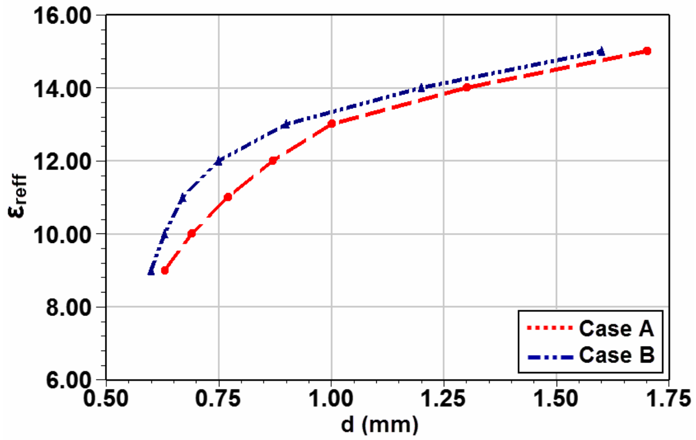

Figure 4.9 Extracted ε_{reff} along Z-axis [Case A] and X-&Y-axis [Case B] of the simulation model in Figure 4.8(a).

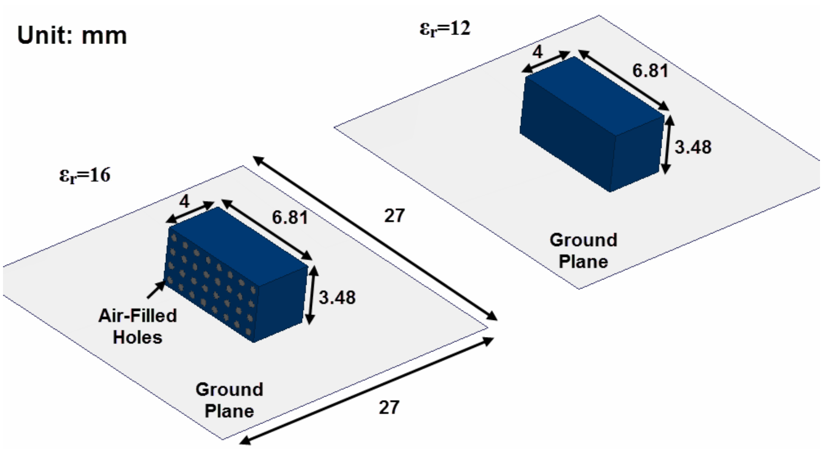

(a) (b)

Figure 4.10 HFSS simulation models for the verification of permittivity extraction of (a) synthetic dielectric with air-filled holes and (b) conventional dielectric.

4.4.3 Realization of A Filtering Antenna Using Synthetic Dielectric

Some available permittivity of host dielectric provided by the manufacturer is ε_r = 6, 10 and 16. Since the synthesized permittivity is always smaller than the one of the host material, the dielectric material with ε_r = 16 is chosen in this design for the realization of a synthetic dielectric with ε_{reff}=12. A square lattice of circular holes is

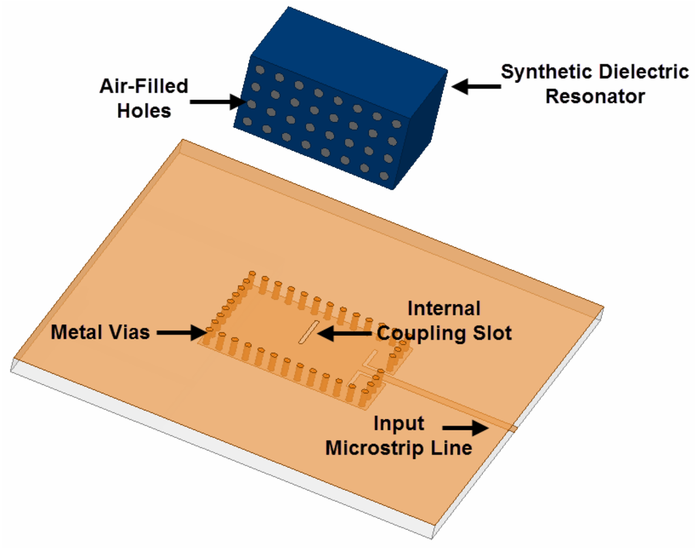

Figure 4.11 The geometry of a 2nd-order filtering antenna using a synthetic dielectric resonator as the radiator.

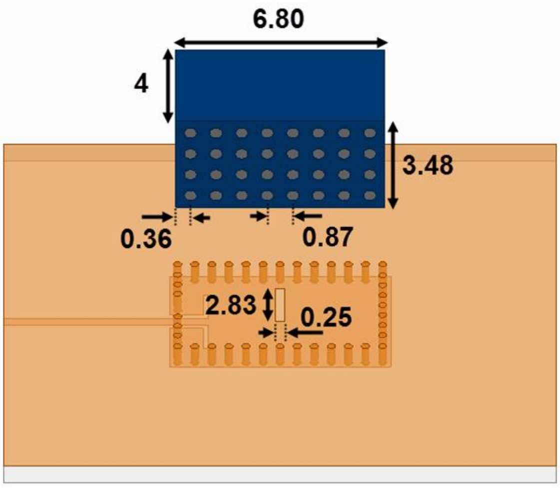

Figure 4.12 Cross-section view of the filtering antenna using synthetic dielectric.

employed in synthesized dielectric in our design, the effective permittivity $\varepsilon_{\text{reff}}$ is proportional to the volume of the substrate removed and can be calculated by

$$\varepsilon_{reff} = \frac{\varepsilon_r \cdot (d^2 - \pi \cdot a^2) + \pi \cdot a^2}{d^2} \tag{4.11}$$

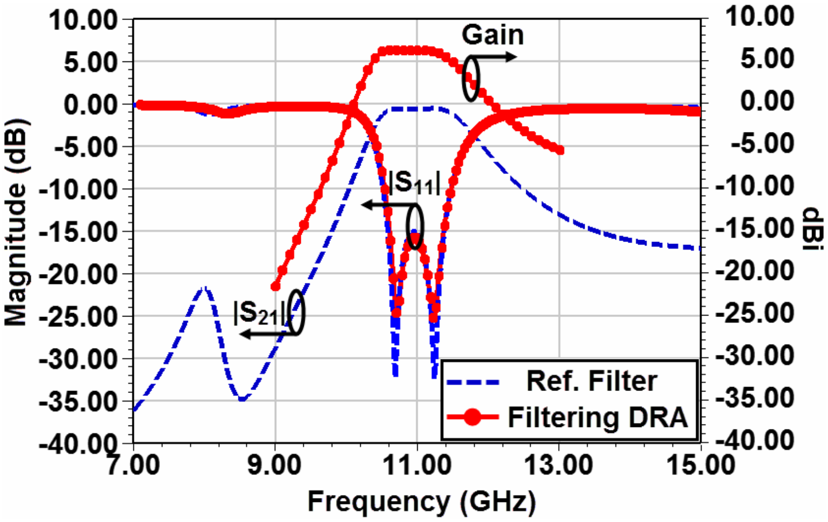

Figure 4.13 Simulated frequency responses of the reference filter and the filtering DRA in Figure 4.12.

where *d* is the distance between holes in the square lattice, *a* is the radius of each hole, and ε_r is the substrate relative permittivity. In our case, a dielectric material with ε_r = 16 is chosen for the realization of a synthetic dielectric with ε_{reff}=12. For a fixed *a*=0.2 mm, *d* is initially calculated to be 0.7 mm.

Then, periodic boundaries [108] are applied to simulation models of a cell as shown in Figure 4.8 to obtain the exact value of *d*. The radius *a* of the air-filled hole in Figure 4.8(a) is restricted to be 0.2 mm. By comparing the phase delay obtained in the two models in Figure 4.8, extracted values of ε_{reff} along Z-axis [Case A] and X-&Y-axis [Case B] are plotted in Figure 4.9. It can be observed that, ε_{reff} is indeed anisotropic along different axes. The change of slope of Case B is faster than the one of Case A and ε_{reff} is close to each other after d>1.5 mm. In Case A, when the

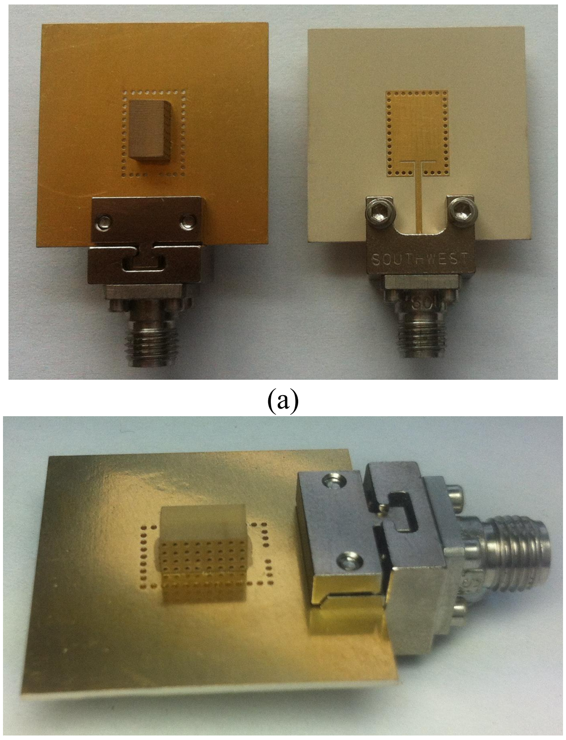

(a)

(b)

Figure 4.14 (a) Top view and bottom view and (b) cross-section view of the fabricated filtering antenna prototype.

space *d* between adjacent cells equals to 0.87 mm, a best matching can be achieved. It is also noted that, the difference of $\varepsilon_{\mathrm{reff}}$ between the two cases is only 0.7 when d is around 0.87 mm. This small discrepancy can be adjusted in the final optimization of the DRA's dimensions after the synthetic dielectric is utilized to replace the original dielectric.

The resonances of the TE^{y}_{111} mode have also been compared between two DRAs with those parameters obtained above. Detailed dimensions of the two DRAs are illustrated in Figure 4.10. It is found that, the resonant frequency of the DRA with ideal dielectric is 10.9769 GHz, which is very close to10.9441 GHz of the DRA with

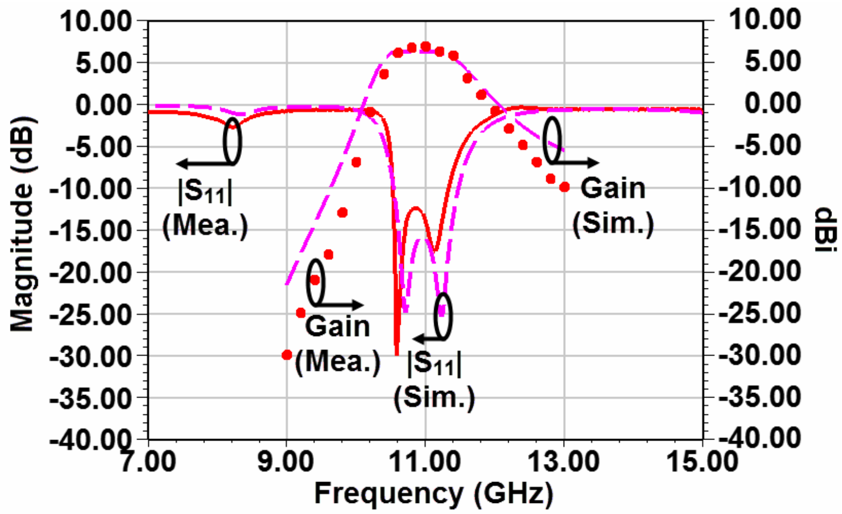

Figure 4.15 Simulated and measured $|S_{11}|$ results and gain of the proposed filtering antenna.

synthetic dielectric. The small discrepancy is reasonable, due to the fact that the DRA in Figure 4.10(b) is not an ideal periodic structure. As a result, an optimization needs to be conducted to modify the whole filtering antenna with synthetic dielectric shown in Figure 4.11. Finalized parameters are plotted in Figure 4.12. A good correspondence of return loss can be achieved between the reference filter and the filtering antenna. The filtering shape of the gain responses for the filtering antenna also basically follows the one of the transmission coefficients of the reference filter.

4.5 Measurement Results and Discussions

Figure 4.14 shows the photo of the fabricated filtering antenna. A 2.92mm Southwest super SMA connector is used to connect the microstrip input of the antenna for measurement. Simulated and measured results are compared in Figure 4.15. The achieved bandwidth is 840 MHz for $|S_{11}|<-10$ dB, which is slightly smaller

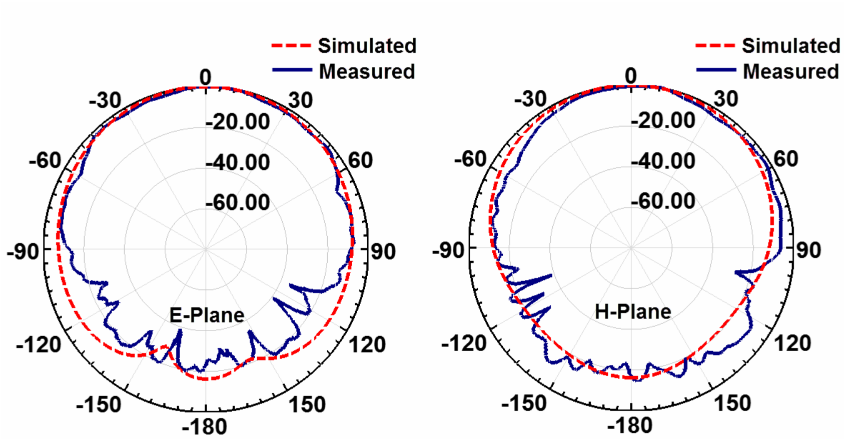

Figure 4.16 Simulated and measured radiation patterns at 11 GHz for the filtering antenna.

than the one obtained in the simulation. The fabrication tolerance in the shaping of the DRA could be the dominant reason for this discrepancy. Far-field results are measured in an anechoic chamber. Gain results are obtained at the broadside of the proposed filtering antenna. Maximum measured gain within the passband is 6.45 dBi. The overall loss for the filtering antenna is estimated to be 0.45 dB [simulated directivity (6.9 dBi) - measured gain (6.45 dBi)], which is very close to the calculated insertion loss of 0.42 dB based on the unloaded quality factor of the SIW cavity [Q_u=267] and the DR radiator [Q_u=1007]. Those measured radiation patterns at 11 GHz are given in Figure 4.16 and also match well with simulated results.

4.6 Conclusion

A DR radiator based on the synthetic dielectric is successfully implemented in the design of a broadband filtering antenna. The design is based on the exploration of the external quality factor of a DRA versus its parameters. Investigations show that, changing the permittivity of the DR can provide a larger variation range for the external quality factor than changing its dimensions. A 2nd-order prototype operating at 11 GHz is designed, fabricated and measured for a validation.

Chapter 5 Conclusion and Proposal for Future Research

This thesis sets out to analyze and design SIW cavity-based filtering antennas with radiation nulls for their broadside gain, and to implement proper feeding network to expand filtering antennas from element designs to array designs. In this final chapter, the primary contributions of this research are summarized and suggestions for future work in this area are provided.

5.1 Contributions

Since most published filtering antennas are element designs and based on transmission line structures, the motivation for this thesis is to implement the SIW technology for filtering antenna and antenna array designs, to realize high selectivity or certain functions. Gradient-based optimization method is used for synthesizing the reference filter before the antenna-filter integration. The major original contributions are made below.

In Chapter 2, cross-couplings in a multi-mode cavity and a gradient-based filter synthesis procedure are selected for the generation of radiation nulls for SIW cavity filtering antennas. Two designs examples are proposed. The first one is a filtering antenna composed of two vertically stacked SIW cavities. There are two major advantages for this proposed filtering antenna, which are the high frequency selectivity and low cross-polarization levels, respectively. A multi-mode coupling scheme realized in a single cavity and a dual-slot cavity-backed antenna are developed to achieve required performances. The second one is an SIW filtering antenna array with quasi-elliptic gain responses. The key to achieve high out-of-band gain attenuation is the utilization of an oversized TE_{103}-mode cavity. The power division for the two antenna elements can also be achieved by using this cavity.

In Chapter 3, SIW cavity filtering antennas are expanded from element to array designs. A filtering 4-element antenna array which can realize monopulse functions is proposed in Section 3.2. A dual-mode square cavity (TE_{102} and TE_{201}) with proper inputs and outputs is designed to act as the monopulse comparator. A null depth around 27 dB is achieved in the difference channel, when measured in the chamber. The proposed design can be easily further expanded to an array with more elements. A filtering 4-element antenna array which can realize dual-polarization functions is proposed in Section 3.3. By utilizing the LTCC technology, a dual-path reference filter, with one input and four outputs for each path, is developed. These two paths are isolated from each other by utilizing different kinds of coupling structures, in order to achieve a low cross-polarization level when the end resonators are replaced by cavity-backed slot antennas. An isolation better than 32 dB is measured between two input ports, while the cross-polarization level is better than 22 dB in the measurement. The configuration of the proposed design fully exploits the three-dimensional integration feature of the LTCC technology.

In Chapter 4, a dielectric resonator is applied as the radiator in a filtering antenna for broadband applications. Investigations indicate that, the quality factor of a dielectric resonator can be effectively tuned by changing its permittivity. In order to obtain the dielectric resonator with a required permittivity, which is not available in real world, the concept of synthetic material is implemented. With proper filter-antenna integration, the dielectric resonator and SIW resonator are capable to be integrated as filtering antennas and achieve a fractional bandwidth larger than 10%.

5.2 Future Research

The above research contributions suggest many more specific open questions and directions. The remainder of this section will lay out some of these more immediately accessible avenues for future research.

1. For SIW based filtering antennas, designs with duplex function, dual-band or circular polarization are desired to be developed. It could be estimated that, multi-mode cavities will be essential to achieve the above functions.

2. Since filtering antennas using multiple resonators, whose design procedure follows a filter synthesis method, suffer from high insertion loss brought by

resonators included, those design methods without additional resonators but still can achieve the filtering function for gain responses are highly desirable. Related explorations can be conducted based on the mode analysis for SIW cavities.

3. Most published filtering antennas are driven by academic purposes, which do not have a specific target application. Therefore, it is of critical importance to investigate those areas where filtering antennas can be implemented. One possible application area is the shared-aperture antenna array, where high isolation is required between antenna arrays operating at different frequency ranges. In conventional designs, such kind of an array is usually designed for two frequency ranges. The polarization directions of those radiation elements for different frequency ranges should be orthogonal to each other. Furthermore, the two operating frequency ranges can not be too close to each other. All these restrictions are aimed to ensure the isolation. However, if the filtering antenna concept can be implemented in such kind of an array, the constrain of orthogonal polarizations can be omitted, as long as the attenuation in the filter response at certain frequency ranges can meet those system requirements. Another advantage is that, the shared aperture array can be designed for more frequency ranges other than two.

Bibliography

[1] K. Linehan and R. Chandrasekaran, “Active Antennas: The Next Step in Radio and Antenna Evolution,” Tech. Rep., 2011 [On-line]. Available: http://docs.commscope.com/Public/active_an-tenna_system_white_paper.pdf

[2] K. Chang, R. A. York, and P. S. Hall, “Active integrated antennas,” *IEEE Trans. Microw. Theory Tech.*, vol. 50, no. 3, pp. 937-944, Mar. 2002.

[3] R. S. Adams, Be. O'Neil, and J. L. Young, “The circulator and antenna as a single integrated system,” *IEEE Antennas Wireless Propag. Lett.*, vol. 8, pp. 165-168, May 2008.

[4] T. L. Nadan, J. P. Coupez, S. Toutain, and C. Person, “Integration of an antenna/filter device, using a multi-layer, multi-technology process,” *in Proc. 28th Eur. Microw. Conf.*, Oct. 1998, vol. 1, pp. 672–677.

[5] J. Hirokawa and M. Ando, “Single-layer feed waveguide consisting of posts for plane TEM wave excitation in parallel plates,” *IEEE Trans. Antennas Propag.*, vol. 46, no. 5, pp. 625-630, May 1998.

[6] J. H. Zuo, X. W. Chen, G. R. Han, L. Li, and W. M. Zhang, “An integrated approach to RF antenna- filter co-design,” *IEEE Antennas Wireless Propag. Lett.*, vol. 8, pp. 141–144, Jan. 2009.

[7] C. Yu, W. Hong, Z. Kuai, and H. Wang, “Ku-band linearly polarized omnidirectional planar filtenna,” *IEEE Antennas Wireless Propag. Lett.*, vol. 11, pp. 310–313, Mar. 2012.

[8] G. Q. Luo, W. Hong, H. J. Tang, J. X. Chen, X. X. Yin, Z. Q. Kuai, and K. Wu, “Filtenna consisting of horn antenna and substrate integrated waveguide cavity FSS,” *IEEE Trans. Antennas Propag.*,vol.55,no.1, pp. 92–98, Jan. 2007.

[9] X. Y. Zhang, W. Duan, and Y.-M. Pan, “High-gain filtering patch antenna without extra circuit,” *IEEE Trans. Antennas Propag.*, vol.63, no.12, pp. 5883–5888, Dec. 2015.

[10] P. F. Hu, Y. M. Pan, X. Y. Zhang, and S. Y. Zheng, “A compact filtering dielectric resonator antenna with wide bandwidth and high gain,” *IEEE Trans. Antennas Propag.*, vol.64, no.8, pp. 3645–3651, Aug. 2016.

[11] Y. Zhang, X. Y. Zhang, L.-H. Ye, and Y.-M. Pan, “Dual-band base station array using filtering antenna elements for mutual coupling suppression,” *IEEE Trans. Antennas Propag.*, vol.64, no.8, pp. 3645–3651, Aug. 2016.

[12] S. W. Wong, T. G. Huang, C. X. Mao, Z. N. Chen, and Q. X. Chu, “Planar filtering ultra-wideband (UWB) antenna with shorting pins,” *IEEE Trans. Antennas Propag.*, vol.61, no.2, pp. 948–953, Feb. 2013.

[13] H. Mardani, C, Ghobadi, and J. Nourinia, “A simple compact monopole antenna with variable single- and double-filtering function for UWB applications,” *IEEE Antennas Wireless Propag. Lett.*, vol. 9, pp. 1076–1079, Nov. 2010.

[14] Z. H. Tu, W. A. Li, and Q.-X. Chu, “Single-layer differential CPW-fed notch-band tapered-slot UWB antenna,” *IEEE Antennas Wireless Propag. Lett.*, vol. 13, pp. 1296–1299, Jul. 2014.

[15] C. K. Lin and S. J. Chung, “A compact filtering microstrip antenna with quasi-elliptic broadside antenna gain response,” *IEEE Antennas Wireless Propag. Lett.*, vol. 10, pp. 381–384, 2011.

[16] Xi. Chen, F. Zhao, L. Yan, and W. Zhang, “A compact filtering antenna with flat gain response within the passband,” *IEEE Antennas Wireless Propag. Lett.*, vol. 12, pp. 857–860, 2013.

[17] C.-X. Mao, S. Gao, Y. Wang, F. Qin, and Q.-X. Chu, “Compact highly integrated Planar duplex antenna for wireless communications,” *IEEE Trans. Microw. Theory Tech.*, vol. 64, no. 7, pp. 2006-2013, Jul. 2016.

[18] Y.-J. Lee, J.-H. Tarng, and S.-J. Chung, “A filtering diplexing antenna for dual-band operation with similar radiation patterns and low cross-polarization levels,” *IEEE Antennas Wireless Propag. Lett.*, vol. 16, pp. 58-61, Apr. 2017.

[19] C.-Y. Hsieh, C.-H. Wu, and T.-G. Ma, "A compact dual-band filtering patch antenna using step impedance resonators," *IEEE Antennas Wireless Propag. Lett.*, vol. 14, pp. 1056–1059, 2015.

[20] C. X. Mao, S. Gao, Y. Wang, B. Sanz-Izquierdo, Z. Wang, F. Qin, Q. X. Chu, J. Li, G. Wei, and J. Xu, "Dual-band patch antenna with filtering performance and harmonic suppression," *IEEE Trans. Antennas Propag.*, vol.64, no.9, pp. 4074–4077, Sep. 2016.

[21] W. Duan, X. Y. Zhang, Y.-M. Pan, J.-X. Xu, and Q. Xue, "Dual-polarized filtering antenna with high selectivity and low cross polarization," *IEEE Trans. Antennas Propag.*, vol.64, no.10, pp. 4188–4196, Oct. 2016.

[22] C.-X. Mao, S. Gao, Y. Wang, F. Qin, and Q.-X. Chu, "Multimode resonator-fed dual-polarized antenna array with enhanced bandwidth and selectivity," *IEEE Trans. Antennas Propag.*, vol.63, no.12, pp. 5492–5499, Dec. 2015.

[23] Z. H. Jiang and D. H. Werner, "A compact, wideband circularly polarized co-designed filtering antenna and its application for wearable devices with low SAR," *IEEE Trans. Antennas Propag.*, vol.63, no.9, pp. 3808–3818, Sep. 2015.

[24] Z. H. Jiang, M. D. Gregory, and D. H. Werner, "Design and experimental investigation of a compact circularly polarized integrated filtering antenna for

wearable biotelemetric devices," *IEEE Trans. Biomed. Circuits Syst.*, vol.10, no.2, pp. 328–338, Apr. 2016.

[25] W. Wei-Jun, Y. Ying-Zeng, Z. Shao-Li, Z. Zhi-Ya, and X. Jiao-Jiao, "A new compact filter-antenna for modern wireless communication systems," *IEEE Antennas and Wireless Propag. Lett.*, vol. 10, pp. 1131–1134, Oct. 2011.

[26] C.-T. Chuang and S.-J. Chung, "A compact printed filtering antenna using a ground-intruded coupled line resonator" *IEEE Trans. Antennas Propag.*, vol.59, no.10, pp. 3630–3637, Oct. 2011.

[27] Y. Yusuf and X. Gong, "Compact low-loss integration of high-Q 3-D filters and highly efficient slot antennas," *IEEE Trans Microw. Theory Tech.*, vol. 59, no. 4, pp. 857–865, Apr. 2011.

[28] Y. Yusuf, H. T. Cheng, and X. Gong, "A seamless integration of 3-D vertical filters with highly efficient slot antennas," *IEEE Trans. Antennas Propag.*, vol. 59, no. 11, pp. 4016–4022, Nov. 2011.

[29] E. H. Lim and K. W. Leung, "Use of the dielectric resonator antenna as a filter element," *IEEE Trans. Antennas Propag.*, vol. 56, no. 1, pp. 5–10, Jan. 2008.

[30] C.-K. Lin and S.-J. Chung, "A filtering microstrip antenna array," *IEEE Trans. Microw. Theory Tech.*, vol. 59, no. 11, pp. 2856–2863, Nov. 2011.

[31] Y. Yusuf, H. Cheng, and X. Gong, “Co-designed substrate-integrated waveguide filters with patch antennas,” *IET Microw. Antennas Propag.*, vol. 7, no. 7, pp. 493–501, May 2013.

[32] J. Hirokawa and M. Ando, “Single-layer feed waveguide consisting of posts for plane TEM wave excitation in parallel plates,” *IEEE Trans. Antennas Propag.*, vol. 46, no. 5, pp. 625–630, May 1998.

[33] D. Deslandes and K. Wu, “Integrated microstrip and rectangular waveguide in planar form,” *IEEE Microw. Wireless Compon. Lett.*, vol. 11, no. 2, pp. 68–70, Feb. 2001.

[34] M. J. Hill and R. W. Ziolkowski, J. Papapolymerou, “Simulated and measured results from a Duroid-based planar MBG cavity resonator filter,” *IEEE Microw. Wireless Compon. Lett.*, vol. 10, no. 12, pp. 528–530, Dec. 2010.

[35] R. E. Collin, Foundations for Microwave Engineering. New York: McGraw-Hill, 1992.

[36] D. M. Pozar, Microwave Engineering, 2 ed. New York: Wiley, 1998.

[37] S. Mukherjee and A. Biswas, “Design of dual band and dual-polarised dual band SIW cavity backed bow-tie slot antennas,” *IET Microw. Antennas Propag.*, vol. 10, no. 9, pp. 1002–1009, Jun. 2016.

[38] A. P. Saghati and K. Entesari, “A reconfigurable SIW cavity-backed slot antenna with one octave tuning range,” *IEEE Trans. Antennas Propag.*, vol. 61, no. 8, pp. 3937–3945, Aug. 2013.

[39] J. C. Bohorquez, H. A. F. Pedraza, I. C. H. Pinzon, J. A. Castiblanco, N. Pena, and H. F. Guarnizo, “Planar substrate integrated waveguide cavity-backed antenna,” *IEEE Antennas Wireless Propag. Lett.*, vol. 8, pp. 1139–1142, Oct. 2009.

[40] B. J. Chen, T. M. Shen, and R. B. Wu, “Dual-band vertically stacked laminated waveguide filter design in LTCC technology,” *IEEE Trans. Microw. Theory Tech.*, vol. 57, no. 6, pp. 1554–1562, Jun. 2009.

[41] H. Chu and J.-X. Chen, “Dual-band substrate integrated waveguide balun bandpass filter with high selectivity,” *IEEE Microw. Wireless Compon. Lett.*, vol.24, no.6, pp. 379-381, Jun. 2014.

[42] H. Chu, P. Li, and J.-X. Chen, “Balanced substrate integrated waveguide bandpass filter with high selectivity and common-mode suppression,” *IET Microw. Antennas Propagat.*, vol. 9, no. 2, pp. 133-141, Feb. 2015.

[43] P. Li, H. Chu, and R. S. Chen, “SIW magic-T with bandpass response,” *Electron. Lett.*, vol. 51, no. 14, pp. 1078-1080, Jul. 2015.

[44] H. Chu, Y. X. Guo, Y. L. Song, and X. Q. Shi, "40/50 GHz diplexer design in LTCC technology", *Electron. Lett.*, vol. 47, no. 4, pp. 260-262, Feb. 2011.

[45] A. Collado, F. Mira, and A. Georgiadis, "Mechanically tunable substrate integrated waveguide (SIW) cavity based oscillator," *IEEE Microw. Wireless Compon. Lett.*, vol. 23, no. 9, pp. 489-491, Sept. 2013.

[46] M. L. Coq, E. Rius, J. F. Favennec, C. Quendo, B. Potelon, L. Estagerie, P. Moroni, B. Bonnet, and A. E. Mostrah, "Miniaturized C-band SIW filters using high-permittivity ceramic substrates," *IEEE Trans. Compon., Packag., Manuf. Technol.*, vol. 5, no. 5, pp. 620–626, May 2015.

[47] Z. Yang, B. Luo, J. Dong, and T. Yang, "X-band low-phase noise oscillator employing substrate integrated waveguide dual-mode filter", *Electron. Lett.*, vol. 51, no. 6, pp. 494-495, Mar. 2015.

[48] D. L. Diedhiou, E. Rius, J.-F. Favennec, and A. E. Mostrah, "Ku-band cross-coupled ceramic SIW filter using a novel electric cross-coupling," *IEEE Microw. Wireless Compon. Lett.*, vol.25, no.2, pp. 109-111, Feb. 2015.

[49] M. Esmaeili and J. Bornemann, "Quasi-elliptic triple-stopband filter based on six cross-coupled SIW resonators," *IEEE Microw. Wireless Compon. Lett.*, vol.25, no.12, pp. 802-804, Dec. 2015.

[50] H. Chu, J.-X. Chen, S. Luo, and Y.-X. Guo, “A millimeter-wave filtering monopulse antenna array based on substrate integrated waveguide technology,” *IEEE Trans. Antennas Propag.*, vol. 64, no. 1, pp. 316–321, Jan. 2016.

[51] H. Chu, Y. X. Guo, and X. Q. Shi, “60 GHz LTCC 3D cavity bandpass filter with two finite transmission zeros”, *Electron. Lett.*, vol. 47, no. 5, pp. 324-326, Mar. 2011.

[52] Z.-C. Hao, W.-Q. Ding, and W. Hong, “Developing low-cost W-band SIW bandpass filters using the commercially available printed-circuit-board technology,” *IEEE Trans. Microw. Theory Tech.*, vol. 64, no. 6, pp. 1775–1786, Jun. 2016.

[53] X.-D. Deng, Y. Li, W. Wu, and Y.-Z. Xiong, “340-GHz SIW cavity-backed magnetic rectangular slot loop antennas and arrays in silicon technology,” *IEEE Trans. Antennas Propag.*, vol. 63, no. 12, pp. 5272–5279, Dec. 2015.

[54] P. N. Choubey, W. Hong, Z.-C. Hao, P. Chen, T.-V. Duong, and J. Mei, “A wideband dual-mode SIW cavity-backed triangular-complimentary-split-ring-slot (TCSRS) antenna,” *IEEE Trans. Antennas Propag.*, vol. 64, no. 6, pp. 2541–2545, Jun. 2016.

[55] S. W. Wong, K. Wang, Z.-N. Chen, and Q.-X. Chu, “Electric coupling structure of substrate integrated waveguide (SIW) for the application of 140-GHz

bandpass filter on LTCC," *IEEE Trans. Compon., Packag., Manuf. Technol.*, vol. 4, no. 2, pp. 316–322, Feb. 2014.

[56] Y. Shang, H. Yao, H. P. Fu, and W. M. Lim,"A 239–281GHz CMOS receiver with on-chip circular-polarized substrate integrated waveguide antenna for sub-terahertz imaging," *IEEE Trans. THz Sci. Technol.*, vol.4, no.6, pp.686–695, Nov. 2014.

[57] R. Levy, "Filters with single transmission zeros at real or imaginary frequencies," *IEEE Trans. Microw. Theory Tech.*, vol. 24, no. 4, pp. 172–181, Apr. 1976.

[58] L. Gao and X. Y. Zhang, "High selectivity dual-band bandpass filter using a quad-mode resonator with source-load coupling," *IEEE Microw. Wireless Compon. Lett.*, vol. 23, no. 9, pp.474–476, Sep. 2013.

[59] H. Chu, C. Jin, J.X. Chen, and Y.X. Guo, "A 3-D millimeter-wave filtering antenna with high selectivity and low cross-polarization," *IEEE Trans. Antennas Propag.*, vol. 63, no. 5 pp. 2375–2380, May 2015.

[60] S. Amari and U. Rosenberg, "Characteristics of cross (bypass) coupling through higher/lower order modes and their applications in elliptic filter design," *IEEE Trans. Microw. Theory Tech.*, vol. 53, no. 10, pp. 3135–3141, Oct. 2005.

[61] B. R. Smith and G. C. Temes, “An iterative approximation procedure for automatic filter synthesis,” *IEEE Trans. Circuit Theory*, vol. CT-12, no.2, pp. 107–122, Mar. 1965.

[62] R. J. Cameron, “General prototype network synthesis methods for microwave filters,” ESAJ., vol.6, pp. 193-206, 1982.

[63] D. S. G. Chambers and J. D. Rhodes, “A low-pass prototype network allowing the placing of integrated poles at real frequencies,” *IEEE Trans. Microw. Theory Tech.*, vol. MTT-31, no. 1, pp. 40–45, Jan. 1983.

[64] H. C. Bell, Jr., “Canonical asymmetric coupled-resonator filters,” *IEEE Trans. Microwave Theory Tech.*, vol. MTT-30, no. 9, pp. 1333–1340, Sept. 1982.

[65] A. E. Atia and A. E. Williams, “Narrow bandpass waveguide filters,” *IEEE Trans. Microw. Theory Tech.*, vol. MTT-20, no. 4, pp. 258 –265, Apr. 1972.

[66] W. A. Atia, K. A. Zaki, and A. E. Atia, “Synthesis of general topology multiple coupled resonator filters by optimization,” in *IEEE MTT-S Int. Microwave Symp. Dig.*, Baltimore, MD, Jun. 1998, pp. 821–824.

[67] G. C. Temes and D. A. Calahan, “Computer-aided network optimization-The state of the art,” *Proc. IEEE*, vol. 55, Nov. 1967, pp. 1823-1863.

[68] J. W. Bandler, “Optimization methods for computer-aided design,” *IEEE Trans. Microw. Theory and Tech.*, vol. MTT-17, no. 8, pp. 533-552, Aug. 1969.

[69] G. R Hoffman, “Introduction to computer aided design of micro-wave circuits,” in *Proc. 14tlr European Miccrowave Conf.* (Liege, Belgium), Sept. 1984, pp. 731-737.

[70] W. Shen, X.W. Sun, W.Y. Yin, J.-F. Mao, and Q.F. Wei, “A novel single-cavity dual mode substrate integrated waveguide filter with non-resonating node,” *IEEE Microw. Wireless Compon. Lett.* , vol. 16, no. 9, pp. 368 –370, Sep. 2009.

[71] L.-S. Wu, X.-L. Zhou, Q.-F. Wei, and W.-Y. Yin, “An extended doublet substrate integrated waveguide (SIW) bandpass filter with a complementary split ring resonator (CSRR),” *IEEE Microw. Wireless Compon. Lett.* , vol. 19, no. 12, pp. 777 –779, Dec. 2009.

[72] U. Rosenberg and S. Amari, “Novel design possibilities for dual-mode filters without intracavity couplings, ” *IEEE Microw. Wireless Compon. Lett.* , vol. 12, no. 8, pp. 296 –298, Aug. 2002.

[73] G. Q. Luo, Z. F. Hu, L. S. Dong, and L. L. Sun, “Planar slot antenna backed by substrate integrated waveguide cavity,” *IEEE Antennas Wireless Propag. Lett.* , vol. 7, pp. 236–239, 2008.

[74] J. X. Li, G. Q. Luo, Y. Liang, W. J. Li, L. X. Dong, and L. L. Sun, "Cavity backed dual slot antenna for gain improvement," *Microwave and Opt. Tech. Lett.*, vol.52, no.12, pp.2767-2769, Dec. 2010.

[75] J.-S. Hong and M. J. Lancaster, *Microstrip Filters for RF/Microwave Applications*. New York: Wiley, 2001.

[76] U. Nickel, "Overview of generalized monopulse estimation', *IEEE Aerosp. Electron. Syst. Mag.*, vol. 21, no. 6, pp. 27 –56, Jun. 2006.

[77] B. J. Andrews and T. S. MooreA. Y. Niazi, "Millimeterwave microstrip antenna for dual polar and monopulse applications," presented at the *ICAP'83 3rd Int. Conf. Antennas Propag.*, Apr. 12–15, 1983.

[78] C. M. Jackson, "Low cost K-band microstrip patch monopulse antenna," *Microw. J.*, vol. 30, no. 7, pp. 125–126, 1987.

[79] M. Sierra-Castaner, M. Sierra-Perez, M. Vera-Isasa, and J. L. Fer-nandez-Jambrina, "Low-cost monopulse radial line slot antenna," *IEEE Trans. Antennas Propag.*, vol. 51, no. 2, pp. 256–262, Feb. 2003.

[80] H. Wang, D. G. Fang, and X. G. Chen, "A compact single layer monopulse microstrip antenna array," *IEEE Tran. Antennas Propag.*, vol. 54, no. 2, pp. 503–509, Feb. 2006.

[81] Y. Li, W. Hong, G. Hua, J. X. Chen, K. Wu, and T. J. Cui, "Simulation and experiment on SIW slot array antennas," *IEEE Microw. Wireless Compon. Lett.* , vol. 14, no. 9, pp. 446–448, Sep. 2004.

[82] B. Liu, W. Hong, Z. Q. Kuai, X. X. Yin, G. Q. Luo, J .X. Chen, H. J. Tang, and K. Wu, “Substrate integrated waveguide (SIW) monopulse slot antenna array,” *IEEE Trans. Antennas Propag.*, vol. 57, no. 1, pp. 275–279, Jan. 2009.

[83] Y. J. Chen, W. Hong, and K. Wu, “94 GHz substrate integrated monopulse antenna array,” *IEEE Trans. Antennas Propag.*, vol. 60, no. 1, pp. 121–129, Jan. 2012.

[84] T. Kim, J. Park, J.-Y. Seol, S. Jeong, J. Cho, and W. Roh, “Tens of Gbps support with mmWave beamforming systems for next generation communications,” in *Proc. IEEE Global Commun. Conf. (GLOBECOM’13)*, Atlanta, GA USA, Dec. 9–13, 2013, pp. 3790–3795.

[85] A. Bleicher, “The 5G phone future: Samsung’s millimeter-wave transceiver technology could enable ultrafast mobile broadband by 2020,” *IEEE Spectrum*, vol. 50, no. 7, pp. 15 – 16, Jul. 2013.

[86] T. S. Rappaport, S. Sun, R. Mayzus, H. Zhao, Y. Azar, K. Wang, G. N. Wong, J. K. Schulz, M. Samimi, F. Gutierrez, “Millimeter wave mobile communications for 5G cellular: It will work!” *IEEE Access*, vol. 1, no. 1, pp. 335–349, May 2013.

[87] W. Roh, J.-Y. Seol, J. Park, B. Lee, J. Lee, Y. Kim, J. Cho, and K. Cheun, “Millimeter-wave beamforming as an enabling technology for 5G cellular

communications: Theoretical feasibility and prototype results," *IEEE Commun. Mag.*, vol. 52, no. 2, pp. 106–113, Feb. 2014.

[88] H. Q. Ngo, E. G. Larsson, and T. Marzetta, "Energy and spectral efficiency of very large multiuser MIMO systems," *IEEE Trans. Commun.*, vol. 61, no. 4, pp. 1436–1449, Apr. 2013.

[89] S. Han, C.-L. I. Z. Xu, and C. Rowell, "Large-scale antenna systems with hybrid analog and digital beamforming for millimeter wave 5G," *IEEE Commun. Mag.*, vol. 52, no. 1, pp. 186–194, Jan. 2015.

[90] Y. X. Guo, K. M. Luk, and K. F. Lee, "Broadband dual polarization patch element for cellular-phone base stations," *IEEE Trans. Antennas Propag.*, vol. 50, no. 2, pp. 251–253, Feb. 2002.

[91] B. Lindmark and M. Nilsson, "On the available diversity gain from different dual-polarized antennas," *IEEE J. Sel. Areas Commun.*, vol. 19, no. 2, pp. 287–294, Feb. 2001.

[92] L. Wei, R. Q. Hu, Y. Qian, and G. Wu , "Key elements to enable millimeter wave communications for 5 G wireless systems," *IEEE Wireless Commun. Mag.*, vol. 21, no. 6, pp. 136–143, Dec. 2014.

[93] Q. Zhao and J. Li, "Rain attenuation in millimeter wave ranges," *in Proc. IEEE Int. Symp. Antennas, Propag. EM Theory*, Guilin, China, Oct. 2006, pp. 1–4.

[94] X. P. Chen and K. Wu, “Substrate integrated waveguide cross-coupled filter with negative coupling structure,” *IEEE Trans. Microw. Theory Tech.*, vol. 56, no. 1, pp. 142 –149, Jan. 2008.

[95] End Launch Connectors-Southwest Microwave [online]. Available: http://mpd.southwestmicrowave.com/showImage.php?image=832&name=End _Launch_Connectors.pdf

[96] R. J. Mailloux, Phased Array Antenna Handbook, Artech House, Boston, MA, 2005.

[97] R. L. Haupt , “Optimized weighting of uniform subarrys of unequal sizes,” *IEEE Trans. Antennas Propag.*, vol. 55, no. 4, pp. 1207-1210, Apr. 2007.

[98] S.-Z. Zhao, P. N. Suganthan, S. Pal, A. Basak and S. Das, “Multi-objective design of monopulse antenna with two-lbests multi-objective particle swarm optimizer,” *International Conference on Computational Problem-Solving (ICCP)*, 3-5 Dec. 2010, pp.209-214.

[99] M. W. McAllister and S. A. Long, “Rectangular dielectric resonator antenna,” *IEE Electron. Lett.*, vol. 19, no. 6, pp. 218–219, Mar., 1983.

[100] A. Rashidian, M. Tayfeh Aligodarz, L. Shafai, and D. M. Klymyshyn, “On the matching of microstrip-fed dielectric resonator antennas,” *IEEE Trans. Antennas Propag.*, vol. 61, no. 10, pp. 5291–5296, Oct. 2013.

[101] W. M. Abdel-Wahab, Y. Wang, and S. Safavi-Naeini, “SIW hybrid feeding network-Integrated 2-D DRA array: simulations and experiments,” *IEEE Antennas Wireless Propag. Lett.*, vol. 15, pp. 548–551, 2016.

[102] R. Chair, A. A. Kishk, and K. F. Lee, “Wideband simple cylindrical resonator antennas,” *IEEE Microw. Compon. Lett.* , vol. 14, no. 4, pp. 241–243, Apr. 2005.

[103] L. Guo and K. W. Leung, “Compact linearly and circularly polarized unidirectional dielectric resonator antennas,” *IEEE Trans. Antennas Propag.*, vol. 64, no. 6, pp. 2067–2074, Jun. 2016.

[104] W. W. Li and K. W. Leung, “Omnidirectional circularly polarized dielectric resonator antenna with top-loaded alford loop for pattern diversity design,” *IEEE Trans. Antennas Propag.*, vol. 61, no. 8, pp. 4246–4256, Aug. 2013.

[105] L. Hady, A. Kishk, and D. Kajfez, “Dual-band compact DRA with circular and monopole-like linear polarizations as a concept for GPS and WLAN applications,” *IEEE Trans. Antennas Propag.*, vol. 57,no. 9, pp. 2591–2598, Sep. 2009.

[106] P. F. Hu, Y. M. Pan, X. Y. Zhang, and S. Y. Zheng, “A compact filtering dielectric resonator antenna with wide bandwidth and high gain,” *IEEE Trans. Antennas Propag.*, vol. 64, no. 8, pp. 3645–3651, Aug. 2016.

[107] R. K. Mongia and A. Ittipiboon, “Theoretical and experimental investigations on rectangular dielectric resonator antennas,” *IEEE Trans. Antennas Propag.*, vol. 45, no. 9, pp. 1348–1356, Sep. 1997.

[108] R. J. Cameron, C. M. Kudsia, and R. R. Mansour, *Microwave Filters for Communication Systems: Fundamentals, Design, and Applications*. New York: Wiley, 2007, ch. 11.

[109] E. A. Navarro, A. Luximon, I. J. Craddock, D. L. Paul, and M. Dean, “Multilayer and conformal antennas using synthetic dielectric substrates, ” *IEEE Trans. Antennas Propag.*, vol. 51, no. 4, pp. 905 –908, Apr. 2003.

[110] S. Zhang, Y. Vardaxoglou, W. Whittow, and R. Mittra, “3D-printed flat lens for microwave applications, ” in *Proc. Loughborough Antennas Propag. Conf.*, Nov. 2-3, 2015, pp. 1–3.

[111] K. Gong and X. H. Hu, “Low-profile substrate integrated dielectric resonator antenna implemented with PCB process,” *IEEE Antennas and Wireless Propag. Lett.*, vol. 13, pp. 1023–1026, Jan. 2014.